CHAPTER THIRTY FOUR

NUCLEAR FUELS

Rudy J. M. Konings, Thierry Wiss, and Christine Guéneau

34.1 INTRODUCTION

The core of a nuclear reactor is composed of a controlled critical configuration of a fissile material, which in strict a sense is the fuel. This fissile material is contained in a matrix, normally a ceramic compound or eventually a metallic alloy, and in practice this combination of fissile material and matrix is called the nuclear fuel. In the fuel the fission process takes place, generating heat that must be transferred to the coolant, while producing fission products that must be retained. For example in uranium dioxide fuel for light water reactors (LWRs) the matrix for the fissile ^{235}U is made of $^{238}UO_2$ (95–97%). However, ^{238}U is fertile which means that by neutron capture it can be transformed into the fissile ^{239}Pu, which also contributes to the energy generation during the irradiation. Also the natural thorium isotope ^{232}Th is fertile, transforming to the fissile ^{233}U by neutron capture. Thus U, U/Pu as well as Th/U or even Th/U/Pu fuel cycles can be considered.

From the point of view of materials science, the choice of the chemical composition of the fuel and the matrix is based on the following considerations:

- Low neutron capture cross-section of the non-fissile and non-fertile elements, to avoid the increase of enrichment to compensate for the loss of neutrons, and the unnecessary production of radioactive waste
- High density of heavy atoms per unit of volume, to minimise the size of the reactor core

- No chemical reaction with its direct surroundings, i.e. the cladding and the coolant of the reactor
- Favorable physical properties, especially thermal conductivity and melting temperature that together define the margin to melting (the difference between the centerline temperature and the melting temperature)
- High mechanical stability (isotropic expansion, stable against radiation) in the temperature range of operation
- High thermal stability (no phase transformation, no dissociation)

Apart from its chemical composition (fuel type), the fuel is characterized by its form and its packing (Table 34.1). The fuel form indicates whether the fuel is a single phase material such as UO_2, a solid solution such as $(U,Pu)O_2$ or a composite of the fuel phase with a matrix phase that can be a ceramic or a metal. The fuel packing indicates the way the fuel material used is contained in the fuel element or in the reactor core. The most common packing is a stack of cylindrical fuel pellets encapsulated in a cladding tube, but in a high temperature reactor (HTR) the packing is a graphite compact containing spherical fuel particles, whereas in a molten salt reactor (MSR) the fissile material is dissolved in a liquid salt.

Many compounds of uranium have been studied as fuels for nuclear reactors: metal alloys and ceramics such oxides, carbides or nitrides. These have very different physical properties, particularly thermal conductivity and melting point. The former is a measure how well the generated heat can dissipate out of the fuel to the reactor coolant; the latter is a measure of the thermo-mechanical stability of the fuel. Clearly, the better the heat can be conducted (transferred) out of the fuel to the coolant, the lower the operating temperature of the fuel, or, from a different perspective, the higher the linear power at which the fuel can be operated. The difference between the operating temperature and the melting temperature, the so-called margin to melting, is therefore a very important parameter. Thus metal with a low melting temperature but a very high thermal conductivity as well as oxide with a very high melting temperature but a low thermal conductivity can be used as nuclear fuel.

Table 34.1 *The general characteristics of a nuclear fuel.*

Fuel type	*Fuel form*	*Fuel packing*
Oxide	Single phase	Pellet stack in pin
Carbide	Solid solution	Particle in compact
Nitride	Composite	Sphere-pac in pin
Metal		Liquid
Halide		

During its irradiation the fuel is subjected to extreme conditions of radiation and temperature, as well as to changes in the chemical composition due to the production of fission products as well as activation products (transuranium elements such as plutonium and the so-called minor actinides neptunium, americium and curium). As a result the structure and the chemical composition of the fuel change significantly, which has an impact on the fuel properties and thus on the fuel behavior. As safety is the key issue for reactor operation, it is important to understand the impact of these changes on the fuel performance both during normal operation and transient conditions. The ability of the fuel material to accommodate the irradiation effects determines the maximum burnup to which a fuel can be used.

In the current generation of thermal spectrum nuclear reactors, the pressurized water reactor (PWR) and boiling water reactor (BWR), uranium dioxide is used as fuel. This choice is dominated strongly by the requirement that the fuel should not react with the coolant, which the metal, nitride and carbide do very exothermally at typical operation temperatures. In fast spectrum reactors, which are normally cooled by liquid metals, a much wider choice of materials is possible and oxide, metal, carbide and nitride fuels have been proposed and investigated. In the high-temperature gas-cooled reactors with typical coated particle fuel normally oxide, carbide or oxy-carbide are employed as fuel. As shown in Fig. 34.1 all these fuels have their typical domain of operation depending on the allowable linear heat rate and burnup, which have been determined by extensive studies, as summarized in the present chapter.

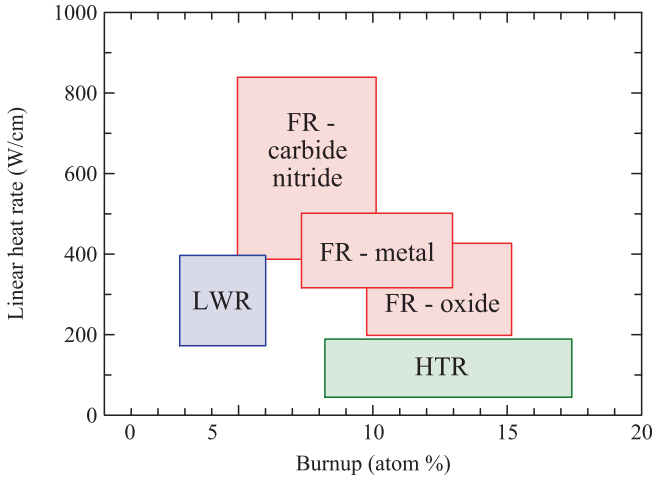

Fig. 34.1 *The typical linear heat rate and burn-up of nuclear fuel types for light water reactors (LWR), fast reactors (FR), and high temperature reactors (HTR); oxide fuel is the reference for LWR and HTR.*

34.2 HISTORICAL BACKGROUND

34.2.1 1942–1960

In spite of the fact that the fuel of the first nuclear reactor, Enrico Fermi's graphite moderated CP1 in Chicago, was principally uranium oxide, this material was not considered seriously as fuel for nuclear power plants till about 1955 (Dayton, 1960). Its low uranium density was considered to be a disadvantage and the focus was on the metal as fuel material during the first post-World War II years.

In line with this, the world's first commercial nuclear power station, Calder Hall in the UK, used uranium metal as fuel. The Calder Hall unit 1 reactor was constructed at the Windscale site in the UK between 1953 and 1956 and first went critical on 27 August 1956. It was a so-called Magnox type (thermal) reactor, in which the natural uranium metal was clad in a magnesium alloy, moderated by graphite and gas-cooled by carbon dioxide. However, the achievable burn-up of the fuel is low, as is the thermal efficiency of this reactor type. Also the limited stability of the magnesium alloy in water makes long term storage difficult and requires prompt reprocessing of the spent fuel.

In various countries also heavy water was studied as moderator because of its excellent moderation capacity. A team of Canadian, British and French scientists and engineers constructed the natural uranium metal fueled ZEEP reactor in Canada, which became critical in 1945. Historically this is closely related to the fact that during World War II a team of French researchers (among them Joliot-Curie and Kowarski) escaped from Paris via London to Canada with heavy water stocks (about 200 kg) collected in Vermork (Norway), the unique production plant at the time, to avoid its use by Nazi Germany. For obvious reasons also in Norway the development of a heavy water moderated reactor was initiated after World War II and the Kjeller reactor, a cooperation of Norway and the Netherlands, went into operation in 1951 using natural uranium as fuel.

The construction of the first commercial nuclear power plant in the USA, the Shippingport Atomic Power Station, was started in 1954 after the Atoms for Peace speech of President Eisenhower to the United Nations a year earlier. The team around General Rickover of the Atomic Energy Commission, in charge of this project, decided to build a thermal reactor, a PWR with uranium oxide fuel, clad in a zirconium alloy. Since normal water was used as coolant and moderator, instead of the better moderating but more expensive heavy water,[1] the reactor had to operate with enriched uranium, a technology used up to then for military purposes. But with this design the achievable fuel burnup and thermal efficiency were improved, and thus also the economics. The choice for

[1] The better moderation of heavy water is caused by the fact that it does not absorb neutrons as readily as water.

the PWR technology can also be understood when realizing that this reactor was in parallel serving as a prototype for naval propulsion, and as such was a continuation of the US naval atomic reactor programme that required compact reactor cores, which can be realized with an efficient heat removal using liquid water. The relatively good compatibility of the oxide with the coolant water made the fuel choice obvious.

Since uranium was still a relatively rare commodity at that time and the expectations for atomic energy were high in the 1950s, research into breeder reactors was also strongly pursued throughout the world. The first breeder reactor, Clementine in the USA, which began operation in 1949, used metal (δ plutonium) as fuel, and also EBR-I, which began operation in 1951, used metal fuel (uranium). Metal fuels offer the highest breeding ratio and the shortest doubling time[2] due to their high heavy metal density and their hard neutron spectrum in the absence of moderating elements. Therefore, the fast reactor developments initially followed the metal route. However, the dimensional instability of the fuel, caused by anisotropic radiation growth and fission product induced swelling, posed problems, and technical solutions needed to be found. The expectation was that alloying uranium with transition metals like Zr, Mo or Cr would mitigate the instability and programs to investigate this were started in USA and UK.

Apart from these solid fueled reactors, other concepts were also studied during this period. For example at Los Alamos National Laboratory (LANL) the use of liquid Pu–Fe fuel in the LAMPRE reactor was explored as a rigorous solution to the dimensional stability problem of the solid metal fuel. At Oak Ridge National Laboratory (ORNL) the concept of a molten salt fueled reactor (MSR) was investigated. Originally intended for aircraft propulsion, the MSR was further developed as thermal breeder to produce ^{233}U from ^{232}Th. Also suspensions of fissile material in aqueous solutions have been explored as fuel for reactors.

34.2.2 1961–1978

The success of the Shippingport reactor provided a strong incentive for industry to further develop the water-cooled uranium oxide fueled reactors for commercial power production. The PWR and the BWR were developed by US companies, and the technology was exported to Europe and Japan. A PWR was developed also in the USSR, under the name VVER. In Canada, however, the concept of natural uranium fuel and heavy water moderator/coolant was continued, resulting in the design of the CANDU reactor. In this reactor oxide fuel clad in Zircaloy was used also.

[2] The time required for a breeding reactor to double its fuel/fissile inventory.

In Europe the gas-cooled reactors were pursued initially, building on the Magnox technology. The advanced gas cooled reactor (AGR) became operational in 1962 in Sellafield (UK) and further units were built in the UK and France. Compared to the Magnox reactors, this reactor operated at a higher gas outlet temperature for improved efficiency, and used enriched uranium oxide fuel for less frequent refuelling.

Further improvement of the gas cooled reactor technology resulted in the high-temperature reactor (HTR), which uses helium as coolant and coated particles embedded in graphite as fuel elements to further improve the outlet temperature. The HTR was developed in Europe and USA at about the same time, based on the similar multilayer coated particles but with different fuel element types, graphite pebbles versus prismatic graphite blocks. Prototype reactors were built in USA (Peach Bottom), UK (Dragon) and Germany (AVR).

The trust in the nuclear technology resulted in a rapid increase in the installed nuclear power, rising to 100 GW toward the end of the 1970s, stimulated by the oil crisis in 1973. By that time, light water reactors were dominating the market. In most countries the LWR fuel cycle was originally based on reprocessing and recovery of the uranium and plutonium from the spent fuel. These elements were considered to be of economic value, especially for fast reactor operation. An industry thus emerged dealing with uranium enrichment, uranium oxide fuel fabrication, oxide fuel reprocessing and the fabrication of uranium and plutonium mixed oxide (MOX). The separated plutonium was intended for use in fast reactors, but also re-use in thermal reactors was investigated. As early as 1963 MOX fuel rods were loaded in the BR3 test reactor in Mol (Belgium) for research purposes, later followed by tests in commercial reactors in Germany (Obrigheim in 1972) and France (Chooz-A in 1974). Similar plans existed in the USA, but in 1977 President Carter decided to suspend the commercial reprocessing and recycling of plutonium in the USA.

The fast reactor developments were progressing less quickly during this period. By the beginning of the 1960s it appeared that the problems of achieving high burn-up with metal fuel due to dimensional instability could not be solved rapidly (Kittel *et al*., 1993). Mixed uranium and plutonium oxide that is very radiation tolerant, was not facing this problem and therefore attention slowly shifted to oxide fuel for fast breeder reactors also. Also carbide and nitride fuels were subject of extensive studies, in particular to achieve shorter doubling times (<15 years) of the fissile material in breeder reactors (Blank, 1988). In France the Commissariat à l'Energie Atomique (CEA) made the decision to explore mixed oxide fuel in their Rapsodie fast flux test facility (favored over U–Pu–Mo and (U,Pu)C) and the irradiation of the first core was highly successful. At about the same time the BOR-60 and BN-350 reactors in the USSR and the SEFOR reactor in the USA also started substantial testing of mixed oxide fuel. The disadvantage of the oxide fuel, low thermal conductivity and hence high operating temperature, proved to be an advantage as the resulting high

operating temperature resulted in release of the fission gases rather than extensive swelling. By the beginning of the 1970s most fast reactor demonstration plants around the world were based on mixed oxide fuel, including Phénix in France, PFR in the UK, KNK-II in Germany, FFTF in USA, and JOYO in Japan.

The development of metal fuel was continued at Argonne National Laboratory (ANL) during the 1960s and 1970s. It was found that the right combination of material selection and fuel pin design was needed to solve the problem of dimensional stability. Alloying with zirconium and leaving a sufficient large pellet-cladding gap were found to provide a solution. This concept could not be realized with helium gas filling the free volume of the fuel pin, but required that the pellet-cladding gap was filled with liquid sodium. This concept was successfully tested in the EBR-II breeder-reactor (Idaho).

34.2.3 1979–1986

On 28 March 1979 an accident occurred in the Three Mile Island (TMI) Unit 2 nuclear power plant in the USA. Owing to a failure of the secondary cooling circuit of this PWR, a partial core melt-down occurred. The damage to the reactor core was significant, but the release of radioactive material outside the containment was limited, and below what was expected. This initiated extensive research into the release of fission products in the fuel during normal operation as well as during severe accident conditions, when interaction with coolant and structural materials can occur.

A worse event took place on 26 April 1986, when a severe core melt-down occurred in one of the four nuclear reactor units at the Chernobyl site in the USSR. The Chernobyl reactor was a graphite moderated water-cooled RMBK type. Steam explosions and graphite fires, which occurred after the control over the reactor was lost during a safety experiment, caused part of the radiotoxic inventory of the core to be dispersed in the air, and a radioactive cloud penetrated far into Western Europe.

These two accidents initiated a debate about the risks and benefits of nuclear energy and strengthened the opposition against the use of nuclear power that was growing in several countries. At the same time the research into reactor safety was intensified. The interactions of fuel with steam and concrete were studied on a large scale throughout the world, leading to a significant increase in the knowledge of the behavior of fission products during severe accident conditions in PWRs.

34.2.4 1987–now

In the middle of the 1980s it became clear that the increase in installed nuclear power, reaching about 350 GW worldwide, was leveling off. The reasons for this

were the availability of cheap alternatives like oil and natural gas, for which large new reserves were found, and the decreasing public acceptance of nuclear power in the aftermath of the accidents at Three Mile Island and Chernobyl. The installed nuclear power was principally generated by thermal light water reactors of PWR and BWR type. The operating experience with fast reactors like Phénix and SuperPhénix in France had demonstrated that the economy of the fast breeder reactor (FBR) cycle could not (yet) compete with the LWR cycle, and the interest in FBR development decreased significantly. The SNR-300 fast breeder reactor in Germany, the construction of which was finalized, was never put into operation.

The plutonium that was separated at the reprocessing plants was not being reused in fast reactor fuel, but was accumulating steadily. For this reason the use of plutonium in mixed oxide fuel in LWRs became an attractive option. The MOX factory of BelgoNucleaire in Dessel (Belgium), which was fabricating MOX for fast reactors, began its industrial MOX production for LWRs in 1986, initially mainly for the French reactors, later also for Belgian, Swiss and German reactors. As a response to this expanding market, large capacity MOX fabrication plants were also constructed in France (MELOX, Marcoule) and Germany (Hanau), but the latter was never placed into operation for political reasons.

During this period uranium oxide fuel in PWRs saw a steady increase of the average discharge burnup, from about 33 to 55 MWd/kgHM today. The incentives for this burnup increase were of course economic, reducing the fuel costs as well as the waste disposal costs. This initiated extensive research to demonstrate that the fuel behavior remained consistent with license requirements. Because the allowable burnup for MOX fuel was lower than that of UO_2 fuel, similar studies evolved for MOX fuel in order to achieve parity between the UO_2 and MOX fuel elements (only partial MOX loading is allowed, generally up to one third of the total core).

In the 1990s the focus of the fuel research shifted towards studies addressing the back end of the fuel cycle. The accumulation of many tons of separated plutonium that could not be re-used in fast reactors led to increasing public concern. Apart from use in MOX fuel in LWRs, the destruction (fissioning) of separated plutonium in so-called uranium-free (or inert matrix) fuels for LWRs was proposed, changing the plutonium isotope vector in the discharged fuel significantly so that proliferation risks are diminished. At the same time an increasing interest developed in the possibility of reducing the long-term radiotoxic inventory of the waste intended for geological storage by so-called partitioning and transmutation (P&T) of the minor actinides (neptunium, americium and curium). The idea that by separating the long-lived radionuclides from the spent fuel and re-irradiating them with neutrons to destroy them (by fission), gained interest, especially in Japan and Europe. The research showed that P&T can be acomplished best in fast reactor systems, thus giving a new impulse to fast reactor fuel research.

Table 34.2 *Overview of the Generation IV systems.*

	Neutron spectrum	*Coolant*	*Coolant temperature* (°C)	*Fuel cycle*	*Fuel*
SFR	Fast	Na	550	Closed	Oxide, metal, carbide
LFR	Fast	Pb, Pb/Bi	480–800	Closed	Nitride, oxide
GFR	Fast	He	850	Closed	Carbide, nitride
MSR	Thermal/fast	fluoride salt	700–800	Closed	Fluoride
SCWR	Thermal/fast	H_2O	510–625	Open/closed	Oxide
VHTR	Thermal	He	900–1,000	Open	Oxide, oxycarbide[a]

[a] Coated particle fuel

This was further enhanced by the Generation IV initiative at the beginning of the twenty-first century. The Generation IV Forum was initiated to foster the international co-operation in research for the future generation(s) of nuclear energy systems, stimulated by the concern about the environmental impacts of fossil fuels and their potential long-term consequences on global climate change. As formulated in the Generation IV roadmap, future nuclear reactors must be able to produce energy "safely and economically, with certainty of long-term supply and without adverse environmental impacts" when continuing playing a role in the energy supply. Six nuclear systems have been selected for Generation IV, of which four are breeder reactors with a closed fuel cycle (Table 34.2): the sodium-cooled fast reactor (SFR), the lead-cooled fast reactor (LFR), the gas-cooled fast reactor (GFR) and the molten salt reactor (MSR). These concepts are not completely new but re-visits of past developments and as a consequence the research on the fuels for these systems will be building strongly upon the experiences from the past. For the solid fuel reactors mixed oxide is the state-of-the-art technology whereas dense metal, carbide and nitride offer the potential of obtaining high breeding ratios. The MSR is particularly suited for the Th/U cycle. The other two systems are thermal reactors with an open fuel cycle: the very high temperature reactor (VHTR), a further development of the HTR, and the supercritical water reactor (SCWR), building on the LWR technology. For most of these six reactor designs, the development and optimization of the fuel as well as the structural materials in the reactor core is a key issue for their success.

34.3 THE NUCLEAR FUEL CYCLE

As discussed in the previous section, the nuclear fuel is the central product of a chain of industrial processes, generally called the nuclear fuel cycle. The basic nuclear fuel cycle in which the fuel is used in a single load only and is finally

stored in a geological repository (the so-called open cycle) consists of the following steps:

- *Mining*: Uranium is a relatively abundant element in the earth's crust (2.8 ppm). It occurs in high concentrations in hard rocks (e.g. granites) and sandstones. High grade ores contain more than 2 wt% uranium, which is present in a wide variety of minerals, with uraninite (UO_2) as one of the most important ones. Natural uranium is composed of about 99.3% of the ^{238}U isotope and 0.7% of ^{235}U.
- *Refining and conversion*: The ore is crushed and milled and then treated with acid to extract the uranium. The next step is a purification to selectively separate the uranium. After drying an uranium oxide concentrate, U_3O_8, which is called yellowcake, is obtained.
- *Enrichment*: Since most commercial reactors require a ^{235}U concentration in the fuel (3–5%) that is higher than in natural uranium, the fraction of this isotope must be increased by enrichment. The enrichment is based on the small mass difference between the two isotopes and can be achieved by two different methods: gaseous diffusion and gaseous centrifugation. For this purpose the yellowcake is converted to UF_6, a highly volatile compound (boiling point 329.7 K).
- *Fabrication*: Starting from enriched UO_2 powder, the fuel for the reactor is fabricated in a series of process steps, strongly depending upon the fuel type, form and packing.
- *Irradiation*: In the reactor the fission takes place and energy is produced, which is generally used to generate electricity. During the irradiation, physical processes take place in the fuel that strongly affect its properties, and this degradation is one of the factors determining the maximum burnup[3] the fuel can reach.
- *Storage and cooling*: After the irradiation the fuel elements are removed from the reactor, and they are stored for several years, during which radioactive decay reduces the radioactive inventory and the decay heat produced in the spent fuel.
- *Encapsulation*: The spent fuel elements are prepared for the final storage in a geological repository. For this purpose the fuel elements are encapsulated in corrosion resistant canisters that are designed for the specific (hydro) geological conditions of the repository. Since in most countries final geological repositories are not yet existing or in operation, further storage is required (interim storage).
- *Final storage*: The spent fuel canisters are stored in a (deep) geological repository to isolate them from the biosphere during very long time

[3] The burnup is usually expressed in units of energy generated per kilogram of heavy metals (uranium, plutonium), i.e. MWd/kgHM. Another unit that is often used is Fission per Initial Metal Atom, FIMA.

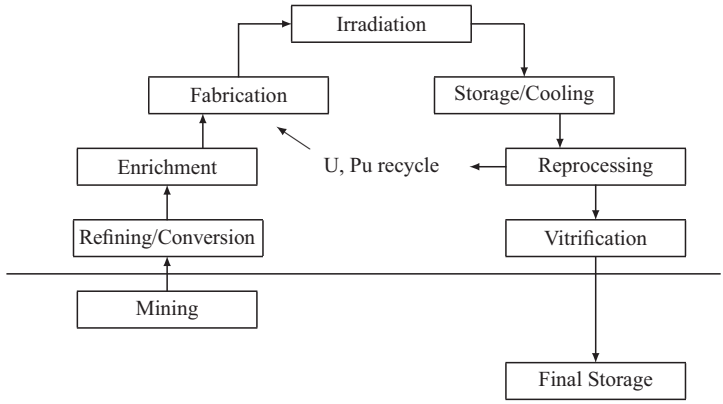

Fig. 34.2 *Schematic representation of the closed nuclear fuel cycle.*

periods, often with the option of retrievability. Stable geological host rocks such as clay, salt or granite are studied for these repositories.

Since the spent fuel still contains a few percent of fissile isotopes (^{235}U and ^{239}Pu), the fuel can be reprocessed to recover them for re-use. This is often called the closed fuel cycle (Fig. 34.2) and involves the following additional steps:

- *Reprocessing*: The uranium and the plutonium are separated from the spent fuel by chemical processing.
- *Vitrification*: The waste products from the reprocessing (fission products, minor actinides) are immobilized, generally in a glass matrix.
- *Recycling*: The separated plutonium (and a fraction of the separated uranium) is recycled in fuel for nuclear reactors.

The nature of the fuel cycle processes of especially the closed cycle depends strongly on the type of reactor and its fuel. The reprocessing technology for the extraction and separation of plutonium and uranium from UO_2 and MOX fuel of current generation reactors, the so-called PUREX (plutonium–uranium extraction) process, is based on liquid–liquid solvent extraction, after dissolution of the spent fuel in nitric acid. It is used on an industrial scale in Europe, Russia and Japan (see Chapter 24). The high level waste from this process, which contains the fission products and the minor actinides, is generally immobilized in the form of a (borosilicate) glass.

For the next-generation reactors a wide variety of fuel forms is considered, which, moreover, potentially have to include full recycling of actinides, to minimize the production of long-lived radioactive waste. As shown in Table 34.2 it is clear that apart from oxides, also other fuel forms like metals, carbides and nitrides are considered, which might require different fuel cycle processes. The cycle for metal fuel has been developed in the frame of the fast reactor program

in the USA, particularly for EBR-II, and is based on electrochemical reprocessing in molten chloride salts. Carbide and nitride fuels can be reprocessed by aqueous solvent extraction processes, and are thus compatible with PUREX technology, but these fuel materials can also be processed using pyrochemical methods. Criteria such as fuel cooling time, material purity, safeguarding of the process, etc. will play an important role in the final choice between these methods.

34.4 RADIATION DAMAGE IN NUCLEAR FUELS

34.4.1 The slowing down of energetic projectiles in matter

Nuclear fuels have to operate safely for several years while being exposed to extreme conditions of radiation, causing damage and chemical changes to the fuel matrix. When the conditions are met for a fission to occur, about 200 MeV energy is dissipated in the fuel lattice. Most of this energy is carried by the fission fragments, i.e. high energy heavy ions, and the heat production in the fuel pellets ensues mostly from the slowing down of these fission fragments, but also from their further radioactive decay, most frequently by gamma or beta decay. The heat dissipated in the lattice of the crystalline nuclear fuel is a primary effect from the energy losses of the fission fragments by nuclear or electronic interactions on the atoms constituting the fuel crystal lattice. As a direct consequence lattice defects are created along the path of the fission fragments leading to modification of the physical properties of the fuel when accumulated over time.

The intense neutron fluxes, with energies ranging from electron volts to megaelectron volts, produced by the fission reactions themselves and necessary to sustain the controlled nuclear chain reaction, form another source of damage, as is the intense β-radiation field that is present because most fission products are radioactive with different decay energies and very different half-lives. In addition to the fission processes, damage is also created by alpha-decay from the actinides originally present in the fuel, and even more so, from the "minor actinides" (Np, Am, and Cm) that are formed by successive neutron capture during the operation of the fuel. The alpha-decay has to be accounted not only during reactor irradiation (at elevated temperature), but also during storage before and after reactor irradiation, i.e. under conditions where thermally activated damage recovery is largely or fully absent.

In general, particles or ions passing through matter lose energy via two processes, either by direct collisions with the atoms of the matter (elastic collisions) or by dissipating their energy on the electrons (inelastic collisions), hence nuclear energy loss $(\mathrm{d}E/\mathrm{d}x)_n$ leading directly to displaced atoms, or electronic energy loss (ionizations) $(\mathrm{d}E/\mathrm{d}x)_e$. Any given radiation source can exhibit these two types of energy loss, depending on the type of projectile and its

characteristics like energy and mass. Under the conditions in nuclear fuels both processes can occur simultaneously in different proportions (Was and Allen, 2008).

In this section, the basic processes for energy loss will be described and the stopping power and range of various ions/particles will be defined. The radiation damage produced by the passage of these ions/particles will be conceptually described. The fission damage and alpha damage will be treated more specifically.

(a) Energy loss and displacements produced by neutrons

The neutrons in a nuclear reactor are generally grouped according to their (kinetic) energy: thermal neutrons with energy $E < 1$ eV (0.025 eV), epithermal neutrons with 1 eV $< E <$ 10 keV and fast neutrons with $E >$ 10 keV. In the energy domain where neutrons from fission are emitted, only elastic collisions and capture are considered.

In thermal reactors the energy loss by the neutrons in the moderator is the sine qua non condition for a controlled fission reaction chain to occur while the remaining fast neutrons (not thermalized) produce damage in the fuel and in the structure materials. A neutron of mass $m = 1$ and of energy E_n, while passing through a medium of mass M_1, will occasionally collide (mean free path $\sim$1 cm) with a lattice atom, imparting to it an energy (depending on the impact parameters) up to a maximum energy given by

$$E^{max} = \frac{4mM_1}{(m + M_1)^2} E_n \tag{34.1}$$

or for $M_1 \gg m$

$$E^{max} \approx \frac{4E_n}{M_1} \tag{34.2}$$

The maximum pka (primary knock-on atom) energies for a neutron of energy $E_n = 1$ MeV in UO_2 are thus 17 keV for U, and 250 keV for O, but most interactions with neutrons will lead to a smaller energy transfer.

The minimum neutron energy to produce one displacement is given by $E^{max} = E_d$, where E_d is the displacement energy, for example 20 eV for O and 40 eV for U in UO_2. Hence

$$E_n^{min} \approx 0.1\text{keV} \tag{34.3}$$

Thus thermal (low energy) neutrons do not produce direct displacements. On the contrary, the fast neutron damage will result from elastic collisions on the target atoms producing displacements. The neutrons will transfer part of their energy to primary knock-on atoms (pka's) that could themselves generate a succession of collisions (cascades) of lattice atoms (as a function of their displacement energy, E_d). A convenient estimation of the number of primary

defects can be obtained using the Kinchin and Pease formula (Kinchin and Pease, 1955):

$$N = 0.8\frac{E_n}{2E_d} \tag{34.4}$$

where N is the number of Frenkel defects (an interstitial and vacancy pair) and E_n the (elastic) energy. The damage level is often expressed as displacements per atoms (dpa). It is conveniently used to describe a damage dose for fast neutrons whose energy loss is primarily elastic. It is also used for other projectiles including heavy ions but in that case it is more appropriate for the low energy ions, hence those with high nuclear energy losses.

One of the most severe effects of displacements produced by neutrons is known as the "Wigner effect": defects produced by neutrons can release a large amount of energy when heating the damaged material. This occurred during the Windscale accident in the UK (1957) during annealing of the graphite moderator of the Pile 1 reactor.

(b) Energy loss and displacements produced by β-decay

The energy distribution for the beta decays of the fission products in nuclear fuels is a continuum with E_β^{max} (typically 2.6 keV < E < 10.4 MeV). The e^- and e^+ particles produce ionization and excitation along their path, and the nuclear scattering is very large. The Rutherford (elastic) scattering cross-section is proportional to the mass ratio of the displaced atom and the electron, $(M_1/m_0)^2$, and the cross-section ratio $\sigma_{e^-}/\sigma_{p^+}$, which is 4×10^6. In fact σ can be extremely large and electrons have to be considered as targets. Electrons can also produce isolated displaced atoms if their energy is high enough. The minimum energy, E_e^{min}, to displace a lattice atom is given by

$$E_d = 2\frac{m_0}{M}\frac{E_e^{min}}{m_0c^2}\left(E_n^{min} + 2m_0c^2\right) \tag{34.5}$$

where m_0 is the electron mass, M the mass of the displaced atom and c the velocity of light. β-decay thus causes very few isolated point defects.

The emission of photons as well as X-rays in nuclear fuel will be neglected in this discussion. They contribute to the heating and ionization but their consequences are negligible compared to the other damage sources during operation of the fuel.

(c) Energy loss and displacements from α-decay

A heavy recoil atom, e.g. ^{237}Np produced in the decay of ^{241}Am, receives a recoil energy E due to conservation of momentum, $ME = m_\alpha E_\alpha$, hence typically ~100 keV (91 keV in the decay of ^{241}Am). These recoil atoms show predominantly nuclear stopping and produce a dense collision cascade with typically about 1,500 displacements within a short distance of 20 nm. A simulation of

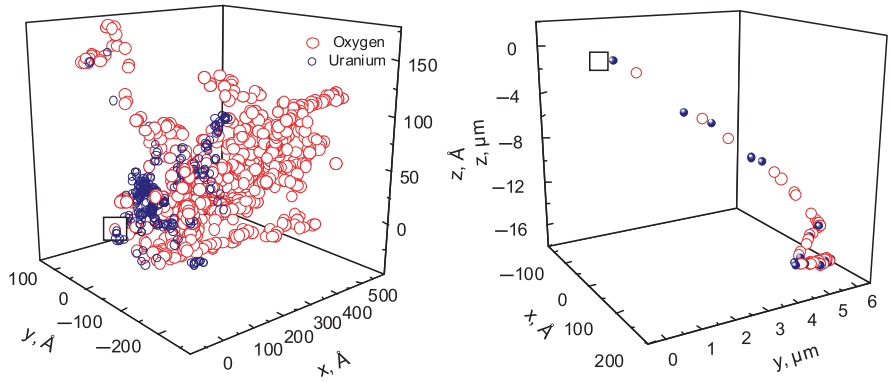

Fig. 34.3 *Displacement cascades in uranium dioxide produced by the recoil atom of* ^{238}Pu, *i.e.* ^{234}U *with* 94 *keV energy* (*graph left*) *and the alpha-particle of* 6 *MeV* (*right graph*). *The primary knock-on atom is indicated by a square. Only the displaced atoms are shown as circles* (*blue for uranium and red for oxygen*).

Table 34.3 *Displacements induced in* UO_2 *by different damaging sources calculated using the TRIM code* (*Ziegler et al.*, 1985).

	Energy/ keV	*Range/μm*			*Fraction of energy lost by elastic/inelastic collisions*	*Number of defects formed, N*
		UO_2	*UC*	*UN*		
Light fission product	~95,000	9	8.4	6.6	0.03/0.97	40,000
Heavy fission product	~70,000	7	6.8	3.6	0.06/0.94	60,000
α-particle	5,500	15	14	11.3	0.01/0.99	200
Recoil atom	95	0.020	0.018	0.014	0.90/0.10	1,500

such a displacement cascade produced by the ^{234}U recoil atom of the decay of ^{238}Pu as well as from the alpha-particle, is shown in Fig. 34.3. Table 34.3 gives some characteristics for the case of α-decay in UO_2.

(d) Impact of fission fragments

Fission produces two fission fragments, also called fission products[4] (FPs), plus two to three neutrons:

$$^{235}U + n = X_1 + X_2 + 2 \text{ to } 3\ n \tag{34.6}$$

[4] In a strict sense a fission fragment possesses kinetic energy, whereas a fission product is at rest.

The fission products fall into two groups (Fig. 34.4), the light ones (LFP, for example Mo or Kr with ~95 MeV energy) and the heavy ones (HFP, for example I or Ba with ~70 MeV energy). Typical displacement characteristics for the case of UO_2 and some other fuel materials are given in Table 34.3 and in Fig. 34.5: range, number of defects produced, etc. The exact values depend on the characteristics of the substance used (e.g. displacement energy, E_d, atomic number, density etc.).

Because of the high energy deposition rate, typically 20–30 keV/nm, a locally (over-)heated track (fission spike or thermal spike) may be formed. Such fission tracks have been observed in many materials. Most of the energy deposition is by electronic energy loss, in particular for the more energetic light fission products. This can cause the formation of additional defects and/or rearrangement of existing defects, in addition to causing local heating to or above the melting point.

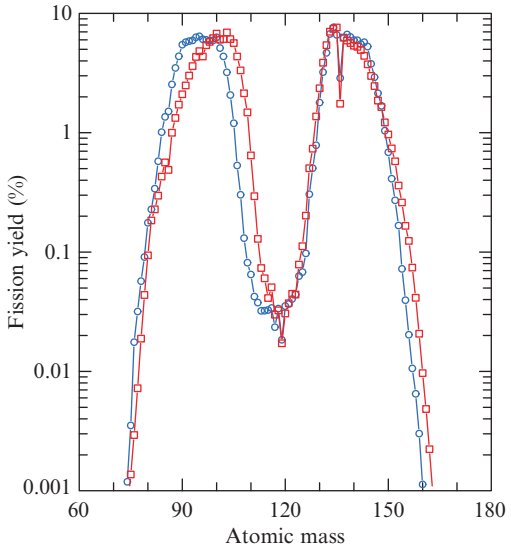

Fig. 34.4 *The fission yields of* ^{235}U (○) *in a thermal neutron spectrum and* ^{239}Pu (□) *in a fast neutron spectrum.*

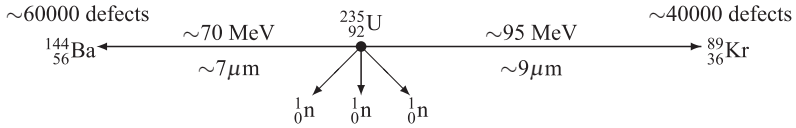

Fig. 34.5 *Schematic representation of the fission process.*

A short description of the sequence of events in the fission spike is the following:

- Primary phase or ballistic phase: The passage of the fission fragment (a few picoseconds) is very short but it defines the initial size and shape of the spike. Most Frenkel defects are produced by secondary collision cascades. The deposited Coulomb energy is dissipated into local heating through electronic interactions with recoiling ions to produce a thermal spike.
- Second or quenching phase: Recombination of vacancies and interstitials occurs when the spike comes to thermal equilibrium. An interstitial-rich outer zone and a vacancy-rich inner zone form. The hydrostatic pressure field originally created by the molten core of the spike – contributing to the separation of interstitials from the vacancies of the Frenkel pairs formed in the primary phase – is replaced by compressive stresses in the outer zone and tensile stresses in the core.
- Third or track annealing phase: More recombination occurs, some vacancy clusters are stabilized by fission gases forming embryos for gas bubbles.

The processes in these three phases are repeated many times throughout the volume of a homogeneous fuel. The complete fuel is affected after a rather short irradiation time, the level of one displacement per atom (dpa) being typically reached within less than 1 day. The consequences are significant fission-enhanced diffusion, fission-enhanced creep, re-solution of fission gas from bubbles, etc. (Blank, 1972; Brucklacher and Dienst, 1972; Blank and Matzke, 1973; Ronchi, 1973; Matzke, 1983), as will be discussed below.

Figure 34.6 shows the large difference in electronic energy loss, $(dE/dx)_e$, between the alpha-particles and the fission products. The energy loss curves show the electronic stopping only, i.e. the ionization part, with high values of 18–22 keV/nm at the point of fission (full ion energy) for the case shown,

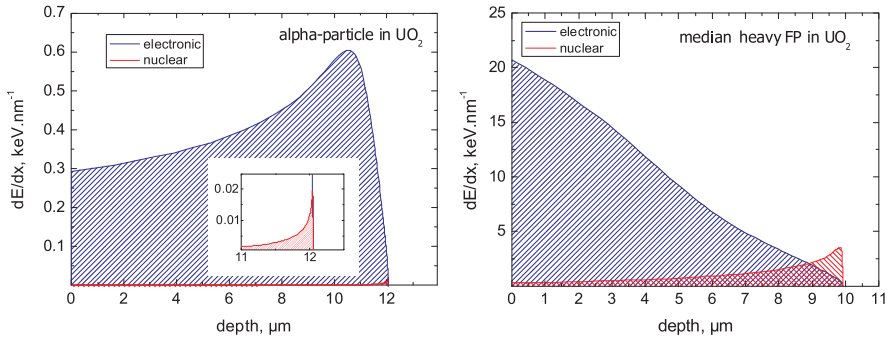

Fig. 34.6 *Electronic energy loss* (*dashed lines*) *and nuclear energy losses* (*red area*) *of a typical* α*-particle* (*left*) *and of a median fission product* (*right*) *in* UO_2.

i.e. UO_2. The nuclear, i.e. the displacement damage part, peaks at the end of the range (~1 keV/nm) and is very small (but still present) at the point of fission (~0.1 keV/nm). The ratio of nuclear to electronic stopping is always low for those high energies, but it varies between 1:180 at the fission site and approximately 1:3 toward the end of the range, or even below 1:1 at the very end.

The recoil atoms of the α-decay and the high defect density produced by their slowing down are not included in Fig. 34.6 because of the large difference in range: about 1,500 displacements are formed along a very short track of only 20 nm, as shown in Fig. 34.3.

34.4.2 Radiation damage

The effects caused by atomic displacements are rather complex and depend on the relative sink strengths of a given material for interstitials and vacancies and on the temperature. A majority of the Frenkel pairs recombine in a short time. The defects that survive migrate through the crystal lattice where they cluster to form extended defects like dislocation loops and dislocation networks or are absorbed in grain boundaries, gas bubbles or precipitates, which act as sinks.

An important effect of radiation damage is the volume increase of the crystal lattice, leading to macroscopic swelling of the fuel material. For example, at room temperature alpha damage in UO_2 doped with ^{238}Pu leads to a distinct increase of the volume, saturating rapidly, when an equilibrium between formation and annealing of defects is attained (Fig. 34.7). In this case the ingrowth or

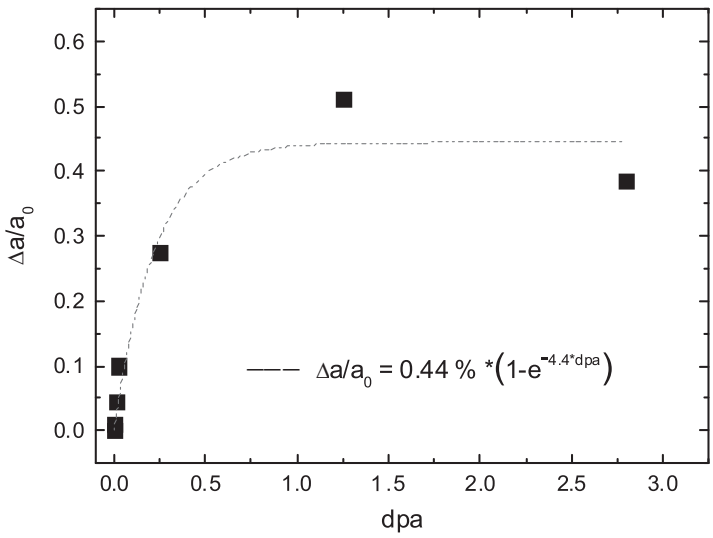

Fig. 34.7 *The change in the lattice parameter of UO_2 doped with ^{238}Pu.*

evolution of radiation damage, expressed as the relative volume change $\Delta V/V_0$, with time is described by a simple exponential equation:

$$\frac{\Delta V}{V_0} = A\left(1 - e^{-B\lambda t}\right) \tag{34.7}$$

where λ is the decay constant, t the time, A the value at saturation and B the rate constant for simultaneous annealing of defects.

Accumulation of radiation damage can also lead to damage-induced phase transformation, most notably amorphization (or metamictization) of originally crystalline matter. Another consequence is polygonization, also called grain subdivision, a process that transforms a typical grain of an originally well-crystallized ceramic into thousands of small grains in the submicron range. Polygonization occurs in some nuclear fuels, including UO_2.

When discussing damage accumulated by fission, or to a lesser extent, by radioactive decay, one has to consider the simultaneous change in chemistry. Each fission, besides producing the above mentioned 100,000 displacements, also produces two fission products, often accumulating to more than 10 at.% at the end of life of the nuclear fuels. The fission products include gaseous elements like Kr, Xe, and volatile elements such as Br, I, Cs, etc. Since most of the fission products decay by β-particle emission, new elements are formed. For example, Cs, a highly abundant fission product, decays to Ba with another valence state and a different chemical behavior. Also gaseous helium is formed by the α-decay of short-lived actinides that are formed, e.g. ^{241}Am that decays to ^{237}Np. The α-decay results in displacements in the lattice and the He atoms may precipitate into bubbles, thus causing the fuel to swell. Thus we deal with complex phenomena that explain why it is very important to understand damage effects and mechanisms, not only in new but also in conventional nuclear fuels, despite the large amount of work devoted to this subject in the past five decades.

UO_2 does not become amorphous under any damage source. Fission damage and the ingrowth of fission products can eventually cause polygonization, i.e. both single crystals and sintered specimens are transformed into a material consisting of very small grains of about 0.1–0.3 μm grain size. In UO_2 fuel about 10^4 subgrains are formed from each original UO_2 grain. Polygonization is the term used to describe the rearrangement of those dislocations formed in the earlier stage of irradiation that do not annihilate one another, into walls of dislocations, forming low-energy "subboundaries" and perfect but slightly misaligned subgrains. This phenomenon was already observed in early test irradiations and was called grain subdivision. It was received renewed attention in the 1980s when power reactors increased the fuel burn-up (see section 34.5.4.e).

Another interesting fission-related process is radiation-enhanced or, more specifically, fission-enhanced diffusion. Especially for the diffusion of U and Pu in UO_2, $(U,Pu)O_2$, UC, (U,Pu)C, UN, and (U,Pu)N a large number of in-pile experiments were performed (for the carbides and nitrides see Section 34.6). Between 130°C and $\sim$ 1,000°C, the diffusion of U and Pu is completely

athermal, i.e. independent of temperature. The results have been explained by the formation of thermal spikes along the trajectory of the fission fragments in combination with a pressure gradient. Because of the high-energy deposition rate (see Fig. 34.6), a locally (over)heated track (fission spike or thermal spike) may be formed. Such fission tracks are seen in transmission electron microscopy in thin UO_2 foils and with the replica technique at UO_2 surfaces but not in TEM samples prepared from the bulk (Ronchi, 1973; Wiss *et al.*, 1997). This indicates that the threshold for the formation of observable tracks must be near to the energy loss value of fission products, i.e. 18–22 keV/nm.

An extreme case of fission spikes interacting with the fuel matrix is the destruction of preexisting fission gas bubbles by a fission spike that is passing by. The phenomenon is called ''re-solution'' of fission gas and was known for about 40 years. It was explained by the above-mentioned hydrostatic pressure component (Blank and Matzke, 1973) of the thermoelastic stress field of the fission spike interacting with the bubbles. This phenomenon is illustrated in Fig. 34.8 showing a TEM micrograph of densification in a LWR UO_2 fuel irradiated at 35,000 MWd/tHM (Ronchi and Wiss, 2002).

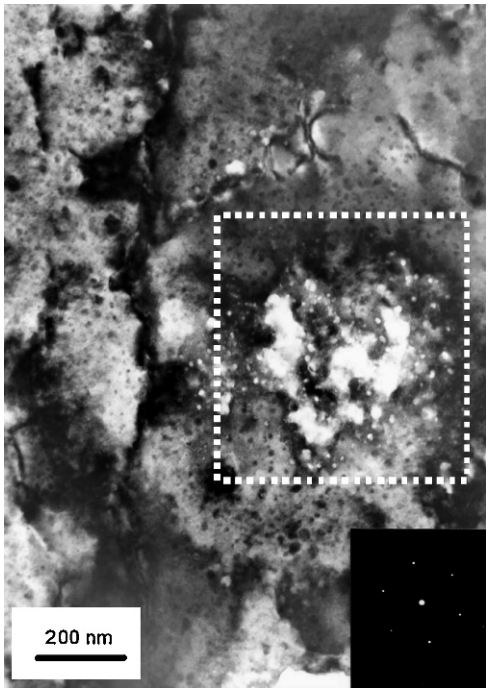

Fig. 34.8 *TEM micrograph of a LWR UO_2 fuel irradiated at* 35 *MWd/kgHM. The dotted white square indicates the location of an initial sintering pore where radiation enhanced re-densification* (*in-pile sintering*) *occurred through the passage of fission fragments.* (©*European Communities*, *reproduced with permission.*)

The pressure gradients also serve to explain the surprisingly high U and Pu diffusion coefficients. To decrease these gradients, the highly mobile uranium interstitials are pushed away from the spike axis, thus increasing the U-diffusion to values higher than those calculated for atomic mixing and thermal spike effects alone. Like diffusion, in-pile creep of UO_2 was shown to be athermal and fission-enhanced below ~1,273 K as well (Brucklacher and Dienst, 1972). Most of the aspects of damage evolution and its consequences on properties changes are discussed further in Sections 34.5.4 (d) and 34.5.4 (e).

34.5 THERMAL AND FAST REACTOR OXIDE FUEL

34.5.1 The actinide oxides

(a) Uranium dioxide

Uranium dioxide has a face-centered cubic (fcc) crystal structure, isostructural with fluorite, CaF_2 (Fig. 34.9). The unit cell contains four molecules of UO_2. It is face-centered with respect to the uranium ions, which occupy the octahedral positions (0,0,0), $(\frac{1}{2},\frac{1}{2},0)$, $(\frac{1}{2},0,\frac{1}{2})$ and $(0,\frac{1}{2},\frac{1}{2})$, whereas the oxygen ions occupy the $(\frac{1}{4},\frac{1}{4},\frac{1}{4})$ and its equivalent positions (tetrahedrally coordinated by uranium). Interstitial ions may be accommodated at octahedral vacant sites, which is evident from the oxygen sublattice, showing eight cubes of oxygen per unit cell, of which only half are occupied by a U^{4+} ion.

Uranium dioxide is not the only compound in the U–O system (Fig. 34.10). Several oxides with different O/U ratios exist: U_4O_9 ($UO_{2.25}$), U_3O_7 ($UO_{2.33}$, probably a metastable phase formed during UO_2 oxidation), U_3O_8 ($UO_{2.67}$) and UO_3. At low temperatures UO_2 is a line compound. At higher temperatures it forms a solid solution with a maximum oxygen content corresponding to $UO_{2.25}$, which means that the interstitial holes in the lattice are filled with

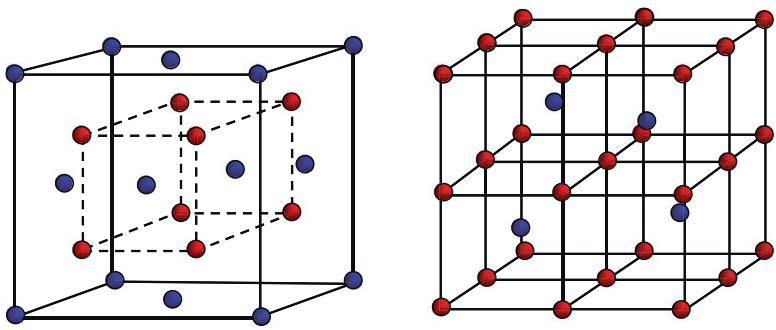

Fig. 34.9 *The crystal structure UO_2. The unit cell (left) and the oxygen lattice (right) with the uranium atoms in blue and the oxygen atoms in red.*

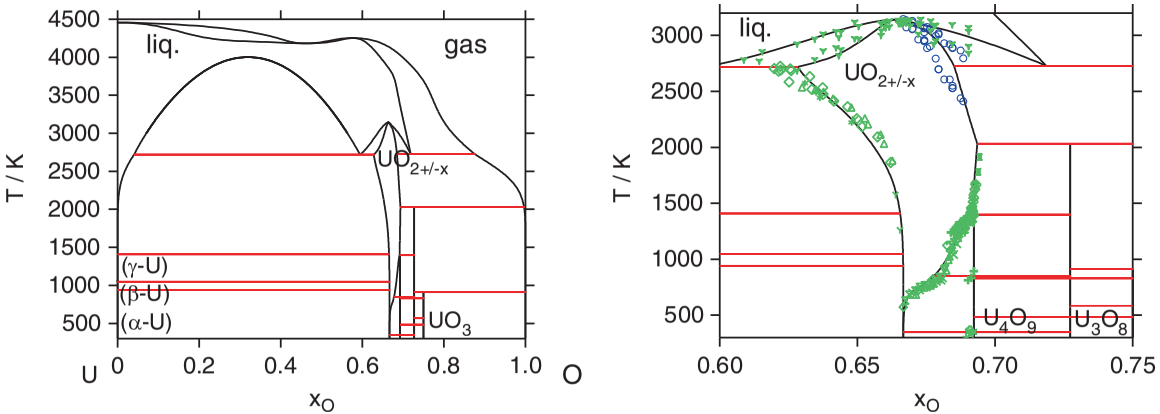

Fig. 34.10 *The assessed U-O phase diagram (left) and a blow-up of the region around UO_2 (right) (After Guéneau et al. 2002). The blue circles show the recent results of Manara et al. (2005) that were not considered in the assessment; the other symbols show the experimental data from various different sources that were included in the assessment.*

oxygen atoms, compensated by oxidation of the uranium ions from 4+, to formally 5+. Neutron diffraction studies by Willis (1963, 1987) have shown that for $x > 0.03$ in UO_{2+x}, all oxygen interstitials are displaced from their normal site along the <110> and <111> directions to form the so-called Willis type clusters by associating with the nearby oxygen vacancies (Fig. 34.11). Yakub *et al*. (2009) showed by molecular dynamics calculations that also interstitial tetra- and pentamer cuboctahedral clusters form very stable configurations in UO_2. Above about 2,000 K also substantial hypostoichiometry can occur, which means that oxygen vacancies are formed in the lattice, compensated by reduction of some of the uranium ions from 4+, to formally 3+. Stoichiometric UO_2 melts at (3,120 ± 30) K (Fink, 2000). In the metal-oxide part of the diagram, a miscibility gap exists in the liquid state above ~2,720 K. The assessed U–O phase diagram is shown in Fig. 34.10, but it is worth mentioning that recent studies using laser-melting (Manara *et al*., 2005) have shown that the liquidus and solidus for the hyper stoichiometric range, shown in the assessed phase diagram, must be re-assessed.

Due to the cubic structure UO_2 lattice expands with temperature along all three principal axes in the same way and thus shows isotropic behavior as far as its mechanical properties are concerned. The thermal expansion data for UO_2 were reviewed by Fink (2000) and the recommended values are given in Table 34.4.

The thermal conductivity is a key property of a fuel because it determines how well the heat generated by the fission can be extracted from the fuel, and thus it determines the local temperature in the fuel. The thermal conductivity of oxides

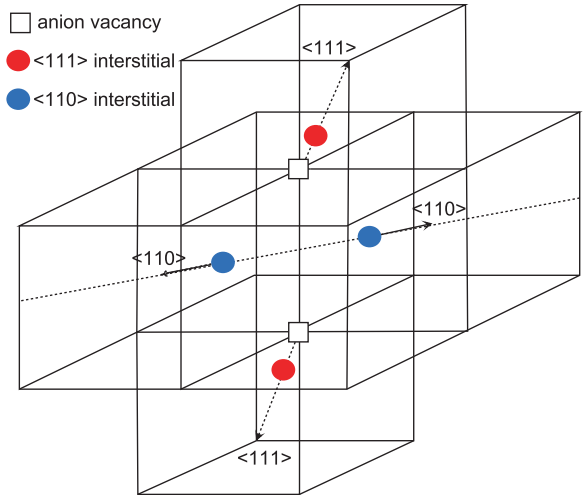

Fig. 34.11 *The 2:2:2 cluster proposed by Willis* (1978). *The corners of the cubes correspond to the positions of oxygen. The cluster contains two anion vacancies, two interstitial oxygens displaced along* < 111 > *and two interstitial oxygens displaced along* < 110 >.

Table 34.4 *The thermal properties of UO_2.*

	Equation	*T/K*	*Ref.*
(a) Solid UO_2			
Heat capacity	$C_p/(\mathrm{J{\cdot}K^{-1}{\cdot}mol^{-1}}) = 52.1743 + 87.951 \times 10^{-3}\,(T/K) - 84.2111 \times 10^{-6}(T/K)^2 + 31.542 \times 10^{-9}\,(T/K)^3 - 2.6334 \times 10^{-12}(T/K)^4 - 1.3288 \times 10^{6}(T/K)^{-2}$	298.15–3,120	Fink (2000)
Thermal expansion	$L(T) = L_{273}\,(0.9973 + 9.082 \times 10^{-6}\,(T/K) - 2.705 \times 10^{-10}(T/K)^2 + 4.391 \times 10^{-13}\,(T/K)^3)$	273–923	Fink (2000)
	$L(T) = L_{273}(0.99672 + 1.179 \times 10^{-5}(T/K) - 2.429 \times 10^{-9}\,(T/K)^2 + 1.219 \times 10^{-12}\,(T/K)^3)$	973–3,110	Fink (2000)
Thermal conductivity[a]	$\lambda/(\mathrm{W \cdot m^{-1} \cdot K^{-1}}) = \dfrac{1}{0.075408 + 1.7692 \times 10^{-4}(T/K) + 3.6142 \times 10^{-8}(T/K)^2} + \dfrac{2.024 \times 10^{11}}{(T/K)^{5/2}} \exp\left(\dfrac{-16350}{(T/K)}\right)$	298.15–3,120	IAEA (2006)
Vapor pressure[b]	$^{10}\log(p/\mathrm{MPa}) = 66.53672 + 4.382 \times 10^{-3}(T/K) - 4.411 \times 10^{-7}(T/K)^2 - \dfrac{37,090}{(T/K)} - 19.070\,^{10}\log(T/K)$	1,800–2,600	IAEA (2006)
(b) Liquid UO_2			
Enthalpy of fusion	$\Delta_{fus}\,\mathrm{H^\circ} = 70 \pm 4$ kJ/mol		Fink (2000)
Heat capacity	$C_p/(\mathrm{J{\cdot}K^{-1}{\cdot}mol^{-1}}) = 0.25136 + 1.3288 \times 10^{9}\,(T/K)^{-2}$	3,120–4,500	Fink (2000)
Density	$\rho/(\mathrm{Mg{\cdot}m^{-3}}) = 8.860 - 9.285 \times 10^{-4}\,((T/K) - 3,120)$	3,120–7,600	Fink (2000)
Thermal conductivity	$\lambda/(\mathrm{W{\cdot}m^{-1}{\cdot}K^{-1}}) = 2.5$–$3.6$		IAEA (2006)
Vapor pressure[b]	$^{10}\log(p/\mathrm{MPa}) = 15.961 - \dfrac{26974}{(T/K)} - 2.7600\,^{10}\log(T/K)$	3,120–8,000	Fink (2000)
Viscosity	$\eta/(\mathrm{MPa \cdot s}) = 0.988 \exp\left(\dfrac{4,620}{(T/K)}\right)$	3,083–3,328	Fink (2000)

[a] 95% Theoretical density
[b] Total vapor pressure

like UO_2 is dominated by phonon heat transport at temperatures below about 1,500 K and is limited by two principal mechanisms: phonon–phonon interactions and phonon scattering (by lattice imperfections like vacancies or impurities). The thermal conductivity of such materials can generally be described by an equation of the type

$$\lambda = \frac{1}{A + BT} \tag{34.8}$$

where the coefficients A and B represent the effects of the phonon scattering and the phonon–phonon interaction, respectively. This equation suggests that the thermal conductivity decreases with increasing temperature, which is the case for UO_2 up to about 2,000 K. Above this temperature the electronic contribution becomes important as a result of which the thermal conductivity slightly increases again (Fig. 34.12).

The porosity is an important factor affecting the overall thermal conductivity of a ceramic like UO_2, that is generally not fully dense. Pores, which are filled with gas, poorly conduct the heat and thus act as thermal barriers. Many formulas have been suggested to take this effect into account, mainly assuming that in highly dense materials the pores have a spherical shape, which is generally the case for sintered UO_2. The Maxwell–Eucken correction is frequently used:

$$\lambda = \lambda_0 \frac{1 - P}{1 + \beta P} \tag{34.9}$$

Here λ_0 is the thermal conductivity of the fully (100%) dense material, P is the fractional porosity, and β is a constant, which is unity for perfect spherical

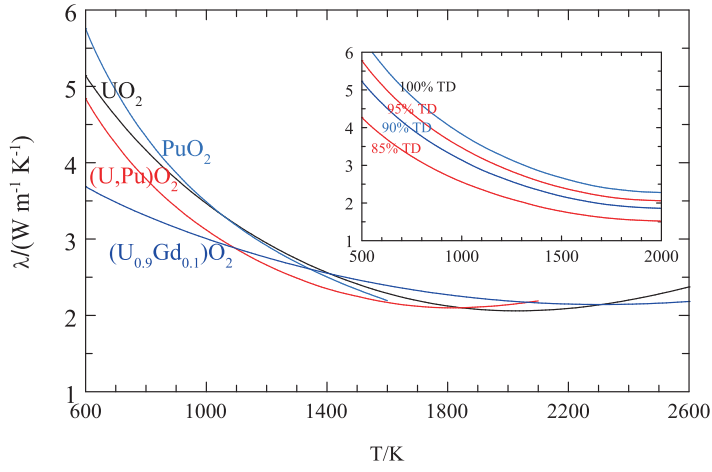

Fig. 34.12 *The thermal conductivity of UO_2, PuO_2, $(U,Pu)O_2$ and $(U_{0.9}Gd_{0.1})O_2$ as a function of temperature; the inset shows the thermal conductivity of UO_2 for various densities.*

pores. For complex pore shapes and distributions, the corrections are less straightforward. For example, by taking into account the influence of the shape, the orientation and the distribution of the pores typical for irradiated fuel (Bakker *et al.*, 1995; Bakker and Konings, 1996) derived the following correction by finite element calculations:

$$\lambda = \lambda_0(1-p)^{\beta} \tag{34.10}$$

where $\beta = 1.5$ is the lower limit for spherical porosity, randomly ordered. For other pores shapes β increases as a function of the microstructure characteristics, up to 1.7 for elliptical pores and up to 2.3 for complex shaped pore structures.

The thermal conductivity of stoichiometric UO_2 has been measured by many authors and these measurements were evaluated by an IAEA expert group (IAEA, 2006). The recommended equation for 95% dense material is:

$$\lambda = \frac{100}{7.5408 + 17.692t + 3.6142t^2} + \frac{6400}{t^{5/2}}\exp\left(\frac{-16.35}{t}\right) \tag{34.11}$$

where λ is the thermal conductivity in $W{\cdot}m^{-1}{\cdot}K^{-1}$, and $t = T/1{,}000$ in K.

Table 34.4 gives a complete overview of the recommended properties of stoichiometric UO_2 based on the assessment of Fink (2000) and the critical evaluation by the IAEA expert group (IAEA, 2006).

The properties of the uranium dioxide phase strongly vary as a function of the O/U ratio. As is evident from the phase diagram (Fig. 34.10), the melting point decreases for both the hypo- and hyperstoichiometric range. The variation of the chemical potential of oxygen (also called the oxygen potential) with the O/U ratio is very distinct. It reflects the equilibrium between oxygen in the crystal lattice and the gas phase:

$$2\left[O^{2-}\right]_{lattice} \rightleftarrows O_2(g) + 4e^- \tag{34.12}$$

The oxygen potential of this equilibrium is defined as

$$\mu(O_2) = RT\ln\frac{p(O_2)}{p^{\circ}} \tag{34.13}$$

where $\mu(O_2)$ is the chemical potential (often written as $\Delta\bar{G}(O_2)$), R is the universal gas constant, T the absolute temperature, $p(O_2)$ is the partial pressure of oxygen, and p° the standard pressure.

In the hypostoichiometric region the oxygen potential is relatively low, meaning that the oxygen is strongly bonded in the lattice. This can be understood from the fact that it is difficult to extract O^{2-} ions from the lattice sites. In the hyperstoichiometric region the oxygen potential is much higher, as the bonding of the O^{2-} ions in the interstitial sites is much weaker. Around O/U = 2.0 a rapid change of the oxygen potential is observed between the two regions (Fig. 34.13). This means that small differences in the O/U ratio close to 2 can lead to significant differences in the oxygen potential. The variation of the oxygen

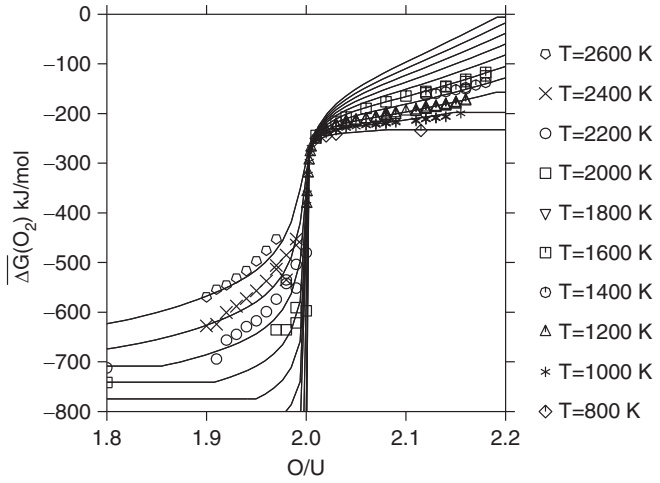

Fig. 34.13 *The oxygen potential of UO_2; the lines show the assessed values* (*Guéneau et al.*, 2002) *with* 200 *K intervals between* 800 *and* 2,600 *K, the symbols represent the various experimental studies. For meaning of the symbols see Guéneau et al.* (2002).

potential data versus O/U ratio and temperature is related to the evolution of the defect concentration in the crystal. Various proposals for the defect chemistry in $UO_{2\pm x}$ have been presented but are still subject of controversy.

Since $UO_{2\pm x}$ is characterized by lattice defects such as vacancies and interstitial substitutions, it is obvious that the thermal conductivity of uranium dioxide varies as a function of the O/U ratio (Fig. 34.14). The highest values are found for $UO_{2.00}$ whereas the hyper-stoichiometric compositions have lower values (Amaya *et al.*, 1996).

(b) Plutonium dioxide

At relevant temperatures no compounds with a Pu valence state higher than 4+ as in plutonium dioxide exist in the plutonium–oxygen system. PuO_2 is isostructural with UO_2, with a slightly smaller lattice parameter of the fcc lattice reflecting the somewhat smaller ionic radius of Pu^{4+} resulting from the actinide contraction. Also its other properties differ significantly, but not dramatically from those of UO_2.

The recommended melting temperature of PuO_2, (2,663 ± 40) K, is about 450 K lower than that of UO_2 (see Chapter 19), although doubt has been raised about this value recently (Kato *et al.*, 2008b). Like UO_{2-x} it shows a wide composition range for the fluorite phase at high temperatures, extending to about O/Pu = 1.6. Between the hexagonal sesquioxide Pu_2O_3 and PuO_2, the

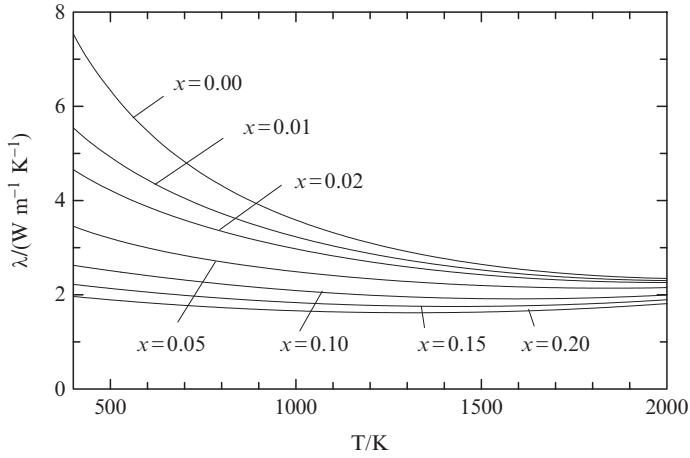

Fig. 34.14 *The thermal conductivity of UO_{2+x} for various values of x; after Amaya et al.* (1996).

intermediate phases $PuO_{1.52}$ (cubic) and $PuO_{1.61}$ (body-centered cubic structure) exist, leading to a complex phase diagram below 1,500 K. At low temperatures the value of x in PuO_{2-x} is small and the dioxide is in equilibrium with $PuO_{1.52}$. High temperature X-ray diffraction studies have shown the existence of a narrow miscibility gap in the fluorite phase PuO_{2-x} occurring at ~900 K. The $PuO_{1.61}$ phase has a notable composition range ($1.61 < O/Pu < 1.72$) and decomposes congruently into PuO_{2-x} around 1,450 K. The Pu–Pu_2O_3 region of the phase diagram is uncertain due to the lack of experimental data. A miscibility gap in the liquid state was observed at (2,098 ± 40) K like in the U–O system. The assessed phase diagram for the Pu–O system, taken from the recent assessment by Guéneau *et al.* (2008), is shown in Fig. 34.15.

The oxygen potential of PuO_{2-x} shows a behavior similar to that of UO_{2-x}, as shown in Fig. 34.16. However, the oxygen potential of PuO_{2-x} is considerable higher for similar O/M ratios and is constant in the region of demixing.

The thermal conductivity of PuO_2 can be described well by a classical phonon heat transport equation in the temperature range for which measurements exist. The results of Gibby (1971) for 97% dense material can be represented by:

$$\lambda = \frac{1}{4.6 \times 10^{-3} + 2.82 \times 10^{-4}(T/K)} \tag{34.14}$$

where λ is the thermal conductivity in $W \cdot m^{-1} \cdot K^{-1}$. Other physico-chemical properties of PuO_2 are given in Table 34.5.

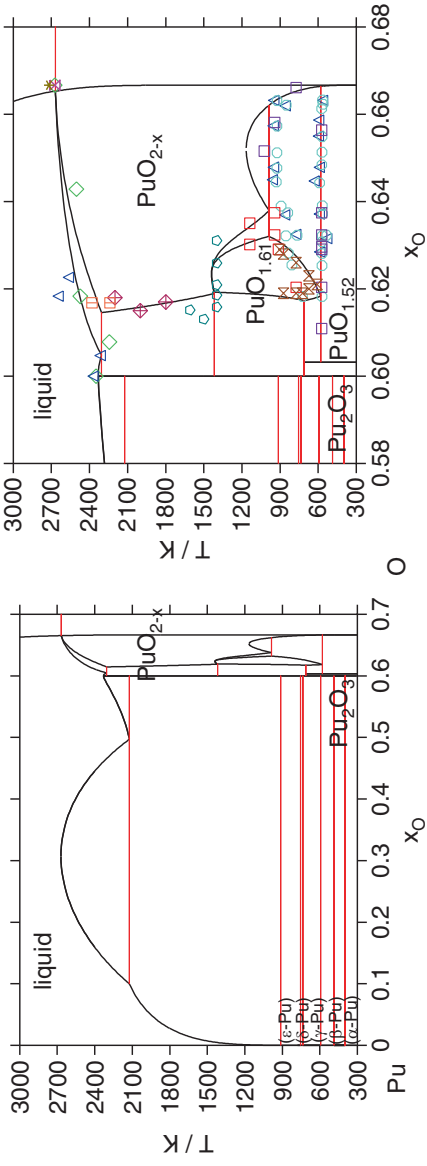

Fig. 34.15 *The Pu–O phase diagram.* (*After Guéneau et al.*, 2008).

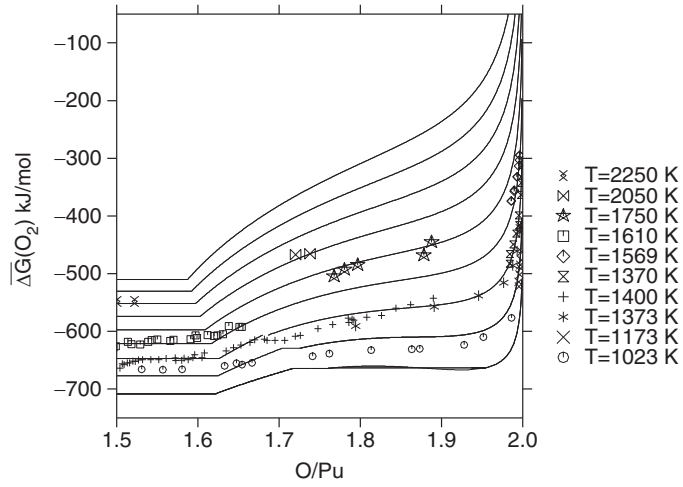

Fig. 34.16 *The oxygen potential of* PuO_{2-x}; *the lines show the assessed values* (*Guéneau et al.*, 2008) *with* 200 *K intervals between* 1,000 *and* 2,600 *K*, *the symbols represent the various experimental studies. For meaning of the symbols see Guéneau et al.* (2008).

(c) Oxides of the minor actinides

The oxides of the minor actinides (MA) neptunium, americium and curium all form fcc dioxides, but only NpO_2 is stable over a wide temperature range. AmO_2 starts losing oxygen at moderate temperatures (Chikalla and Eyring, 1968), and CmO_2 is not stable above 653 K (Mosley, 1972), indicating that for these elements the trivalent state is becoming increasingly stable. Cm_2O_3 is indeed the predominant curium oxide at high temperatures. In the case of the americium–oxygen system, the cubic AmO_{2-x} phase has a wide composition range at high temperatures, to about O/Am = 1.6. At temperatures below about 1,000–1,200 K, the AmO_{2-x} phase is in equilibrium with another cubic phase of a composition at about 1.62. No assessed phase diagrams for the Am–O and Cm–O systems have been reported; the tentative phase diagrams are shown in Fig. 34.17.

The most relevant thermophysical properties of the minor actinide oxides are summarized in Table 34.5. They differ slightly from those of the major actinides U and Pu. As discussed in Chapter 19, the thermodynamic properties of the dioxides and sesquioxides vary in a regular manner and can be described adequately by considering the electronic configurations. As shown in Fig. 34.18 the thermal conductivity of NpO_2 is close to that of the other fcc dioxides UO_2 and PuO_2. The thermal conductivity of the hexagonal Cm_2O_3 is significantly lower than that of the fcc dioxides. The thermal conductivity of the americium oxides have been subject of many discussions. The early measurements (at T = 303 K) by Schmidt (1975) suggest values around 0.7–0.8 $W{\cdot}m^{-1}{\cdot}K^{-1}$ for AmO_2

Table 34.5 *Thermophysical properties of the transuranium actinide oxides; T is the temperature in K.*

	Equation	T/K	Ref.
(a) PuO_2			
$\lambda/(W{\cdot}m^{-1}{\cdot}K^{-1})$	$\dfrac{1}{4.6\times10^{-3}+1.282\times10^{-4}(T/K)}$	373–1,474	Gibby (1971)
$C_p/(J{\cdot}K^{-1}{\cdot}mol^{-1})$	$36.2952 + 152.25\times10^{-3}(T/K) - 127.255\times10^{-6}(T/K)^2 + 36.289\times10^{-9}(T/K)^3 - 0.34759\times10^{6}(T/K)^{-2}$	298–2,633	Chapter 19
$L(T)$	$L_{273}(0.9975 + 8.616\times10^{-6}(T/K) + 1.886\times10^{-9}(T/K)^2)$		Nutt and Tokar (1972)
(b) NpO_2			
$\lambda/(W{\cdot}m^{-1}{\cdot}K^{-1})$	$\dfrac{1}{0.09447+1.797\times10^{-4}(T/K)}$	500–1,500	Nishi *et al.* (2008a)
$C_p/(J{\cdot}K^{-1}{\cdot}mol^{-1})$	$72.3668 + 15.69554\times10^{-4}(T/K) - 9.64173\times10^{5}(T/K)^{-2}$	300–1,100	Nishi *et al.* (2008a)
$L(T)$	$L_{273}(0.9982 + 7.054\times10^{-6}(T/K) + 1.806\times10^{-9}(T/K)^2 - 7.748\times10^{-9}/(T/K))$	298–1,573	Serizawa *et al.* (2001)
(c) AmO_2			
$\lambda/(W{\cdot}m^{-1}{\cdot}K^{-1})$	$\dfrac{1}{2.1\times10^{-2}+3.19\times10^{-4}(T/K)}$	298–1,500	Bakker and Konings (1998)
$C_p/(J{\cdot}K^{-1}{\cdot}mol^{-1})$	$84.739 + 10.72\times10^{-3}(T/K) - 0.8159\times10^{-6}(T/K)^2 - 1.9285\times10^{6}(T/K)^{-2}$	298–1,500	Thiriet and Konings (2003)
$L(T)$	$L_{273}(0.9976 + 7.054\times10^{-6}(T/K) + 2.655\times10^{-9}(T/K)^2)$	273–1,000	Fahey *et al.* (1974)
(d) Cm_2O_3			
$\lambda/(W{\cdot}m^{-1}{\cdot}K^{-1})$	$\dfrac{1}{0.3629+1.78\times10^{-4}(T/K)}$	298–1,400	Konings (2001)
$C_p/(J{\cdot}K^{-1}{\cdot}mol^{-1})$	$123.532 + 14.550\times10^{-3}(T/K) - 1.3469\times10^{6}(T/K)^{-2}$	298–2,000	Konings (2001)
$L(T)$	$L_{273}(0.99835 + 4.4449\times10^{-5}(T/K) + 3.6066\times10^{-11}(T/K)^2)$	273–1,700	Konings (2001)

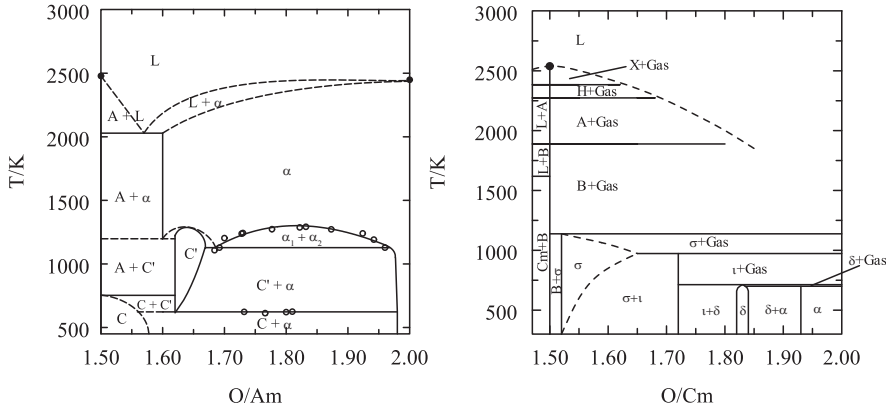

Fig. 34.17 *Left: The tentative americium-oxygen phase diagram in the region* $AmO_{1.5}$–AmO_2 ($p_{O_2} = 0.2$ *bar*), *as suggested by Thiriet and Konings* (2003); $\alpha = AmO_{2-x}$, $C = AmO_{1.5}$(*cubic*), $A = AmO_{1.5}$(*hex*). *Right: The tentative curium-oxygen phase diagram in the region* $CmO_{1.5}$–CmO_2 ($p_{O_2} = 0.2$ *bar*), *modified after Smith and Peterson* (1970) *by Konings* (2001); $\alpha = CmO_{2-x}$, $\delta = CmO_{1.83}$, $\iota = CmO_{1.71}$, $\sigma = CmO_{1.5+x}$(*bcc*), $B = CmO_{1.5}$(*mon*), $A = CmO_{1.5}$(*hex*), *H and X are high-temperature structure types.*

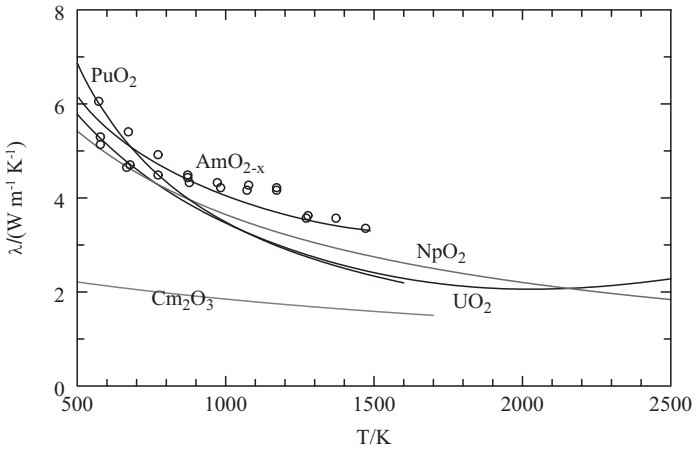

Fig. 34.18 *The thermal conductivity of the actinide oxides as a function of the temperature*; *the symbols show the experimental results for* AmO_{2-x}.

as well as Am_2O_3. This work has been disputed and (semi)empirical (Bakker and Konings, 1998; Lemehov *et al*., 2005) and molecular dynamic calculations (Uchida *et al*., 2009) suggest that the thermal conductivity of AmO_2 is close to that of the other actinide dioxides. Recent measurements by Nishi *et al*. (2008b) confirm this, but the authors observed a strong reduction of the sample during the heating, however, without the decrease due to the non-stoichiometry as known from UO_2 (see Fig. 34.18).

(d) Mixed oxides

(*i*) *The U–Pu–O system*

Uranium dioxide and plutonium dioxide form a solid solution in the complete composition range. Due to the differences in the ionic radii of U^{4+} and Pu^{4+} lattice strain effects can be expected, but these are generally not detectable in the high temperature properties. The phase diagram (Fig. 34.19) shows that the solid solution has a near ideal behavior for the solidus and liquidus curves. The solidus and liquidus were observed to decrease with increasing Pu content and increase slightly with decreasing oxygen to metal ratio in the region of hypo-stoichiometric composition (Kato *et al*., 2008a). Adamson *et al*. (1985) recommended the following equations for the UO_2–PuO_2 solidus and liquidus curves:

$$T_{solidus}/K = 3120 - 655.3x + 336.4x^2 - 99.9x^3 \quad (34.15)$$

$$T_{liquidus}/K = 3120 - 388.1x - 30.4x^2 \quad (34.16)$$

where x is the molar fraction of PuO_2.

However, the recent measurements by Kato *et al*. (2008b) are not in agreement with the results of Aitken and Evans (1968) and Lyon and Bailey (1967) from the 1960s, and report a melting temperature for pure PuO_2 about 200 K higher than the recommended value. Further experiments are required to solve this discrepancy.

The phase equilibria in the $UO_{2\pm x}$–PuO_2–Pu_2O_3 narrow region are complex. Hypo-stoichiometric $(U,Pu)O_{2-x}$ is known to be a single phase at high temper-

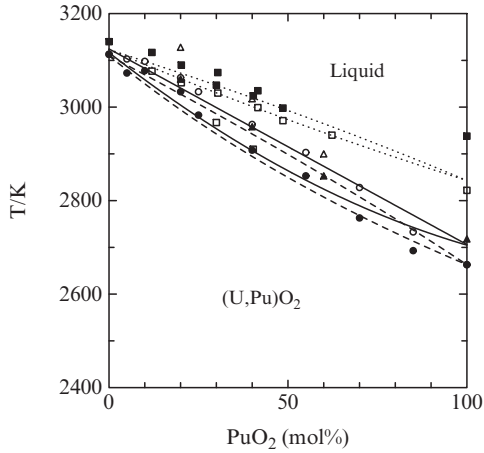

Fig. 34.19 *The pseudobinary phase diagram UO_2–PuO_2. The circles give the experimental data by Lyon and Bailey* (1967), *the triangles by Aitken and Evans* (1968), *and the squares by Kato et al.* (2008b). *The solid lines represent the recommended liquidus and solidus by Adamson et al.* (1985), *the broken line the ideal liquidus and solidus based on the results of Lyon and Baily*, *and the dotted line the liquidus and solidus suggested by Kato et al.* (2008b)

ature but becomes biphasic at low temperature (<773 K depending on both O/M ratio and Pu content), as reported by Markin and Street (1967), Sari and Zamorani (1970) and more recently by Kato *et al*. (2008b). These two-phase regions are formed from the extension of the complex Pu_2O_3–PuO_2 region into the ternary (see Fig. 34.15). Depending on the temperature and the O/M ratio, hypo-stoichiometric $(U,Pu)O_{2-x}$ for Pu content higher than 30 mol% is composed either of two fcc phases or of a single fcc phase in equilibrium with $PuO_{1.61}$ (bcc), $PuO_{1.52}$ or Pu_2O_3 (hexagonal) as shown in Fig. 34.20. Besmann and Lindemer (1986) and recently Agarwal *et al*. (2009) have developed simple thermochemical models to reproduce the available experimental data for the temperature of decomposition of the MOX fuels as a function of the Pu content and the oxygen/metal ratio.

Carbajo *et al*. (2001) critically evaluated the heat capacity and enthalpy data for $(U,Pu)O_2$ and concluded that the results for the solid phase can be described well by the Neumann–Kopp rule:

$$C_p(T, U_{1-y}\,Pu_y\,O_2) = (1-y)C_p(T, UO_2) + yC_p(T, PuO_2) \qquad (34.17)$$

There is still controversy about the effect of the plutonium content on the thermal conductivity of $(U,Pu)O_2$. Gibby (1971) measured this effect for $(U,Pu)O_2$ solid solutions up to 30 mol% PuO_2, observing a small but systematic decrease with increasing PuO_2 content (Fig. 34.21). This could be explained by the fact that the Pu^{4+} ions substitute on the uranium positions of the UO_2 lattice where they act as phonon scattering centers, in line with the theory of phonon scattering by point defects in dielectric solids. Schmidt (1970) found a different dependence on the PuO_2 content with a peak in the thermal conductivity at about 15 mol%, particularly evident at low temperatures (Fig. 34.21). Beauvy (1992), who reported similar results, attributed this to differences in the defect cluster concentrations below and above 12.5 mol% PuO_2. Clearly, further studies are needed as also the strong variation of the thermal conductivity close to O/M = 2.00 (see below) might have affected the results.

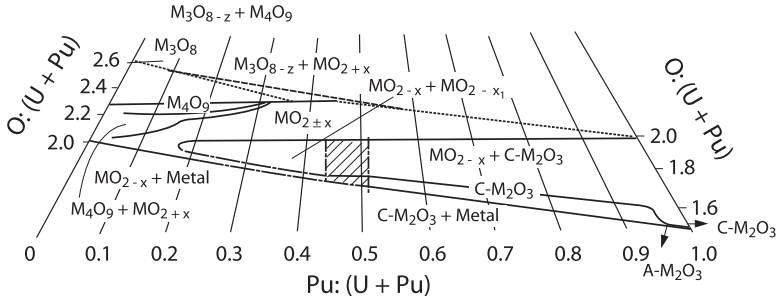

Fig. 34.20 *A section of the U–Pu–O phase diagram at T = 298.15 K, after Markin and Street* (1967).

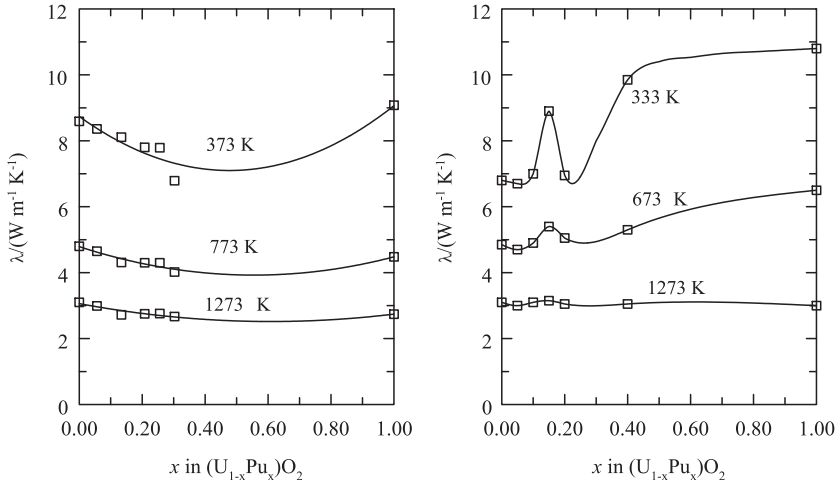

Fig. 34.21 *The thermal conductivity of* $(U_{1-x}Pu_x)O_2$ *of* 96–98% *theoretical density for various values of* x; *left: the results of Gibby* (1971), *right: the results of Schmidt* (1970).

Van Craeynest and Weilbacher (1968) and Schmidt (1971)[5] studied the effect of the O/M ratio on the thermal conductivity of $(U_{0.8}Pu_{0.2})O_{2-x}$, observing a strong decrease as a function of x, particularly at the lowest temperatures, which is due to the fact that Pu^{3+} ions and oxygen vacancies act as scattering centers in the crystal lattice. For the hyperstoichiometric range $(U_{0.8}Pu_{0.2})O_{2+x}$ they found a similar trend as for $UO_{2\pm x}$, i.e. the thermal conductivity decreases for positive as well as negative values of x, slightly asymmetric around O/M = 2.00. Philipponneau (as cited by Baron (1998)) assessed these and other studies and recommended the following (symmetric) equation for the variation of thermal conductivity of $(U_{0.8}Pu_{0.2})O_{2\pm x}$ as function of temperature (T) and x:

$$\lambda = \frac{1}{1.32(|x| + 0.31 \times 10^{-3})^{\frac{1}{2}} - 0.091 + 2.294 \times 10^{-3}(T/K)} + 8.84 \times 10^{-11}(T/K)^3 \tag{34.18}$$

as shown in Fig. 34.22, revealing a strong decrease for both the hyper- and hypostoichiometric range.

Duriez *et al*. (2000) made systematic measurements of the thermal conductivity of $(U,Pu)O_{2-x}$ mixed oxide fuel with homogeneous and heterogeneous (MIMAS type, see Section 34.5.2 (a)) microstuctures, for average Pu concentrations from 3 to 15 wt% and O/M 2.00–1.95, typical for LWR fuel, in the temperature range 700–2,300 K. The thermal conductivity was found to be

[5] see also Mattys (1968)

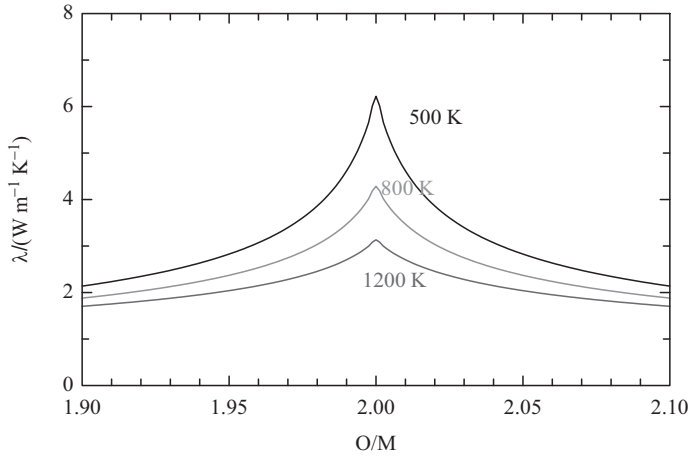

Fig. 34.22 *The thermal conductivity of* $(U_{0.80}Pu_{0.20})O_{2 \pm x}$ *as a function of x for various temperatures.*

significantly lower than that of the UO_2, and no dependence on the Pu concentration was found, but a clear decrease of the thermal conductivity as a function of the O/M ratio was observed. Their results expressed for 95% TD in this concentration range were represented by the equation (x = 2 − O/M is the non-stoichiometry):

$$\lambda = \frac{1}{A(x) + B(x)(T/K)} + \frac{C}{(T/K)^2}\exp\frac{-D}{(T/K)} \tag{34.19}$$

with $A(x) = 2.85x + 0.035$ m K/W, $B(x) = (2.86 - 7.15x)\ 10^{-4}$ m/W, C = 1.689 × 10^9 W K/m, and D = 13,520 K. However, Carbajo *et al.* (2001) argued that this equation does not reproduce the high temperature data (>2,000 K) correctly and suggested a combination of the results of Duriez *et al.* (2000) and Ronchi *et al.* (1999):

$$\lambda = \frac{1}{A(x) + B(x)(T/K)} + \frac{6400}{t^{5/2}}\exp\left(\frac{-16.35}{t}\right) \tag{34.20}$$

As discussed by Duriez *et al.* (2000), the experimental measurements generally refer to homogeneous samples and not to industrial samples in which an inhomogeneous distribution of PuO_2 can occur. For that reason they measured the thermal conductivity of commercial MIMAS mixed oxide fuel pellets. The results of these measurements did not significantly differ from the results obtained by equation (34.19).

Numerous experimental and theoretical studies have been carried out to determine the variation of the oxygen potential as a function of oxygen to metal ratio, plutonium content and temperature in $(U,Pu)O_{2\pm x}$. For the description of the oxygen potential, Markin and Rand (1966) suggested that the $(U,Pu)O_{2\pm x}$ solid solution can be considered as a mixture of UO_{2+x} + PuO_2 for the hyperstoichiometric range, and UO_2 + PuO_{2-x} for the hypostoichiometric range. Besmann and Lindemer (1985, 1986) have developed a solid solution model of the $(U,Pu)O_{2\pm x}$ mixed oxide on the basis of all available experimental data. In that extensively used model the solid solution is described by a mixture of the species $Pu_{4/3}O_2$, PuO_2, UO_2, $U_2O_{4.5}$ (or U_3O_7 for oxygen potential more positive than $-266{,}700 + 16.5(T/K)$ J/mol). The assessed oxygen potentials calculated using the Besmann and Lindemer model (Besmann and Lindemer, 1986) for $(U_{0.9}Pu_{0.1})O_{2\pm x}$ and $(U_{0.7}Pu_{0.3})O_{2\pm x}$ are shown in Fig. 34.23. The agreement between the calculated and experimental data close to the stoichiometry composition O/(U + Pu) = 2 is improved by replacing the species U_3O_7 by $U_2O_{4.5}$. The oxygen potential data measured for $(U,Pu)O_2$ fuels containing 20 and 30 mol% Pu were recently analyzed using a point defect model by Kato *et al*. (2009a). All studies and models indicate that the oxygen potential increases with temperature and plutonium content in $(U,Pu)O_{2\pm x}$.

(*ii*) *The U–Pu–MA–O system*

In next-generation fast reactors, small quantities of minor actinides will be added to the fuel. Therefore numerous studies focus on the effect of the addition of the minor actinides on both phase diagrams as well as thermodynamic and thermophysical properties.

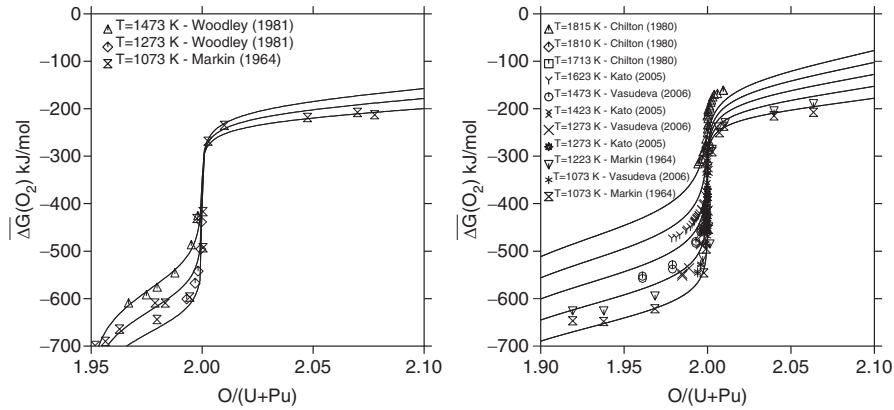

Fig. 34.23 *The oxygen potential of* $(U_{0.9}Pu_{0.1})O_{2\pm x}$ *at* 1,073, 1,273 *and* 1,473 *K* (*left*) *and* $(U_{0.7}Pu_{0.3})O_{2\pm x}$ *at* 200 *K intervals between* 1,073 *and* 1,873 *K* (*right*) *as derived from the model proposed by Besmann and Lindemer* (1985, 1986).

Kato *et al*. (2008a) found that the liquidus and solidus temperature decreases with the Am content. The effect of AmO_2 on solidus temperature was estimated to be about 4 K per 1% AmO_2. The influence of the minor actinides Np and Am on the decomposition of the single phase $(U,Pu,MA)O_{2-x}$ at high temperature to a two-phase microstructure (two fcc phases in the miscibility gap of the hypo-stoichiometric region) at low temperature has been investigated by Kato *et al*. (2006). The experimental results obtained by differential thermal analysis showed that the temperature of the phase separation decreases when the minor actinide content increases.

Small quantities of minor actinides also increase the oxygen potential noticeably as indicated in Fig. 34.24. The effect of adding minor actinides on oxygen to metal ratio is equivalent to or less than that of the accumulation of fission products during burn-up of 1 at.%. The oxygen potential of high content minor actinide samples $(U_{0.5}Am_{0.5})O_{2-x}$, $(U_{0.5}Np_{0.5})O_{2-x}$, and $(U_{0.6}Am_{0.2}Np_{0.2})O_{2-x}$ has been measured by Bartscher and Sari (1983, 1984, 1985), indicating that the presence of americium in the fuel leads to a significant increase of the oxygen potential compared to $(U_{0.7}Pu_{0.3})O_{2-x}$, particularly for the $(U_{0.5}Am_{0.5})O_{2-x}$ composition (Fig. 34.24).

In stoichiometric $(U,Pu)O_2$ with 30% Pu and small quantities of minor actinides, the lattice parameter of the fcc oxide phase decreases as the minor actinide content increases (Kato *et al*., 2006). Americium has a larger effect in comparison with neptunium. The experimental results are reproduced well by

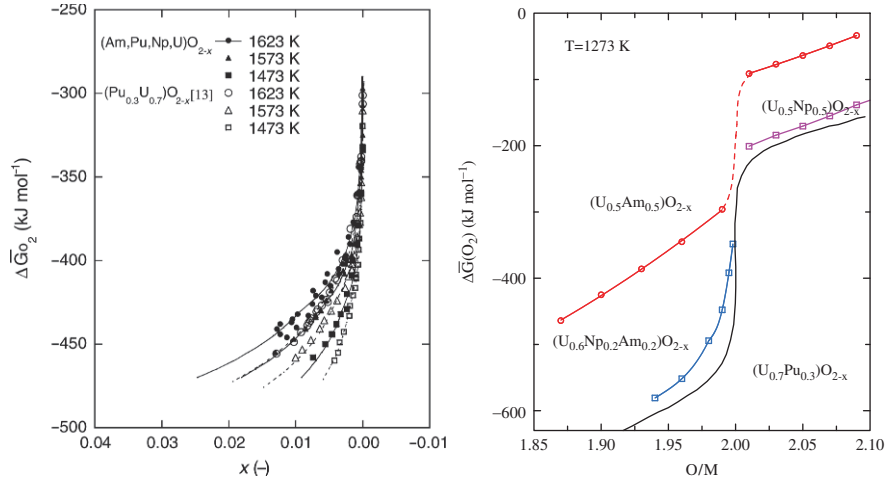

Fig. 34.24 *Left: The oxygen potential of* $(U_{0.66}Pu_{0.3}Np_{0.02}Am_{0.02})O_{2-x}$ *and* $(U_{0.7}Pu_{0.3})O_{2-x}$ (*Kato et al*., 2009b). (©*Elsevier*, 2009, *reprinted with permission*). *Right: The oxygen potential of* $(U_{0.5}Am_{0.5})O_{2-x}$, $(U_{0.5}Np_{0.5})O_{2-x}$, *and* $(U_{0.6}Am_{0.2}Np_{0.2})O_{2-x}$ *together with that of* $(U_{0.7}Pu_{0.3})O_{2-x}$. (*After Bartscher and Sari*, 1983, 1984, 1985).

Vegard's law. This means that MOX containing minor actinides is close to an ideal substitutional solution. In hypostoichiometric MOX, the lattice parameter (a) was found to increase with the decrease of the oxygen/metal ratio:

$$a(10^{-10}m) = 0.248x + a(\mathrm{MO_2}) \tag{34.21}$$

where x is the deviation from the stoichiometry (O/M − 2), and $a(\mathrm{MO_2})$ is the lattice parameter of the mixed oxide calculated using Vegard's law:

$$a(\mathrm{MO_2}) = \sum a_i \times c_i \tag{34.22}$$

where a_i is the lattice parameter of the ith AnO_2 end-member, and c_i is its concentration, defined as $c(\mathrm{NpO_2}) + c(\mathrm{AmO_2}) + c(\mathrm{PuO_2}) + c(\mathrm{UO_2}) = 1$ (Kato *et al.*, 2006). These data have been recently updated by Kato *et al.* (2009a) using X-ray diffraction for a broader composition range of solid solutions $(U_{1-z-y'-y''}Pu_zAm_{y'}Np_{y''})O_{2-x}$ (with $z = 0-1$, $y' = 0-0.12$, $y'' = 0-0.07$). A model based on the calculation of the ionic radius of the anions and cations from the lattice parameters was derived from the experimental database, representing the lattice parameter data of the fluorite phase as function of Pu content, minor actinide content and oxygen/metal ratio.

The addition of minor actinides decreases the temperature of the region of demixing present in the U–Pu–O system. The effect of americium is higher than that of neptunium (Kato *et al.*, 2006). This phase separation could cause micro-cracking of the pellet due to local volume change. As this process occurs at a temperature that is lower than that of the coolant liquid metal, it is concluded that the influence on the behavior of the fuel may not be significant.

The effect of the addition of minor actinides on the thermal conductivity is not very well known. Morimoto *et al.* (2008) studied the effect of small quantities of Am in mixed oxide fuel. They found that the thermal conductivity of $(U_{0.68}Pu_{0.30}Am_{0.02})O_{2-x}$ solid solutions ($x = 0.00-0.08$) is not significantly different from the equation for $(U,Pu)O_{2-x}$ recommended by Duriez *et al.* (2000). Schmidt *et al.* (1986) measured the thermal conductivity of $(U,Np,Am)O_{2-x}$ samples with high minor actinide content (MA/U = 1). They found that the thermal conductivity of the $(U_{0.50}Np_{0.25}Am_{0.25})O_{2-x}$ mixed oxide is close to that of standard $(U,Pu)O_{2-x}$ with similar O/M ratio. Also for high Am content $(U_{0.5}Am_{0.5})O_{2-x}$ the thermal conductivity is close to that of $(U,Pu)O_{2-x}$ with comparable O/M ratio. This indicates that vacancy formation has a stronger influence than anionic substitution. Schmidt *et al.* (1986) also observed that the thermal conductivity of $(U,Am)O_{2-x}$ exhibits an upswing above 1,800 K similar to UO_2 and $(U,Pu)O_2$, whereas the conductivity of $(U,Am)O_{2-x}$ continues to decrease with temperature as typical for a pure phonon conductor (e.g. ThO_2).

(e) $(U,Gd)O_{2-x}$

$(U,Gd)O_2$ is used as burnable poison fuel in nuclear reactors with extended fuel residence time, which requires higher initial enrichment. This higher amount of fissile material in the core must be compensated by the introduction of additional absorber materials such as Gadoliunium that disappear (burn) during the early irradiation period (first loading cycles).

The phase diagram of the UO_2–Gd_2O_3 system is not well known. It has been studied by Beals *et al.* (1969) using X-ray and thermal analysis and these authors found that a fluorite solid solution exists in the entire composition range when sintered in hydrogen. Up to about 80 mol% $GdO_{1.5}$ the fluorite phase is the only phase, above that composition it co-exists with monoclinic gadolinium sesquioxide. However, these results are suspicious because Gd_2O_3 has a body-centered structure, and a complete solution with fcc UO_2 is thus not possible. The phase diagram suggested by Beals *et al.* (1969) presents a different picture: the $(U,Gd)O_{2-x}$ solution is in equilibrium with UGd_3O_{11}, a compound not identified in their experiments. Kang *et al.* (2007) measured the liquidus and solidus of the $(U,Gd)O_{2-x}$ solid solution in the 4–12 wt% range. Their results for the liquidus are close to those of Beals *et al.* (1969) but those for the solidus are significantly higher. Their results can be presented by

$$T_{solidus}/K = 3120 - 48.01x + 1.31x^2 \tag{34.23}$$

$$T_{liquidus}/K = 3120 - 8.0x \tag{34.24}$$

where x is the weight fraction of Gd_2O_3.

The presence of Gd^{3+} ions in the UO_2 lattice causes local distortion, lattice strain and an increase of oxygen defects (vacancies). This has an impact on the phonon–lattice and phonon–phonon interactions, leading to a decrease of the thermal conductivity of $(U,Gd)O_{2-x}$. Following the recommendation by an IAEA expert group (IAEA, 2006), the recommended thermal conductivity equation (95% TD) is that by Ishimoto *et al.* (1994), valid for the temperature range 300–3,000 K:

$$\lambda = \frac{\lambda_0}{x}\arctan(x) + 3.94 \times 10^{-11}(T/K)^3 \tag{34.25}$$

$$x = 3.31\exp(-7.61 \times 10^{-4}(T/K))\sqrt{y\lambda_0} \tag{34.26}$$

where y is the Gd_2O_3 content. λ_0 is the thermal conductivity of point defect free UO_2:

$$\lambda_0 = \frac{1}{0.0245 + 2.46 \times 10^{-4}(T/K)} \tag{34.27}$$

The IAEA expert group (IAEA, 2006) also gave recommendations for the thermal expansion and heat capacity of $(U_{1-y}Gd_y)O_2$ based on critical review of the existing experimental data. For the linear thermal expansion ($L(T)$/

$L(273\ K)$) the recommended equation is:

$$L(T)/L(273K) = 0.99866 + 7.2512 \times 10^{-6}(T/K) + (2.0463 \times 10^{-13}y^2 + 3.4846 \times 10^{-11}y + 2.0653 \times 10^{-9})(T/K)^2 \quad (34.28)$$

and for the heat capacity (298.15–2,000 K)

$$C_p = C_{p0} + \Delta C_p \quad (34.29)$$

$$C_{p0} = 79.8 + (0.1263y^2 - 0.0073y + 0.0061)(T/K) - (1.68 - 1.48y) \times 10^6)(T/K)^{-2} \quad (34.30)$$

ΔC_p is expressed as

$$\Delta C_p = \frac{\Delta H^*}{\sqrt{2}RT^2}\exp\frac{\Delta S^*}{2R}\exp\frac{\Delta H^*}{\sqrt{2}RT} \quad (34.31)$$

where $\Delta H^* = (-73880y^3 + 10190y^2 - 612.13y + 310) \times 10^3$ J·mol^{-1} is the enthalpy of formation of Frenkel pair formation and $\Delta S^* = 61.969 - 45.564y$ J·K^{-1}·mol^{-1} is the entropy of formation of Frenkel pair formation. These Frenkel pairs of oxygen are formed because the substitution of Gd^{3+} on the uranium lattice creates oxygen vacancies on the oxygen sub-lattice. To maintain nearly stoichiometric composition (U,Gd)O_2, an oxygen interstitial must form (together with U^{5+} formation). As discussed in (IAEA, 2006) the entropy and enthalpy of formation per Frenkel pair thus obtained are higher than the values known from UO_2, but when extrapolated to zero Gd content, they are in fair agreement with the estimated values for UO_2.

The oxygen potential of $(U_{1-y}Gd_y)O_{2\pm x}$ solid solutions is close to that of $UO_{2\pm x}$ near $x = 0$. In the hypostoichiometric range the oxygen potential of $(U_{1-y}Gd_y)O_{2\pm x}$ is higher than UO_{2-x} showing the stabilizing effect of the Gd^{3+} substitution. The oxygen potential becomes more positive with increasing Gd content (Une and Oguma, 1983).

(f) $(Th,U)O_{2+x}$ and $(Th,Pu)O_{2-x}$

ThO_2 and UO_2 form a continuous of fcc solid solution series (Lambertson *et al.*, 1953) and lattice parameter measurements show that Vegard's law is obeyed. The experimental solidus and liquidus temperature can be described with an acceptable agreement assuming an ideal solid and liquid mixture (Fig. 34.25). Also ThO_2 and PuO_2 form a solid solution in the whole composition range (Freshley and Mattys, 1962). The only experimental study of the solidus temperatures in this system suggest non-ideal solution behavior, but the melting temperature of the PuO_2 end-member measured in that study is

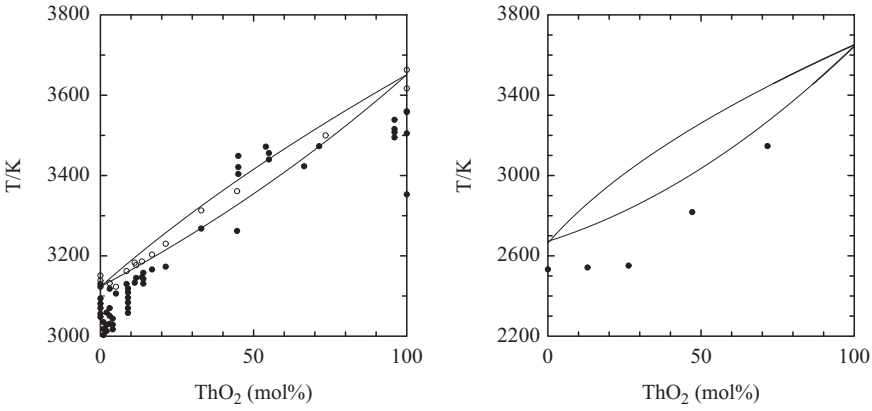

Fig. 34.25 *The pseudobinary UO_2–ThO_2 (left) and PuO_2–ThO_2 phase diagrams. The solid lines represent the liquidus and solidus assuming ideal solution behavior in the solid and liquid solutions, the closed symbols show the experimental data for the solidus and the open symbols for the liquidus (see Bakker et al., 1997 for details).*

about 130 K below the currently accepted value, as shown in Fig. 34.25 that compares the experimental results with the calculated ideal solidus and liquid temperatures.

The thermal properties of the (Th,U)O_2 and (Th,Pu)O_2 solid solutions have been evaluated by Bakker *et al.* (1997) and an IAEA expert group (IAEA, 2006). Experimental data exist for a wide composition range of the (Th,U)O_2 solid solution, with the emphasis on the range 0−30 wt% UO_2, but very few experimental results exist for the (Th,Pu)O_2 solid solution. The experimental data for these solid solutions indicate that thermal expansion can be interpolated between the end-members with an acceptable accuracy. In these reviews no recommendation was given for the heat capacity of the (Th,U)O_2 and (Th,Pu)O_2 solid solutions, because the experimental enthalpy data are not conclusive. The additivity rule (Neumann–Kopp) was considered to be appropriate to estimate the heat capacity of these solid solutions. Their thermal conductivity was found to decrease with increasing UO_2 or PuO_2 content, consistent with increasing thermal resistivity caused by lattice strain resulting from cation replacement. The recommended thermal conductivity equations are given in Table 34.6.

The oxygen potential of the $(Th_{1-y}U_y)O_{2+x}$ solid solution is close to that of UO_{2+x} for small values of x but slightly higher when x becomes larger (Ugajin, 1982). The oxygen potential decreases with increasing thorium content, similar to $(U_{1-y}Pu_y)O_{2+x}$, which can be explained by an increasingly non-ideal behavior when the uranium valence state increases (Fig. 34.26).

Table 34.6 *Thermal conductivity (95% theoretical density) and thermal expansion of ThO_2, $(Th,U)O_2$ and $(Th,U)O_2$.*

	Equation	*T/K*	*Ref.*
(a) ThO_2			
$\lambda(y,T)/(W{\cdot}m^{-1}{\cdot}K^{-1})$	$\dfrac{1}{4.20\times10^{-4}+2.25\times10^{-4}(T/K)^{a}}$	298–2,200	Bakker *et al.* (1997)
$\Delta L/L(293\ K)$	$-0.179+5.097\times10^{-4}(T/K)+3.732\times10^{-7}(T/K)^2-7.594\times10^{-10}(T/K)^3$	298–2,000	Bakker *et al.* (1997)
(b) $(Th_{1-y}U_y)O_2$			
$\lambda(y,T)/(W{\cdot}m^{-1}{\cdot}K^{-1})$	$1/[-0.0464+0.0034y+(2.5185\times10^{-4}+1.0733\times10^{-7}y)(T/K)]$	873–1,873	IAEA (2006)
(c) $(Th_{1-y}Pu_y)O_{2-x}$			
$\lambda(y,T)/(W{\cdot}m^{-1}{\cdot}K^{-1})$	$1/[-0.08388+1.7378y+(2.62524\times10^{-4}+1.7405\times10^{-4}y)(T/K)]$	873–1,873	IAEA (2006)

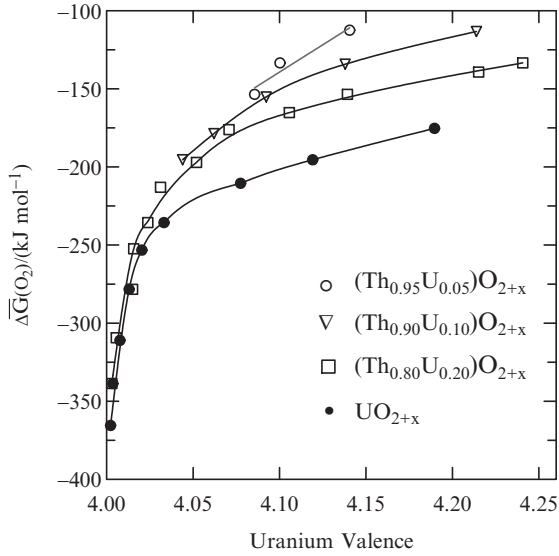

Fig. 34.26 *The oxygen potential of $(Th_{1-y}U_y)O_{2+x}$ at 1,473 K for various values of y. (After Ugajin, 1982)*

34.5.2 Oxide fuel fabrication

(a) Uranium dioxide

The UF_6 from the uranium enrichment must be converted to a uranium dioxide powder for the fabrication of dense nuclear fuel pellets. Three industrial

processes are currently used for this step (Assmann and Stehle, 1979), as schematically shown in Fig. 34.27.

In the ADU process the UF_6 is converted by a controlled reaction with aqueous ammonia to form ammonium diuranate (ADU) in a two step reaction:

$$UF_6(g) + 2H_2O(sln) = UO_2F_2(sln) + 4HF(sln) \tag{34.32}$$

$$2UO_2F_2(g) + 6NH_4OH(sln) = (NH_4)_2U_2O_7(cr) + 4NH_4F(sln) + 3H_2O(sln) \tag{34.33}$$

In this reaction a wet precipitate is formed that is heated to give the dry ADU. The dry ADU powder is then converted to UO_2 by heating it in Ar/H_2 gas:

$$(NH_4)2U_2O_7(cr) + 2H_2(g) = 2UO_2(cr) + 2NH_3(g) + 3H_2O(g) \tag{34.34}$$

The material thus obtained is then milled to obtain a powder with controlled properties such as specific surface area, tap density, mean size and morphology. The so-called ex-ADU powder normally consists of small particles with little internal porosity (Assmann and Stehle, 1979).

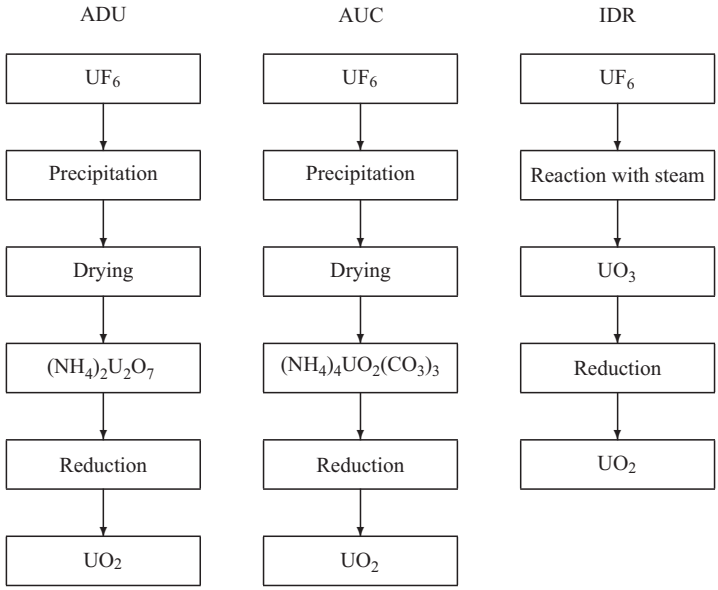

Fig. 34.27 *Schematic representation of ADU, AUC and IDR processes used for the production of reactor grade uranium dioxide powder.*

In the AUC process the UF_6 is converted by a controlled reaction with aqueous ammonia and carbon dioxide gas to form ammonium uranyl carbonate (AUC):

$$\begin{aligned} UF_6(g) + 5H_2O(sln) + 10NH_3(sln) + 3CO_2(g) \\ = (NH_4)_4UO_2(CO_3)_3(cr) + 6NH_4F(sln) \end{aligned} \tag{34.35}$$

The wet precipitate formed is heated to give the dry AUC and the dry AUC powder is converted to UO_2:

$$(NH_4)_4UO_2(CO_3)_3(cr) + H_2(g) = UO_2(cr) + 3CO_2(g) + 4NH_3(g) + 3H_2O(g) \tag{34.36}$$

The ex-AUC powder consists of large particles with intergranular porosity (Assmann and Stehle, 1979).

In the integrated dry route (IDR) or dry conversion (DC) process the UF_6 reacts with steam to form uranium oxyfluoride in a rotary kiln:

$$UF_6(g) + 2H_2O(g) = UO_2F_2(cr) + 4HF(g) \tag{34.37}$$

The product of this reaction is subsequently reacted with steam to form uranium trioxide, which in turn is reduced to uranium dioxide:

$$UO_2F_2(cr) + H_2O(g) = UO_3(cr) + 2HF(g) \tag{34.38}$$

$$UO_3(cr) + H_2(g) = UO_2(cr) + H_2O(g) \tag{34.39}$$

or directly reduced with hydrogen. The dry process has the major advantage that the criticality risk is significantly reduced. Also the amount of process waste is lower.

The UO_2 pellets are made by bi-axial pressing of the powder (Fig. 34.28). For this purpose the powder is blended with lubricants (e.g. zinc stearate) to facilitate the pressing process, particularly to reduce the stresses during ejection from the pellet matrix, and to obtain higher green densities. Also pore formers can be added in case of a high sinterability of the starting powder. This can be U_3O_8 or an organic pore forming material. In case the starting UO_2 powder has poor flow properties a granulation step is generally introduced before compaction. The homogenized mixture of powder, pressing aids and pore former is precompacted in a press and the compacts are then ground. Generally a specific particle fraction of the product is then selected by sieving (Assmann, 1982).

Originally the fuel pellets had flat faces but nowadays most fuel pellets have dished faces to anticipate for the radial anisotropic expansion behavior of the fuel pellets during irradiation (see below). Also chamfering of the pellet faces is often used, as this also helps the pellet fabrication (Fig. 34.29). Annular pellets are being used in the AGRs and VVERs, in which the pellets have a small central hole to reduce fuel centerline temperature.

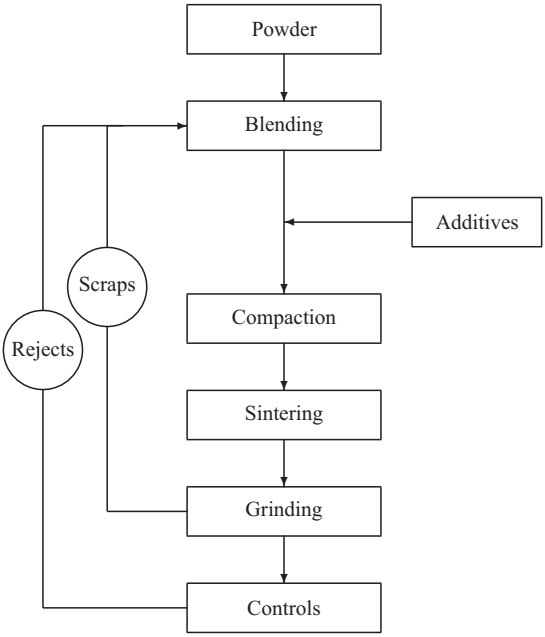

Fig. 34.28 *Schematic representation of the nuclear fuel pellet fabrication processes.*

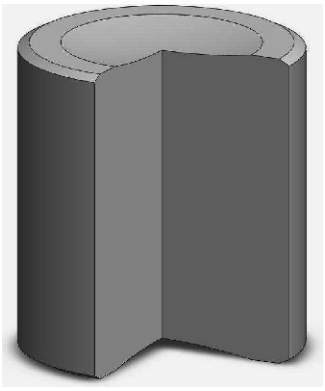

Fig. 34.29 *Schematic representation of a fuel pellet with dish and chamfer.*

After the compaction in a press, the so-called *green* pellets are obtained, which are still relatively fragile since they consist of compacted granules. Their density is about 50–60% of the theoretical density (TD) of UO_2. To obtain the required density of about 95% TD the green pellets are sintered at high

temperature during which the compacted grains grow together and the pellet densifies. This sintering occurs at temperatures between 1,600°C and 1,700°C in an atmosphere of pure hydrogen or argon/hydrogen. The hydrogen is required to obtain an O/U ratio of 2.00. Since the diameter of industrial pellets is defined with a (very) small tolerance, and the sintered pellets generally have a slight hour-glass shape, the pellets must be ground to meet the technical specification. This is generally done by centerless grinding. The grinding scraps of this process are not disposed off as waste but are recycled with the input powder of the fabrication process, as are rejects, i.e. pellets not meeting the specification.

With this process UO_2 pellets with grains/crystals of about 8–10 μm are obtained (Fig. 34.30), though the exact microstructure depends on the starting material (ADU, AUC, IDR). The about 4–6% porosity in the material is principally closed, which means that the pores dominantly occur in the grains or on the grain boundaries without, however, forming networks. The fabrication porosity serves as a sink for the fission gases produced during irradiation. However, the porosity is an important factor affecting the thermal conductivity (but not the other intrinsic properties) as pores filled with poorly conducting gas reduce the heat flow in the material.

Larger grains are considered advantageous to limit the fission gas release (see below) and for that reason industry is now further developing large grain fuels by the use of additives. Killeen (1980) already observed in 1980 that doping of UO_2 with Cr_2O_3, soluble to a limited extent in UO_2, leads to much larger grain size (seven times larger than undoped material), but found no difference in

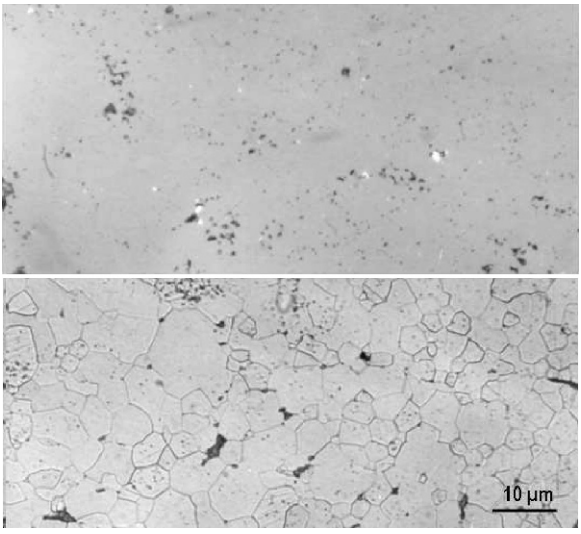

Fig. 34.30 *The microstructure of sintered UO_2 pellets*; *unetched* (*top*) *and etched* (*bottom*) *ceramographic images.* (©*European Communities*, *reproduced with permission*).

fission gas release. Chromia-doped UO_2 fuel was further developed in France (Valin *et al*., 2003). The average grain size was found to be 60 μm when doped with 2,000 ppm Cr_2O_3, compared to 8 μm in standard UO_2. An improvement was found for fission gas release during ramp tests and in out-of-pile tests. The viscoplasticity of the fuel also improved, an advantage with respect to pellet–cladding interaction (PCI).

(b) Mixed oxide

The term mixed oxide (MOX) is generally used for nuclear fuel made of a mixture of natural or depleted UO_2 and reprocessed PuO_2, the latter being produced by oxalate precipitation of the plutonium from a nitric acid solution followed by calcination of the product at about 723 K. The fraction of the reprocessed plutonium in MOX varies as a function of the amount of fissile isotopes (^{239}Pu, ^{241}Pu), but in LWRs it is generally below 10%, to match the enrichment of the uranium oxide fuel in the reactor.

Due to the high (α) radiotoxicity of plutonium, the fabrication of mixed oxide must be performed in hermetically tight glove boxes, to avoid its dispersal that can lead to inhalation and ingestion. Because separated plutonium generally contains ^{241}Am, the decay product of ^{241}Pu, the glove boxes are additionally lead shielded to protect against gamma radiation (69 keV).

Mixed oxide fuel can be produced by simply mixing and milling UO_2 and PuO_2 powders, followed by compacting and sintering. Although a complete miscibility of the two compounds exists in the solid and liquid states, the diffusion of the Pu into the UO_2 lattice is slow at the sintering temperature commonly applied and an inhomogeneous material is obtained. For that reason other processes have been developed (Assmann *et al*., 1988).

In the Mimas process (micronized master blend), which is the industrial process used by Areva in France for LWR fuel, a first mixture containing slightly less than 30% PuO_2 is fabricated by ball milling (Fig. 34.31).[6] After forced sieving to select the required powder size fraction, this primary blend is mixed with UO_2 powder to obtain the required Pu concentration. Next the powder is compacted and sintered in moistened Ar/H_2 to obtain dense pellets with a O/M of 1.99–2.00. The microstructure of these pellets shows Pu-free U-rich agglomerates and Pu-rich agglomerates, indicating that a complete homogenization has not been obtained (Fig. 34.32). These agglomerates are separated by a phase whose plutonium content is between 0 and that of the master blend (Oudinet *et al*., 2008). The Pu-rich spots are small but, exceptionally, can reach sizes of about 150 μm. The Pu concentration does not exceed that in the primary blend, which guarantees dissolution in the reprocessing. As a result a large fraction (25–50%) of the total Pu in the fuel is concentrated in the

[6] Siemens-KWU developed a similar process under the name OCOM (Optimised Co-Milling).

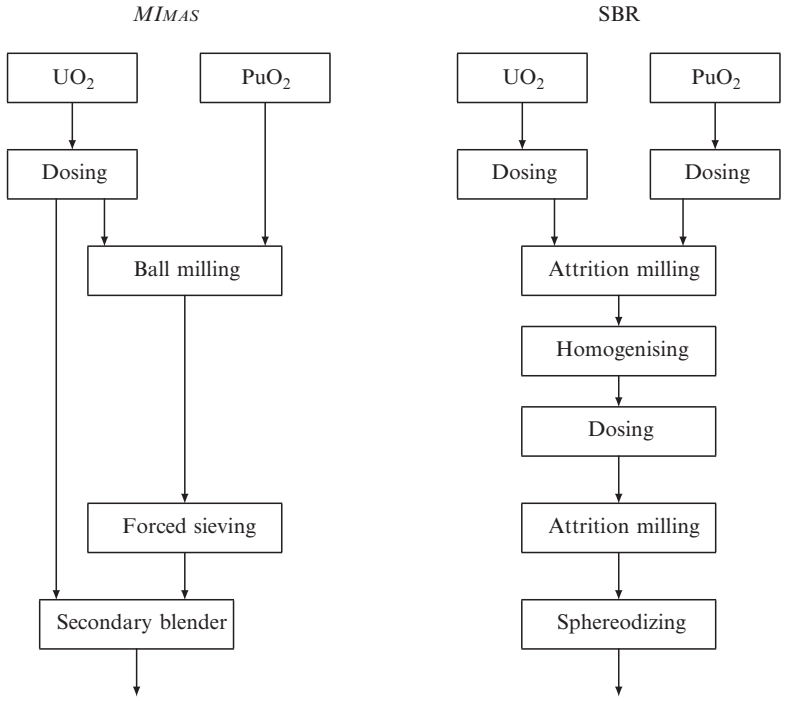

Fig. 34.31 *Schematic representation of the MIMAS and SBR processes used for the production of powders for mixed oxide fuel.*

Pu-spots. However, this inhomogeneity has been considered acceptable and fuels of this type have been irradiated in European reactors during many years now. However, to improve the process the use of additives has been extensively studied. Additives like sulphur, Cr_2O_3 or bentonite (an aluminium phyllosilicate) have been found to have a positive effect on the homogenization and at the same time enhance grain growth.

In the SBR (short binderless route) process used by BNFL in the UK, the UO_2 and PuO_2 are mixed and milled in several stages in an attrition mill to obtain a homogeneous powder that after compacting and sintering yield a rather homogeneous microstructure (Fig. 34.31). Very few Pu-rich spots are present in SBR MOX.

Mixed oxide fuels for fast reactors contain significantly more plutonium, generally between 15% and 30% PuO_2, and eventually more if the reactor is designed as a plutonium burner. The major difference with LWR MOX is thus that the Pu concentration in Pu rich islands in the fuel can be high, which may affect the dissolution of the spent fuel. The $(U,Pu)O_2$ mixed oxide is only fully soluble in nitric acid for concentrations below 40% PuO_2.

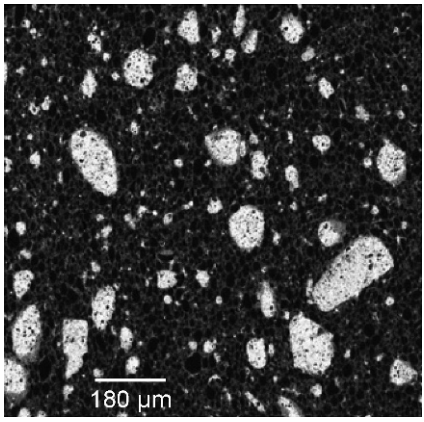

Fig. 34.32 *An electron microprobe X-ray map of an industrial Mimas MOX pellet, where dark colors correspond to low plutonium concentrations* (*Oudinet et al.*, 2008). (©*Elsevier*, 2008, *reprinted with permission*).

This can be overcome by starting the fabrication from aqueous solutions. In Germany (ALKEM) the AUPuC (ammonium–uranyl–plutonyl carbonate) process was developed for that purpose, which is based on co-conversion from a solution obtained by mixing uranium and plutonium solutions from the reprocessing plant (Assmann *et al.*, 1988). However, in practice the product from the reprocessing is currently a plutonium oxide powder. In that case mechanical mixing processes are preferred, similar as for LWR MOX. In France the fast reactor mixed oxide fuels have been produced by co-milling of the UO_2 and PuO_2 powders (COCA process). In this process the powders are blended and milled, then either sieved or granulated and finally pressed and sintered.

For fast reactor fuel the oxygen-to-metal ratio of the oxide fuel can be lower than 2.00. In the past fuels with O/M between 2.00 and 1.93 have been used. The lower O/M values (about 1.95) are advantageous to control the pellet–cladding chemical interaction and to maintain the integrity of the fuel pin at high burnup, but have a negative impact on thermal conductivity and melting point and thus decrease the margin to melting. The fuel (smear) density of fast reactor oxide fuel is generally lower than LWR fuel to accommodate fission gas induced swelling: by a higher initial porosity (10–20%), or annular design. The former also has a penalty on the thermal conductivity. In practice a compromise between the various parameters has to be found.

(c) Gd-doped uranium dioxide

A two-step process is also used for the fabrication of Gd-doped fuel. Typical Gd_2O_3 concentrations are 2–10 wt% (Assmann *et al.*, 1988). For the pellet fabrication gadolinium powder (Gd_2O_3, gadolinia) of well defined particle size

is blended with uranium oxide powder in two steps. First, a master blend with a gadolinia content of about 50% is produced. This master blend is then further blended with uranium oxide powder to the required gadolinium concentration.

The pellet specification for gadolinia-doped fuel is very strict. It requires that the largest fraction, generally at least 94%, of the added gadolinia dissolves in the uranium dioxide matrix. The remaining 6% may exist as free, (unreacted) Gd_2O_3-particles larger than 20 μm. Of these, 2% may exist as particles in the range 40–100 μm. No particle may be larger than 100 μm. (Assmann *et al.*, 1988).

(d) Minor actinide containing mixed oxide

For the next-generation nuclear reactors, the recycling of minor actinides (Np, Am, Cm) in the fuel is considered, the goal being their destruction (transmutation) by neutron fission. Fuels with low (a few percent) and high content (up to 40%) of minor actinides are studied, especially for fast reactors. The former is the case when the minor actinide pins are distributed homogeneously in the reactor core, the latter for the case that they are concentrated in dedicated fuel elements and specific core regions.

Because of the stronger radiation dose of the typical minor actinide nuclides (^{241}Am, ^{243}Am, ^{244}Cm) shielding of the fabrication facilities is required (Konings and Haas, 2002). The γ dose rates are orders of magnitude higher than uranium or even plutonium, which means that lead shielding is a prerequisite. In addition, the neutron dose rate due to spontaneous fission is very high for some curium isotopes, which requires further shielding with materials with high hydrogen density such as water or polyethylene. Finally the thermal power produced by the decay of ^{244}Cm is significant and necessitates forced cooling when storing larger quantities of this material.

During the conventional powder blending process and especially during the blending/milling phase needed to get a homogeneous material, dust formation is difficult to avoid and thus contamination of the working space of the fabrication cells is a risk, which is unwanted when working with such highly radioactive materials. The use of liquid processing of the separated elements after reprocessing/partitioning is a means to produce mixed oxide powders as starting materials and can mitigate the dust formation.

As discussed by Grandjean *et al.* (2007) co-conversion to process a mixture of actinides after treatment of spent fuel producing the starting mixed oxide for the fabrication of fresh fuel, is a promising route. The co-conversion/co-processing of actinides has as important advantages that the fabrication process is simplified and thus suited for remote handling and that a homogeneous starting product for fuel fabrication is obtained. The disadvantage is the liquid processing, which increases the criticality risks. Several co-conversion/co-processing processes have been studied (Grandjean *et al.*, 2007):

- Co-precipitation based on oxalate is the current method to process the separated plutonium. This process can be extended to the minor actinides as demonstrated at the laboratory scale, the so-called COEX process (Grandjean *et al.*, 2007).
- Co-gelation (sol-gel) is based on the formation of a gel after destabilizing a colloidal sol by the hydrolysis reactions. This can be achieved by the *External Gelation Process*, in which droplets of a concentrated solution containing actinides and a polymeric substrate are dispersed mechanically and then solidified by reaction with aqueous ammonia. In the case of *Internal Gelation* the solidification is initiated by the thermal decomposition of an ammonia precursor present in the actinide solution (e.g. hexamethylenetetramine, HMTA), by dispersing the droplets into a hot oil.

The sol-gel produced powders are generally free-flowing (i.e. they produce little or no dust). When produced with a polydisperse grain size the material can be pressed and processed in a conventional way. The disadvantage is the use of ammonia for the gelation, which in combination with the nitrate present in the actinide solution, can lead to formation of ammonium nitrate which poses an explosion risk.

(e) $(Th,U)O_2$ and $(Th,Pu)O_2$

Mixed thorium–uranium and thorium–plutonium oxide fuel can be fabricated by conventional processes consisting of mixing, pressing and sintering steps. However, because it is difficult to obtain homogeneous distribution of the U or Pu in the thorium oxide matrix, due to the slow diffusion kinetics at the sintering temperatures, aqueous precipitation processes have been developed widely (Assmann *et al.*, 1988).

Gel-supported precipitation (GSP) or ex-gel conversion technique has been studied extensively for the fabrication of thorium-based fuels, especially in India, where a strong development effort has been made. This process is based on the co-dissolution of thorium nitrate and uranyl nitrate in water and the conversion using co-gelation as described in the previous section.

34.5.3 The LWR fuel pin and fuel element

(a) The fuel pin

The LWR fuel pin (also called fuel rod) consists of a column of oxide fuel pellets enclosed in a metallic structure, the cladding (Fig. 34.33). The fuel pin is a tight encapsulation that serves as a barrier between the fuel and the coolant. A small gap of about 80–100 μm under cold conditions (160–200 μm diametrically) is present between the pellets and the cladding, meaning that the pellet outer diameter is slightly smaller than the cladding inner diameter. The gap is needed to facilitate the loading of the pellets, but also to anticipate for the swelling of

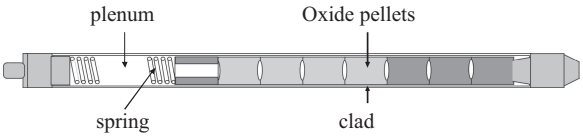

Fig. 34.33 *Schematic representation of a LWR fuel pin*; *not to length scale*.

the fuel pellets during irradiation (see below). The pellets are kept in place in the pin by a metallic spring that is mounted on the top of the pellet stack. The free volume around the spring (the plenum) serves as buffer volume for the fission gas that is released during the irradiation to avoid that the pressure inside the pin will raise to unacceptable values.

Before closing by welding the end-plug on the top, the PWR pin is pressurized with helium gas (20–25 bar) to assure that fuel-cladding gap and the plenum are filled with gas. Helium is chosen as it is inert and has the best thermal conductivity among the inert gases. BWR fuel rods are backfilled with helium to a pressure of about 3 bar.

The dimensions of fuel pins differ significantly between the various reactor designs. For example in PWRs the pins are about 400 cm in length and 9–11 mm in diameter, in BWRs 400 cm in length and 12–14 mm in diameter.

(b) The cladding

As for the fuel, the cladding material must meet several criteria considering its nuclear and material properties.

- Low neutron capture cross section of the constituting elements
- Compatible with the coolant
- Favorable physical properties, especially high thermal conductivity and high melting point
- Good mechanical stability (creep, yield strength and ductility)
- Good radiation stability (low void swelling and no embrittlement)
- Low permeability for fission gases and helium

In practice only a limited number of elements fulfill these criteria. Zirconium has been found to be the best material. However, this needs to be a special grade of zirconium, with very low content of hafnium, an element with very similar chemical properties but very different nuclear properties (it is a strong neutron capturing material).

Since pure Zr metal is too brittle for practical use various alloys of this metal have been developed and used. Zircaloy, an alloy of zirconium and tin, has initially been developed to overcome this. This alloy does not have a very high corrosion resistance towards the cooling water and subsequently other forms or Zircaloy have been introduced, in which small additions of Fe, Cr and Ni significantly improve the properties (Table 34.7).

Table 34.7 *Typical chemical composition for LWR cladding alloys* (*in wt%*).

	Zircaloy-2	*Zircaloy*-4	*Zirlo*	*M*5	*E*110
Sn	1.20–1.70	1.20–1.70	0.9–1.2		
Nb			0.9–1.3	0.8–1.2	0.95–1.05
Fe	0.07–0.20	0.18–0.24	0.1	0.006–0.012	0.015–0.060
Cr	0.05–0.15	0.07–0.13	0.07–0.13		
Ni	0.03–0.08	0.007(Max)			
Zr	Balance	Balance	Balance	Balance	Balance

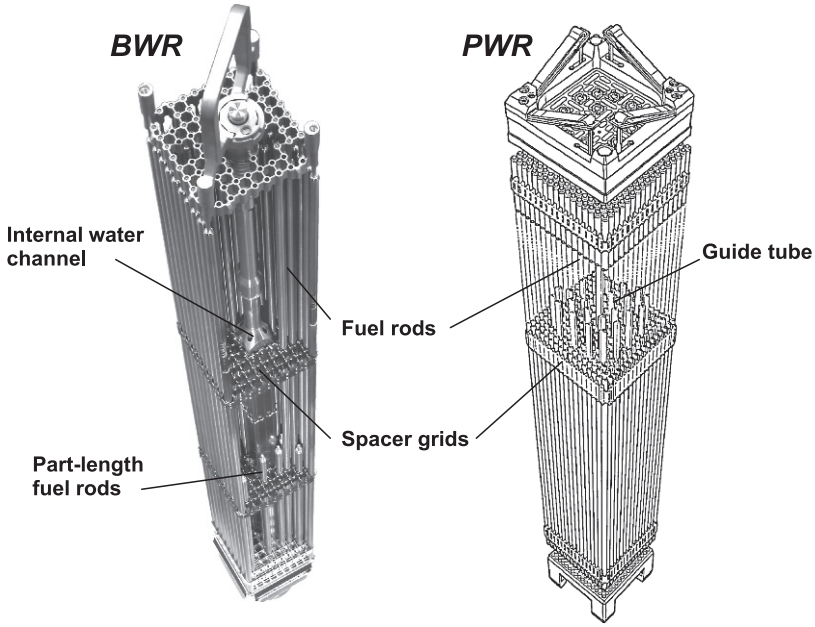

Fig. 34.34 *Fuel elements for BWR and PWR.* (*©AREVA, reproduced with permission*).

With the increasing target burnup of the fuel, the demands on the corrosion resistance have increased further and nowadays alloys of zirconium with niobium have been introduced (under the commercial names M5, Zirlo or E110).

(c) The fuel element

The core of a reactor consists of fuel elements (assemblies) that are composed of an array of fuel pins that are held together by several spacer grids. In pressurized water reactors (PWR) the fuel pins are arranged in 14 × 14 to 17 × 17 square geometry. The fuel element contains generally about 179–264 fuel pins and several control rods that are kept together by a top and a bottom nozzle with interspersed grids (Fig. 34.34).

For boiling water reactors (BWR) the fuel pins are generally assembled in bundles of 8×8 to 10×10 square geometry. The bundles are surrounded by a thin tube. In modern BWR fuel bundles, there are either 91, 92, or 96 fuel rods per assembly depending on the manufacturer. Each element also contains several flow channels.

34.5.4 In-reactor behavior of LWR oxide fuel

(a) The thermal profile of LWR fuel

The energy generated by fission is converted to heat inside the fuel pellet and must be transferred to the coolant to generate electricity. Since uranium dioxide is a poor heat conductor, the heat transfer is slow and a strong radial thermal gradient between the pellet center and pellet rim develops under steady state conditions. Knowledge of the radial temperature distribution in nuclear fuel during irradiation is essential for the successful prediction of fuel performance as the fuel operating temperature affects fission product migration, fission gas release, grain growth and swelling. Moreover, the thermal stresses that are associated with steep radial temperature gradients can cause plastic deformation of the fuel at the center or cracks.

The temperature difference ΔT in the fuel between radial position r and the pellet rim can be approximated by the formula:

$$\Delta T(r) = T(R) - T(r) = \frac{\chi}{4\pi\lambda R^2}(R^2 - r^2) \tag{34.40}$$

where χ is the linear heat rate (in W/cm), λ is the thermal conductivity (in $W{\cdot}cm^{-1}{\cdot}K^{-1}$) and R is the pellet radius (in cm). Because the thermal conductivity varies with temperature and burnup and thus along the pellet radius, and also the linear heat rate varies along the pellet radius, a multi-zone model is used in practice, dividing the pellet in n annular zones with each their specific linear heat rate and thermal conductivity.

Since the gap between pellet and cladding is initially filled with helium gas, which is a relatively poor conducting medium, the temperature gradient over the gap is significant (80–100 K over about 80 μm). In contrast the metallic cladding conducts the heat very well and the temperature gradient in the cladding is relatively small. A representative temperature profile in a PWR fuel pellet is shown in Fig. 34.35.

During irradiation the temperature profile of the fuel pellet will change for several reasons:

- The fuel will densify during the initial stages of the irradiation, leading to a slight improvement of the thermal conductivity and a slight effect of the gap width.
- The pellet will crack during the first rise to power due to the thermal stresses.

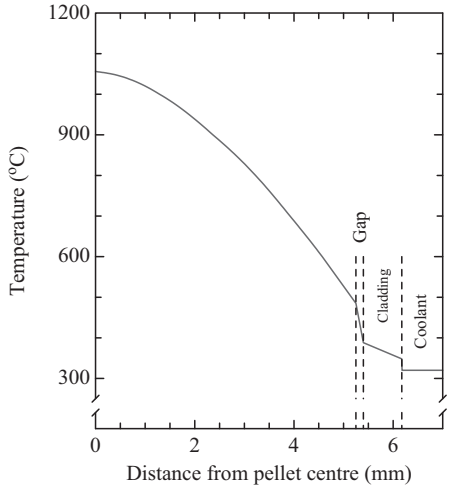

Fig. 34.35 *A typical temperature profile of a LWR fuel as a function of the fuel pin radius.*

- Owing to release of fission gases (Xe, Kr), which have a thermal conductivity significantly lower than helium, to the fuel pin free volume, the gap conductance will decrease.
- The fuel pellet will expand due to the accumulation of fission products in the lattice the formation of gas bubbles.
- The thermal conductivity of the fuel will steadily decrease as a result of accumulation of solid fission products in the lattice (increasing the phonon scattering) and in secondary phases, and the formation of gas bubbles.
- The radiation damage to the fluorite lattice (isolated defects, defect clusters and loops) will degrade the thermal conductivity.

Figures 34.36 and 34.37 show the mechanical changes the fuel pellet undergoes during irradiation. The fuel pellet shows several radial and axial cracks and the dish between the pellet closes due to the larger expansion in the pellet center, which shows a more plastic behavior at the higher operating temperature.

The temperature change has been studied extensively by in-pile central temperature measurements that reveal the integral of the above mentioned separate effects. The in-pile measurements show an increase of the temperature with burnup, suggesting a continuous thermal conductivity degradation (Wiesenack, 1997). This degradation has been studied directly by post-irradiation measurements of irradiated samples by several authors, as summarized in detail by Staicu (2010). The most extensive study was made by Ronchi *et al.* (2004b) who studied the thermal conductivity of UO_2 disks irradiated up to 92 MWd/kgHM and different in-pile temperatures. By systematic studies of the thermal conductivity of samples irradiated at different burnup and temperature using

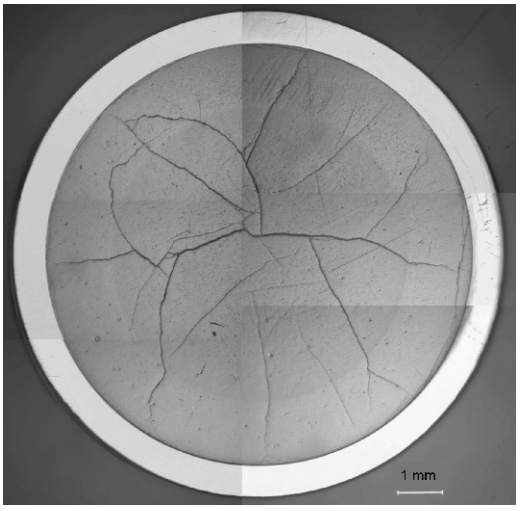

Fig. 34.36 *Macrograph of an irradiated UO_2 pellet showing the typical radial cracks.* (©*European Communities*, *reproduced with permission*).

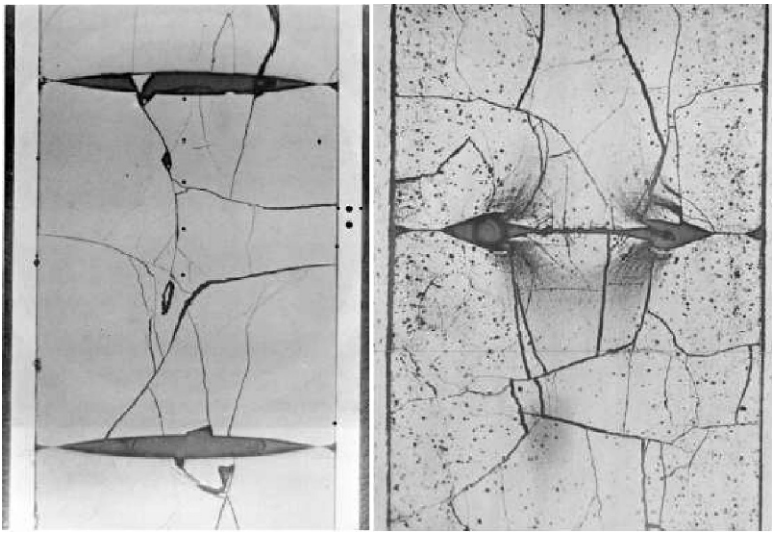

Fig. 34.37 *Macrograph of irradiated UO_2 showing the pellet at beginning of life before swelling* (*left*) *and after* (*gaseous*) *swelling* (*Billaux*, 2005).(©*Areva*, *reproduced with permission*).

thermal annealing cycles, these authors established the complex thermal conductivity dependence (Fig. 34.38). Most significantly, they observed that the degradation of the thermal diffusivity of the irradiated fuel samples was partially recovered during annealing and that the degree of recovery increased with the annealing temperature. In addition, they took into account that the degradation is not only caused during in-pile irradiation but also by the (α) radiation damage that occurred during storage.

Thus, Ronchi *et al.* (2004b) proposed a thermal conductivity expression that interpolates the results, taking into account the following effects:

1. Soluble, non-volatile fission products
2. Fission gas and Cs content and its state (also accounting for the effect of rim restructuring)
3. Irradiation defects (both present at end-of-life and created during subsequent storage by self-irradiation)
4. Precipitation of the fission gasses
5. Annihilation of irradiation defects for thermal recovery conditions

The thermal conductivity expression (for 95% density) is based on the classical phonon heat transport equation (34.8) with coefficients A and B depending

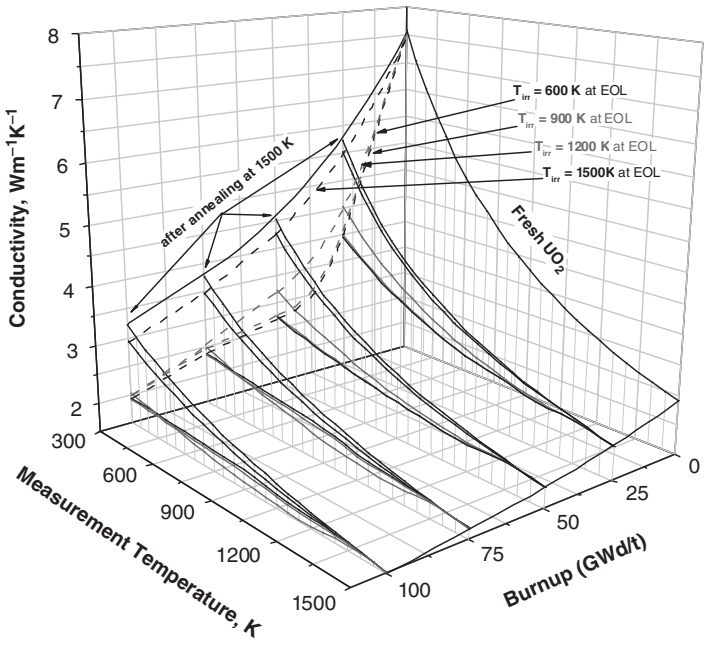

Fig. 34.38 *The thermal conductivity of irradiated UO_2 fuel* (*Ronchi et al.*, 2004b). (©*Elsevier* 2004, *reprinted with permission*).

on the irradiation temperature T_{irr} (700–1,450 K), the maximum temperature reached during annealing T_{ann} (700–1,450 K) following irradiation at T_{irr}, and the local burn-up *bu* (0–100 MWd/kgHM):

$$\lambda = \frac{1}{A(T_{irr}, T_{ann}, bu) + B(T_{irr}, T_{ann}, bu)T} \tag{34.41}$$

Here T is the instant application temperature (300–1,500 K), which for in-pile applications $T = T_{irr} = T_{ann}$. The set of relevant equations to use this expression is summarised in Table 34.8.

A different approach was used in the Halden project (Wiesenack, 1997), which based its recommended thermal conductivity of irradiated UO_2 fuel on an analysis of in-pile experimental data for the central fuel temperature. Such in-pile measurements are not affected by post-irradiation damage, but require the supplementary assessment of the linear power and the fuel-cladding gap conductance. The suggested correlation is based on a burnup correction to the MATPRO thermal conductivity data for pure UO_2 (Hagrman and Reymann, 1979) with a correction for burn-up effects:

$$\lambda = \frac{1}{0.1148 + 0.0035bu + 2.47510^{-4} \times (1 - 0.0033bu)(T/K) + 0.0132exp(0.00188(T/K))} \tag{34.42}$$

where *bu* is burnup in MWd/kgU. Only slight differences exist between the two models.

There is limited information on the thermal conductivity of irradiated MOX in the open literature. Cozzo *et al*. (2009) reported the results for homogeneous SBR MOX of 35 MWd/kgHM obtained from out of pile studies. The results agree well with those for irradiated UO_2 by Ronchi *et al*. (2004b) for the same burnup. This can be explained by the fact that the composition of UO_2 and low Pu content MOX fuel converge during irradiation, the UO_2 producing Pu and the MOX consuming Pu, both accumulating fission products and radiation damage in an homogeneous way.

(b) Mass transport in oxide fuel

The ceramic fuels (UO_2, MOX) used in the LWRs have high melting points and are operated at moderately high temperatures. The atomic transport processes are of great interest in view of predicting the fuel performance during irradiation, specifically creep, grain growth, and sintering. Various diffusion processes occur in the fluorite lattice of the fuel. Chemical diffusion, self-diffusion, thermal diffusion and radiation-enhanced diffusion occur in stoichiometric fuel (O/M = 2) but also potentially in areas deviating slightly from stoichiometry.

Table 34.8 *Dependencies of the parameters of equation* (34.41).

$A(T_{irr}, T_{ann}, bu)$/ $m{\cdot}W^{-1}{\cdot}K^{-1}$	$= 0.046 + \Gamma(bu, GIS) + \delta A$	a,b
$\Gamma(bu, GIS)$	$= 9.02 \times 10^{-4}\, bu\, GIS + 1.74 \times 10^{-3}\, bu + 7.51 \times 10^{-3}$	a
δA	$= \delta A_{Sel\,f}(T_m, bu) + \delta A_{EOL}(T_m, bu)$	c
δA_{EOL}/m·K·W^{-1}	$= \frac{bu}{850}\left[\left(1+\exp\left(\frac{T_m-950}{25}\right)\right)^{-1} + \left(1+\exp\left(\frac{T_m-1300}{35}\right)\right)^{-1} - 0.0525\right]$	
$\delta A_{sel\,f}(T_{ann}, bu)$/ m·K·W^{-1}	$= 0.02F(bu)$ for $T_{ann} < 900$ K	
	$= 0.02F(bu)\frac{1450 - T_{ann}}{1450 - 900}$ for $900 < T_{ann} < 1450$ K	
	$= 0$ for $T_{ann} > 1{,}450$ K	
$B(T_{irr}, T_{ann}, bu)$/ m·W^{-1}	$= B_0 + (B_1 - B_0) + \frac{6.5 \times 10^{-5} - \delta B}{6.5 \times 10^{-5}}$	
B_0/m·W^{-1}	$= 1.65 \times 10^{-6}\, bu + 2.55 \times 10^{-4} + 3.6 \times 10^{-5}\, IRIM$	d
B_1	$= 4.2 \times 10^{-7}\, bu + 2.75 \times 10^{-4}$	
δB	$= F(bu)\delta B_{EOL}(T_m, bu)$	
δB_{EOL}/m·W^{-1}	$= \frac{bu}{34}\left[\left(4.0 \times 10^{-5}\left(1+\exp\left(\frac{T_m-950}{25}\right)\right)^{-1} + 2.5 \times 10^{-5}\left(1+\exp\left(\frac{T_m-1300}{35}\right)\right)^{-1}\right]$	
$GIS(bu, T_{ann}, T_{irr})$	$= \frac{1 - 0.9\left[1+\exp\left(\frac{T_{irr}-950}{30}\right)\right]^{-1}\left[1+\exp\left(\frac{73-bu}{2}\right)\right]^{-1}}{\left[1+\exp\left(\frac{T_{irr}-1350}{200}\right)\right]\left[1+\exp\left(\frac{T_{ann}-1350}{200}\right)\right]}$	
$IRIM$	$= \left[1+\exp\left(\frac{T_{irr}-950}{30}\right)^{-1}\right] \times \left[1+\exp\left(\frac{73-bu}{2}\right)\right]^{-1}$	d
$F(bu)$	$= \left(1-\exp\left(\frac{20-bu}{6}\right)\right)^{-1} - 0.015267$	

[a] GIS is the fraction of gas in-solid defined as the ratio of the gas amount present in dynamical solution to the total produced inventory
[b] Γ is the total scattering coefficient
[c] $T_m = \max(T_{irr}, T_{ann})$
[d] *IRIM* is the correction associated with the HBS formation

The diffusion of the metal atoms in the oxide fuels as the slower diffusing species ($D_O/D_U > 10^7$ at 1,873 K) is rate controlling process for diffusive mass transport like creep (Matzke, 1982). The diffusion of the metal atoms as shown in Fig. 34.39 is totally athermal below 1,373 K and appears fully temperature dependent only above 1,573 K. The radiation-enhanced (athermal) diffusion is

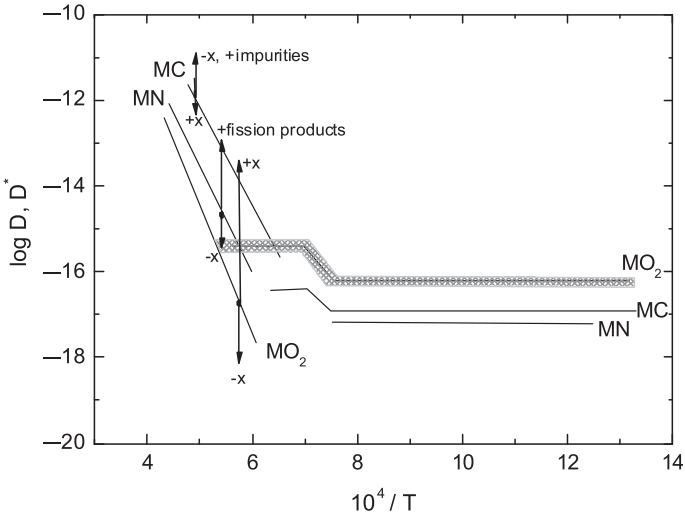

Fig. 34.39 *Radiation enhanced diffusion of uranium and or plutonium in nuclear oxides, carbides and nitrides (M = U and/or Pu). The arrows indicate how the thermally activated diffusion in MO_2 changes with deviation from stoichiometry, the accumulation of fission products and the presence of impurities.* (*After Matzke*, 1982).

also described in Section 34.5.4 (d) where values of the diffusion coefficient as a function of the fission rate are indicated.

Exhaustive reviews of the mass transport can be found elsewhere detailing the various mechanisms associated with the diffusion processes in UO_2 and mixed oxides $(U,Pu)O_2$ (Matzke, 1987, 1990). The self-diffusion of metal and oxygen atoms is strongly affected by the deviation from stoichiometric value. In the hyperstoichoimetric domain it is found that the diffusion of oxygen occurs via interstitials and strongly depends on the degree of deviation from the stoichiometric value. In the hypostoichiometric fuel the diffusion is associated with vacancy mobility. This is particularly true for high Pu-contents where the formation of Pu^{3+} is accompanied by vacancy formation for charge compensation.

The redistribution of oxygen in the fuel has an important impact on fuel-cladding interaction but also on transport properties. For hypostoichiometric oxide the solid-state thermal diffusion of oxygen vacancies occurs towards the high temperatures in the thermal gradient whereas it occurs in the opposite direction in hyperstoichiometric fuels (Sari and Schumacher, 1976).

At low and moderated temperatures creep in UO_2 or $(U,Pu)O_2$ results from the (slow) diffusion of the cations towards sinks like grain boundaries (Millet and Piconi, 1983). Although most of the single processes are well understood and quantified there is still some debate about the transport properties in fuel due to the complexity of the system studied i.e. local deviation from the

stoichiometric value, thermal-gradient, radiation effects, constant ingrowth of impurities (fission products) some being soluble, others not.

(c) The chemical form of the fission products

During irradiation fission products accumulate in the fuel up to several atom percent (Table 34.9). Many fission products have chemical properties different from uranium (valence state, oxygen affinity, ionic size) and (chemical) interaction with the bulk take place. The fission product lattice interactions, and particularly solubility, are strongly influenced by the defect chemistry of UO_2, i.e. oxygen vacancies and interstitials, as well as defect clusters (Fig. 34.40). Grimes and Catlow (1991) showed by atomistic calculations that the neutral trivacancy is the most favorable solution site for fission products in UO_{2-x}, while it is the uranium vacancy site for UO_{2+x}. In UO_2 both serve as solution sites depending on the fission product: the neutral trivacancy site for Xe and the uranium vacancy site for Cs and Rb.

When solubility is exceeded, macroscopic changes in the fuel microstructure will be observable, such as precipitation and/or reaction, as revealed by post-irradiation examinations. Such studies have shown that the fission products in irradiated LWR oxide fuel can be grouped in the following classes (Kleykamp, 1985):

- Elements that are soluble in the uranium dioxide crystal lattice, such as the rare earths, zirconium and niobium
- Inert gases (Xe and Kr) that have a very low solubility in the ceramic matrix and accumulate in gas bubbles

Table 34.9 *Typical fission product inventory of UO_2 fuel from a* 1,000 *MW(e) PWR after* 3 *years operation* (*in at.%*). (*After Bowsher*, 1987).

Element	*Concentration*	*Element*	*Concentration*
Se	0.01	Te	0.07
Br	5.43×10^{-3}	I	0.03
Kr	0.09	Xe	0.60
Rb	0.08	Cs	0.53
Sr	0.21	Ba	0.19
Y	0.11	La	0.18
Zr	0.76	Ce	0.39
Nb	0.01	Pr	0.15
Mo	0.64	Nd	0.48
Tc	0.17	Pm	0.05
Ru	0.41	Sm	0.07
Rh	0.11	Eu	8.83×10^{-3}
Pd	0.13	Gd	2.66×10^{-3}
Ag	2.74×10^{-3}		

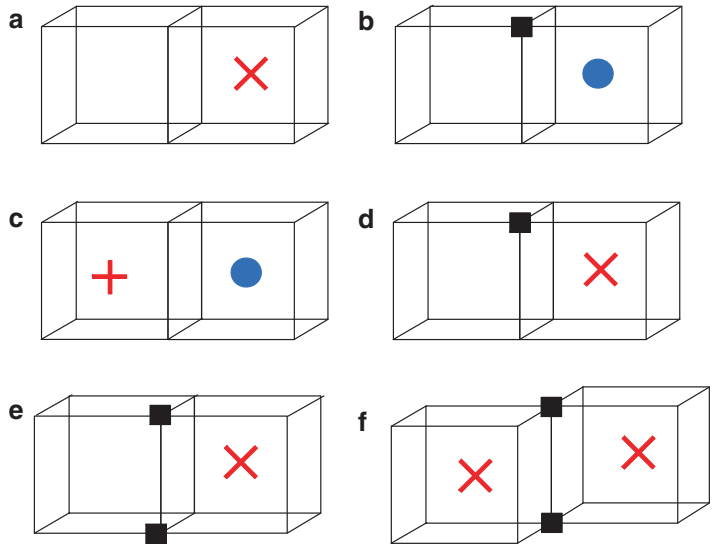

Fig. 34.40 *Solution sites for fission products in UO_2;* ■, *oxygen vacancy*, ●, *uranium ion*, × *uranium vacancy*, + *interstitial site.* (*a*) *Uranium vacancy*; (*b*) *oxygen vacancy*; (*c*) *interstitial site*; (*d*) *di-vacancy*; (*e*) *tri-vacancy*; (*f*) *tetra-vacancy*. (*After Grimes and Catlow*, 1991).

- Metallic precipitates that contain noble metals (Ru, Rh, Tc, Pd) as well as molybdenum
- Oxide precipitates such as the the so-called grey phase (Ba,Sr)(Zr,U,Pu)O_3 or caesium uranates
- Other secondary phases such as caesium iodide

The formation of secondary phases is dependent on the thermodynamic stability and on the kinetics of diffusion of the fission products in the fuel. The temperature of LWR oxide fuel is ~1,300 K at the center and ~750 K at the pellet rim, which means that solid state diffusion is low. The mobility of the fission products in the fuel is primarily caused by transport in lattice defects, pores and cracks. As a result the volatile fission products will react or condense somewhere between the center of the fuel and the gap between the fuel and the cladding. But below 1,000 K the rates of transport and reaction will be low. The non-volatile fission products will remain close to where they are formed.

Locally thermodynamic equilibrium can be obtained, which means that the most stable phases can form. The most favorable sites where reactions can take place are fission gas bubbles, the bubble-matrix interface, dislocation lines, grain boundaries or cracks (Cronenberg and Osetek, 1987), as is shown in Fig. 34.41. Based on thermodynamic considerations the formation of various fission product phases has been suggested (Besmann and Lindemer, 1978; Paquette *et al.*, 1985; Cordfunke and Konings, 1988). For example the volatile

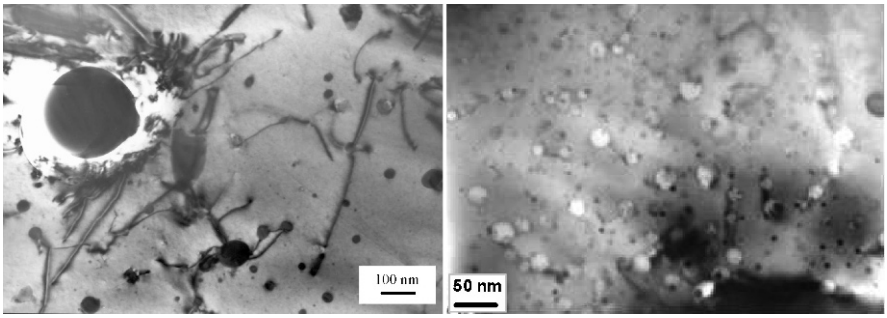

Fig. 34.41 *TEM micrographs of UO_2 fuel irradiated to high burnup showing dislocation loops and metallic fission product precipitates (dark spots) sometimes pinning dislocation lines (left, high fuel temperature) and associated with gas bubbles (right, low fuel temperature). (©European Communities, reproduced with permission).*

fission products cesium and iodine can react to form CsI, which has a substantially lower volatility. The formation of CsI has been suggested after the TMI-2 accident, to explain the unexpected low release of iodine. However, very little experimental evidence for the CsI formation has been presented. Johnson and Johnson (1988) made systematic studies on irradiated samples by mass spectrometry but failed to detect CsI. Hiernaut *et al.* (2008b) recently detected a small CsI signal in the mass spectrometric analysis of an oxidized irradiated UO_2 sample.

In addition to CsI, other potential phases for the volatile fission products have been suggested (Bowsher, 1987). Since the Cs/I ratio in the fuel is much larger than 1, thermodynamic calculations suggest that the excess Cs reacts with molybdenum to form Cs_2MoO_4, with tellurium to form Cs_2Te, with zirconium to form Cs_2ZrO_3, or with UO_2 to form Cs_2UO_4 or $Cs_2U_2O_7$. Similarly barium has been predicted to react with zirconium, uranium and other metals to form the complex (Ba,Sr,Cs)(Zr,U,Pu)O_3 phase with Ba >> (Sr + Cs), the so-called ''grey phase''. This phase has been identified by microprobe analysis in irradiated LWR fuels that have been subjected to higher than normal operating temperatures (Kleykamp, 1985; Kleykamp *et al.*, 1985). In contrast to barium, strontium has a high solubility in UO_2 and the major fraction of this element is incorporated in the fuel matrix (Kleykamp, 1985). The noble metals (Pd, Ru, Tc, Rh), which also have a very low solubility in the matrix, have been found to form metallic precipitates with Mo, often called ε-phase, (Kleykamp, 1985; Kleykamp *et al.*, 1985), in line with thermodynamic considerations (see Fig. 34.42). The size of the ε-phase particles varies as a function of local fuel temperature and thus on the radial position (Fig. 34.41), from a few nanometer in the outer zone of the fuel pellet up to a few micrometer in the center of a fuel pellet. Probably the coalescence is caused by the higher mobility of the small

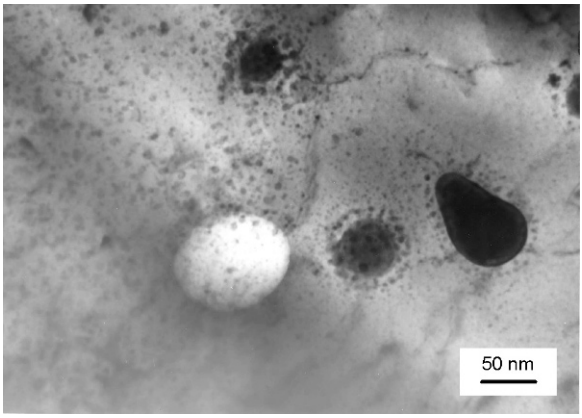

Fig. 34.42 *Oswald ripening of the ε-phase particles showing their coalescence into larger ones.* (©*European Communities*, *reproduced with permission*).

particles at sufficient high temperature and the energetic gain by minimizing the total surface energy (Oswald ripening), as shown in Fig. 34.42.

An important parameter governing the chemical state of the fission product is the oxygen potential. The fission process is in principle oxidizing because the average of the sum of the valence states of two fission products formed is lower than that of the uranium atom (4+) from which they originate and thus they do not bind the oxygen completely, but reality is more complex. Many authors have attempted to assess the O/M ratio or oxygen potential of irradiated nuclear fuel. Kleykamp (1979) estimated the O/M ratio at the end of irradiation to be close to 2.00 at the pellet center and <2.00 at the pellet rim, based on observations on the chemical state of the fission products, impurities and cladding. Oxygen potential measurements on irradiated fuel samples confirmed this. Matzke (1994, 1995) studied the oxygen potential of samples of various burnup, indicating that the oxygen potential slightly increases with burnup to reach the value of the Mo/MoO_2 couple, around 400 kJ/mol at T = 1,025 K. Walker *et al.* (2005) studied the oxygen potential as a function of the radial position in a very high burnup sample (102 MWd/kgHM), indicating the oxygen potential decreases from the center to the rim. However, the oxygen potential values measured in that study were substantially above the Mo/MoO_2 couple.

(d) Fission gas release

The gases produced during irradiation by fission or subsequent decay of fission products are primarily the noble gases xenon and krypton. Some helium is also produced by ternary fission, alpha-decaying actinides and (n, α) reaction on oxygen. The diffusion, precipitation, re-solution and release of these gases in

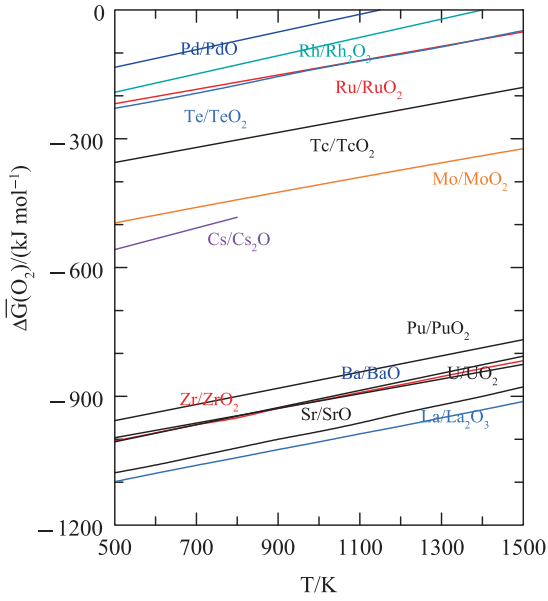

Fig. 34.43 *An Ellingham diagram for some key fission products.*

nuclear fuels are among the main phenomena that govern the irradiation performance in nuclear reactors.

LWR fuel is designed to have a low fission gas release during normal operation, the release normally being a few percent of the inventory. This low release implies that a significant amount of gas should be retained in the ceramic matrix. Owing to their low solubility, the gases precipitate in bubbles as observed by transmission electron microscopy (TEM). The consequence is the swelling of the fuel pellet, which contributes to the pellet–clad gap closure at the beginning of the irradiation and has a direct effect on the thermal gradient and at higher burnup on the pellet and cladding mechanical interaction (PCMI). The amount of gas released in the plenum has an impact on the internal pressure of the fuel rod, as well as on the heat transfer from the pellet to the cladding.

Fission gas release is a complex process that describes the path of the fission product from its position of creation to its escape to the free volume of the fuel pin. The following release stages can be distinguished (Fig. 34.44):

1. Atomic diffusion of the fission product in the lattice and along grain boundaries, thermally activated and enhanced by radiation
2. Capture in intragranular and intergranular bubbles, that might be fabrication pores or newly formed (nanosized) bubbles that often occur along fission tracks (Fig. 34.45)

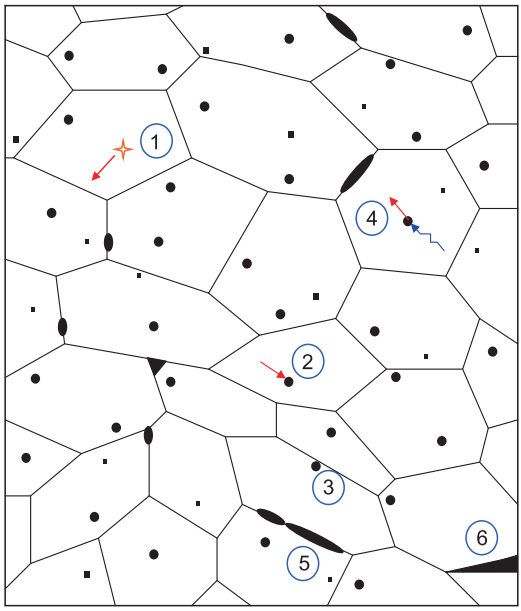

Fig. 34.44 *A schematic representation of the various steps in the fission gas release.*

3. Migration of bubbles to grain boundaries, induced by radiation and thermally assisted (at high temperatures)
4. Resolution (or re-injection) of gas from the bubbles into the matrix, induced by radiation
5. Coalescence of closed gas pores into pores along the grain boundaries
6. Venting via open porosity channels that are formed by porosity aggregation into an intergranular network or via cracks (Fig. 34.46)

The in-pile behavior of the rare gases can basically be divided in two regimes, one coupled to the temperature and temperature gradient resulting in thermal diffusion of the fission gases and an athermal process directly related to fission spikes in the fuel.

(*i*) *Thermal and athermal diffusion*

Values of the coefficient diffusion of Xe and Kr in UO_2 have been derived by Turnbull *et al*. (1982) for the temperature range 250–1,400°C, showing lattice diffusion in the higher temperature range and gas diffusion assisted by uranium-vacancy mobility between 700°C and 1,200°C.

In the central region of the LWR fuel the fission gases precipitate in form of intragranular bubbles but also at the grain boundaries in form of lenticular bubbles sometimes interconnected. In transient tested fuels bubble coalescence

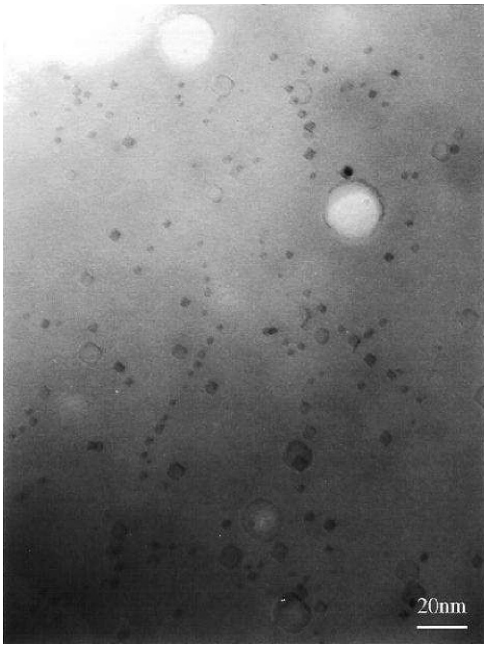

Fig. 34.45 *A TEM micrograph of an irradiated UO_2 fuel showing fission gas bubbles sometimes forming strings and eventually associated with ε particles.* (©*European Communities*, *reproduced with permission*).

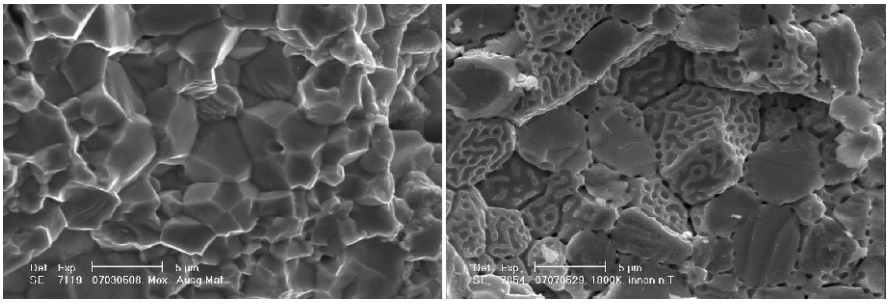

Fig. 34.46 *SEM images of irradiated LWR fuel*; (*left*) *the microstructure of a fracture surface after irradiation*, (*right*) *the fission gas channels formed at the grain boundaries after thermal treatment at* 1,800 *K.* (©*European Communities*, *reproduced with permission*).

occurs and bubbles surrounded by a cloud of smaller bubbles are observed by TEM (see the right micrograph of Fig. 34.41), as discussed by Ray and Matzke (1991).

In the colder region of the fuel there is almost no temperature activated diffusion of the insoluble fission gases. With increasing burnup, intragranular bubbles form in the fuel. Their size increases towards the center of the pellet. Fission spikes passing through bubbles can eject atoms from bubbles back to the lattice via some ballistic effects but more probably via a local increase of the temperature and the hydrostatic pressure inside the spike. Direct evidence of this phenomenon observed for irradiated fuel is the relation between the diffusion coefficient of those fission products (almost) immobile at the irradiation temperature and the fission rate. As the thermal component of a fission spike can be related to the thermal conductivity of the material, it is not surprising that radiation enhanced diffusion decreases with the increase of thermal conductivity (and therefore local temperature) within the sequence $UO_2 > UC > UN$ (Matzke, 1980).

Athermal fission-enhanced diffusion of U and Pu has been extensively described in the past (Matzke, 1983). The enhanced diffusion coefficient D^* is temperature-independent between ambient temperature and about 1,000°C (depending on fission rate). It is also independent of total neutron flux, but it is directly proportional to the fission rate, F (in fission $cm^{-3}{\cdot}s^{-1}$)

$$D^* = AF \tag{34.43}$$

with $A = 1.2 \times 10^{-29}$ cm^5, yielding, for example, $D^* = 9 \times 10^{-17}$ $cm^2{\cdot}s^{-1}$ for $F = 7.5 \times 10^{12}$ $cm^{-3}{\cdot}s^{-1}$.

As a direct consequence of fission spikes in-pile creep should also be accounted for (Brucklacher and Dienst, 1972), yielding also a very significant enhancement below about 1,000°C, explained by the thermal spike effects of fission, with $D^* \sim 1.5 \times 10^{-17}$ $cm^2{\cdot}s^{-1}$.

In-pile release of fission gases is known to be due to a number of mechanisms besides thermally activated diffusion, including direct emission of fission products (often called recoil), release by knock-out due to interaction of gas atoms with passing fission fragments or sputtering of the fuel, and by fission-enhanced diffusion (Turnbull *et al*., 1982). Most of the published information on diffusion of fission gases is based on release measurements assuming that diffusion kinetics operate in the bulk specimen (e.g. Matzke, 1980).

(*ii*) *Fission gas release from UO_2*

As discussed above, the fission gas release predominantly takes place via venting of open porosity channels that are formed by bubble coalescence or cracking. Whereas cracking takes place already at early stages of the irradiation, the porosity coalescence is strongly burnup and temperature dependent. As demonstrated in in-pile and out-of-pile experiments, the bubble coalescence takes place at lower temperatures when the burnup increases. This is reflected in the so-called Halden threshold (Fig. 34.47), which is the relation between the fuel centerline temperature and burnup for a (arbitrary) 1% fission gas release, based on the in-

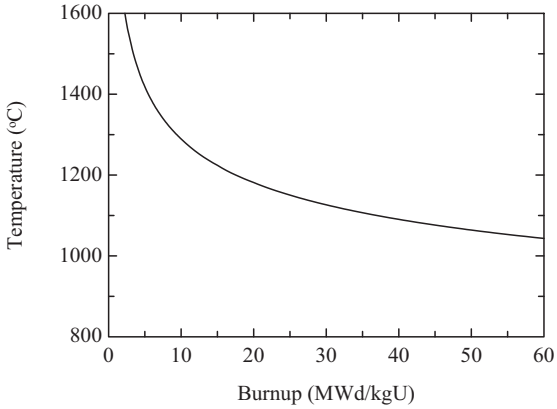

Fig. 34.47 *The Halden threshold for fission gas release as a function of pellet average burnup indicating the temperature for which more than* 1% *of the pellet average fission gas is released.*

pile experiments performed in the Halden test reactor (Norway). The Halden threshold is given by the equation (Vitanza *et al*., 1979):

$$T_c(^\circ C) = \frac{9800}{\ln\left(\frac{bu}{0.005}\right)} \tag{34.44}$$

where T_c represents the central temperature in degrees Celsius, and *bu* the burnup in $MWd/kgUO_2$.

Similar observations have been made by out-of-pile mass spectrometry analysis of irradiated fuel samples during heating. Hiernaut *et al*. performed systematic studies of the release of fission products from irradiated fuel samples of different burnup, in normal state and oxidized (Hiernaut and Ronchi, 2001; Hiernaut *et al*., 2008a, b). They observed three distinct release stages as a function of the annealing temperature:

1. The low temperature release of the gas that had migrated to the grain boundaries during the irradiation
2. The release of fission gas via atomic diffusion to the grain boundaries
3. Release of fission gas trapped in almost immobile intragranular gas bubbles assisted by the progressive sublimation of the sample

(*iii*) *Fission gas release from MOX*

MOX fuels generally show more pronounced fission gas release, which is attributed to the fact that they are operated at higher power in the course of the irradiation and therefore at higher temperature. The fuel microstructure, however, also seems to play a role. For example it has been suggested that the plutonium-rich agglomerates in MOX fuel develop the high burnup structure

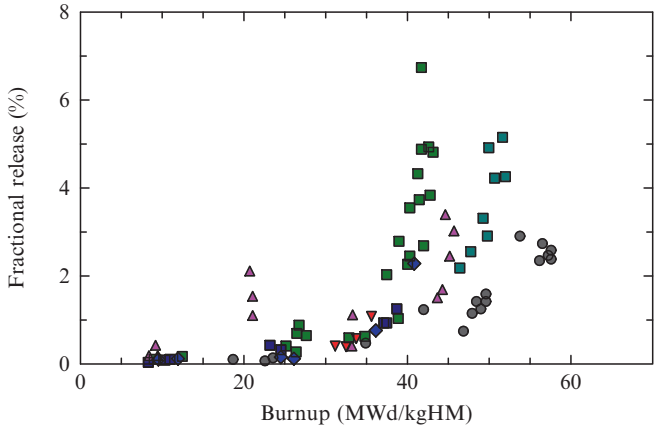

Fig. 34.48 *Measured fractional fission gas releases from* MIMAS (□, *where the different colors represent various types of AUC and ADU starting material*), *COCA* (◊), *OCOM* (▲) *and SBR* (▽) *mixed oxide rods, as well as IDR* UO_2 (●) *rods.* (*After Fisher et al.* 2002).

(HBS) and hardly retain the fission gas. This is corroborated by the post-irradiation examinations of homogeneous SBR MOX. Fisher *et al.* (2002) demonstrated that indeed SBR MOX has a lower fission gas release above about 45 MWd/kgU than heterogeneous MOX (Fig. 34.48). However, this is not consistent with the current view that the fission gas release from the HBS is low. Other effects, such as grain size, which is generally lower in MOX, or differences in the initial porosity structure (open vs closed) could also play a role, as larger grains and porosity slow down the fission gas release.

(e) The high burnup structure

(*i*) *Characteristics*

In the late 1950s it was observed that a strong capture by ^{238}U of neutrons in the resonance range occurs at the periphery of the nuclear fuel leading to the production of ^{239}Np and therefore of ^{239}Pu (Klein *et al.*, 1958). The consequence of the increase of the fissile density is a local increase of the burnup. Electron probe microanalysis (EPMA) has shown that the Pu content increases by a factor 2–3 (Fig. 34.49). Secondary ion mass spectroscopy (SIMS) has demonstrated that this increase is found for all Pu isotopes (^{239}Pu, ^{240}Pu, ^{241}Pu, ^{242}Pu) as well as americium (^{243}Am) (Desgranges *et al.*, 2009). Typically the area concerned by this phenomenon is the annular outer part of the fuel pellet of about 200 μm thickness, representing about 8% of the fuel volume at a (radially averaged) burnup of 60 MWd/kgU. The local enrichment then decreases almost exponentially towards the center of the fuel, as shown in Fig. 34.49 by the concentration of the fission product Nd, an excellent burnup indicator because

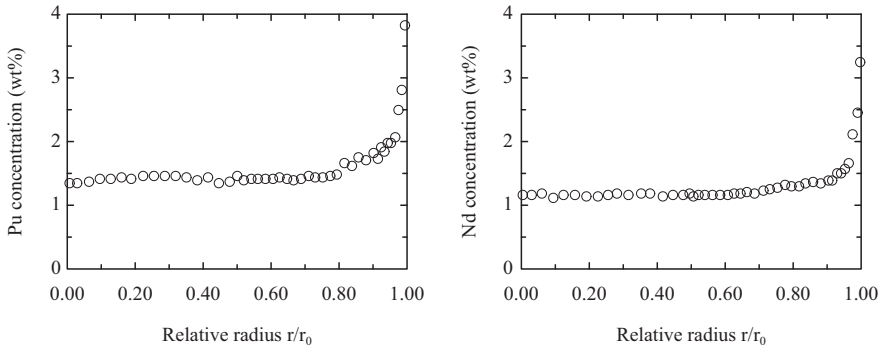

Fig. 34.49 *The Pu and Nd concentration profiles for irradiated UO_2 of* 97.8 *MWd/kgU pellet average burnup measured by EPMA.* (*After Manzel and Walker*, 2002).

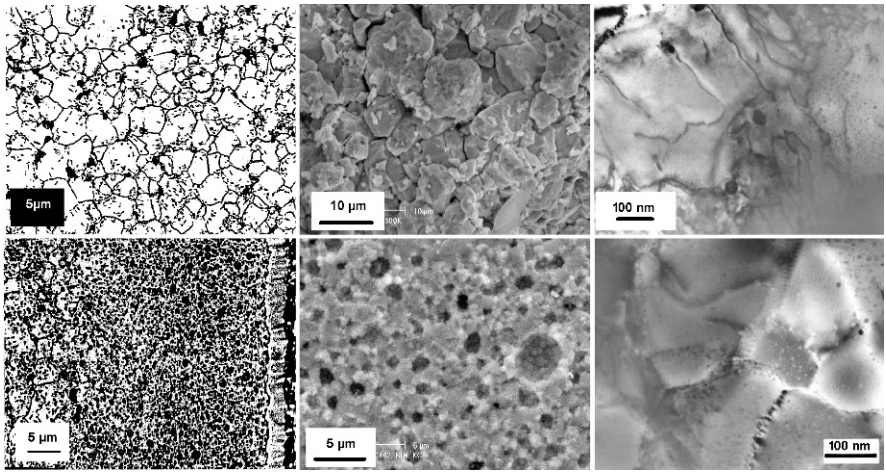

Fig. 34.50 *Optical ceramography, scanning electron micrograph and transmission electron micrographs* (*left to right respectively*) *of un-restructured* (*upper row*) *and re-structured irradiated UO_2 fuel referred to as HBS* (*lower row*). (*©European Communities, reproduced with permission*).

it is immobilized by dissolving in the fuel matrix and because is produced at the same yield both for ^{235}U and ^{239}Pu fission.

At an average fuel burnup of 45 MWd/kgU this increase of local burnup at the pellet periphery results in a modification of the fuel microstructure (Figs. 34.50 and 34.51). The original grains with size of around 10 µm in typical LWR fuels tend to subdivide into thousands of smaller grains with sizes of about 100–200 nm. This restructuring of the grains is associated with the

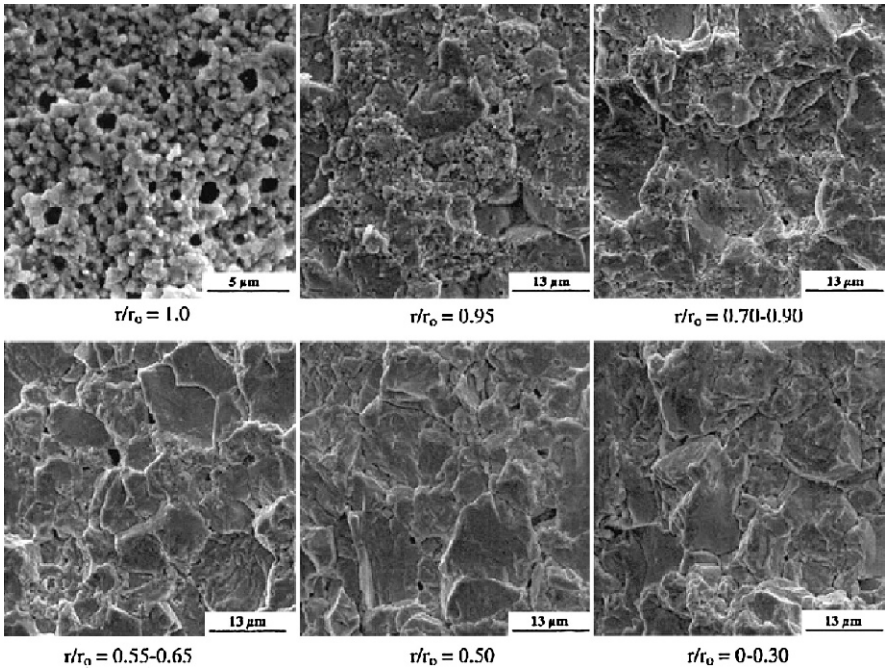

Fig. 34.51 *Scanning electron micrographs of a nuclear reactor fuel of rod average burn-up of* 97.8 *MWd/kgHM at several radial positions* (*Manzel and Walker*, 2002). (©*Elsevier*, 2002, *reprinted with permission*).

formation of a local porosity that can reach values above 20%. The coarsened micrometric size porosity contains almost all of the fission gases. For power reactors this phenomenon has been observed in the 1980s. Two structures, rounded grains at open surfaces and (bulk) polyhedral grains, have been identified in the high-burnup region of the fuel (Lozano *et al*., 1998). The formation of smaller grains at open surfaces (e.g. pores) shows a fractal appearance with the smaller grains having a size of less than 10 nm (Fig. 34.52). The surface reorganization has been observed by scanning electron microscopy (Matzke *et al*., 1989; Une *et al*., 1992) and is accompanied by a bulk restructuring that is also observable by scanning electron microscopy but is mostly investigated by transmission electron microscopy (Une *et al*., 2001). The fuel transforms by a sub-division process in polyhedral grains surrounding pores. The newly formed tiny grains are often found to be slightly disoriented (a few degrees) (Ray *et al*., 1997). A recent observation of a memory effect of the original grains structure supports this assumption (Hiernaut *et al*., 2008a).

Originally observed at the periphery of UO_2 fuels, this high burnup structure (HBS) has also been found in the plutonium-rich agglomerates of Mimas MOX fuels at rather medium pellet-average burnups (Fig. 34.53). For that reason it is

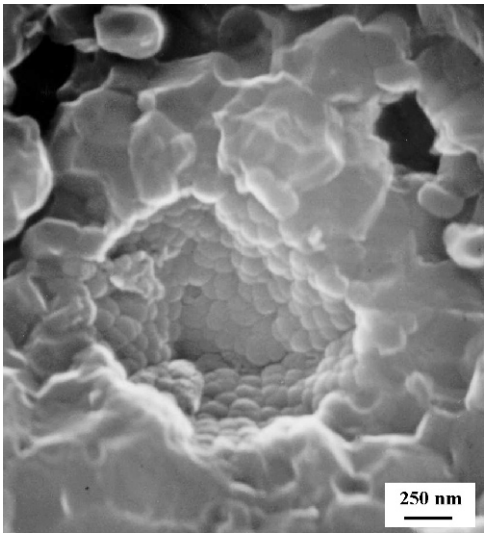

Fig. 34.52 *The grain subdivision as observed in a pore in the HBS zone of a UO_2 fuel.* (©*European Communities*, *reproduced with permission*).

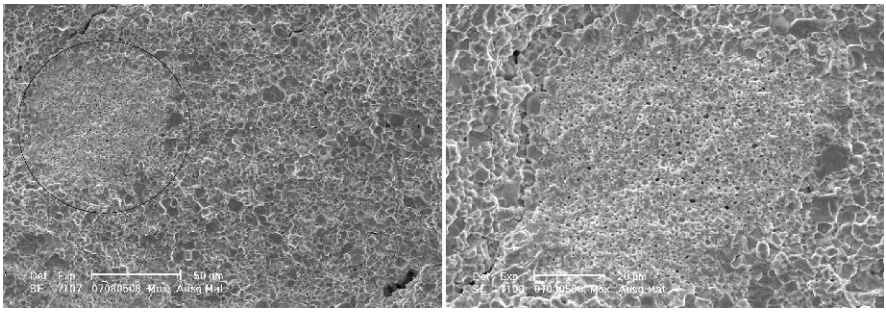

Fig. 34.53 *A Pu-rich agglomerate in irradiated MOX sample*; *the right picture is a higher magnification of the circled area.* (©*European Communities*, *reproduced with permission*).

preferentially referred to as HBS rather than "rim structure" although, when appropriate, this latter term is also used given the spatial information it reflects.

The formation of the HBS could lead to a slight increase in the oxygen potential starting at a local burnup of 80 MWd/kgU (Spino and Peerani, 2008). It could therefore be expected that the release of the fission gases could be enhanced. However, as previously reported (Kleykamp, 1979; Matzke, 1995; Walker *et al*., 2005) the LWR fuel remains stoichiometric or slightly hypostoichiometric. It was also thought that the HBS porosity would induce an enhanced mobility of the fission gases during normal conditions and that

there was a new source for fission gas release occurring directly from the restructuring at high burn-up.

Mogensen *et al*. (1999) determined the radial xenon concentration profiles by X-ray fluorescence (XRF) and EPMA of commercial low-enriched BWR fuel with burn-ups of 44.8–54.9 MWd/kgU and high-enriched PWR fuel with burn-ups from 62.5 to 83.1 MWd/kgU. They found that the percentage of gas released from the UO_2 grains in the outer region of the fuel was generally small compared with the percentage released from the pellet cross-section. This is consistent with the current understanding that most of the fission gas released from the fuel when the high burn-up structure forms is retained in the new pore structure. This has been also confirmed by Spino (Spino *et al*., 2004, 2005; Spino and Papaioannou, 2008), who showed that at least up to 250 MWd/kgHM local burn-up and 25% local porosity no relevant interconnecting paths between pores were present in the HBS (Fig. 34.54), as well as by Knudsen cell fission product release measurements by Hiernaut *et al*. (2008a).

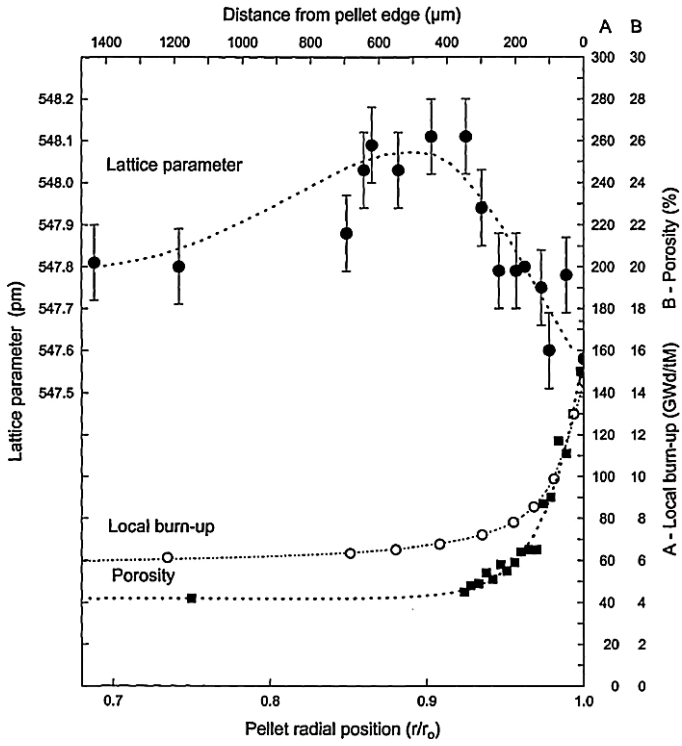

Fig. 34.54 *Radial lattice parameter, local burn-up and porosity profiles of a standard LWR fuel with 67 MWd/kgHM average burn-up* (*Spino and Peerani*, 2008). (©*Elsevier*, 2008, *reprinted with permission*).

Whereas the XRF and EPMA analyses give an indication of the xenon concentration in the bulk, which decreases in the HBS due to the recrystallization, SIMS measurements also detect the xenon in gas bubbles. With this technique Noirot *et al.* (2008) showed that the xenon concentration in fuel of burnup of 62 MWd/kgHM indeed increases in the HBS, and that it approximately corresponds to that expected for that burnup.

It can thus be concluded that the available experimental data indicate that there is no appreciable loss of fission gas from the pellet rim to the gap and that the majority of the gas is located within the pores, which are surrounded by a depleted matrix (with a constant xenon concentration of around 0.25 wt%). The large amount of the gas released comes from the inner part of the fuel. Indeed, in the rim zone, there is a little, but non-negligible, decrease of the thermal conductivity due to the increased porosity. Thus, the central temperature may increase, leading to enhanced thermally activated release from the inner part of the fuel pellet (see next section).

As discussed in Section 34.5.4 (a), Ronchi *et al.* (2004a) found that the thermal diffusivity decreases with increasing burn-up. The largest decrease was observed in a fuel disc that had been irradiated to a burn-up of 92 MWd/kgU at a low temperature of 450°C. Walker *et al.* (2006) studied the thermal conductivity of a commercial PWR fuel with an average section burn-up of 102 MWd/kgHM. In spite of the formation of the high burnup structure, the thermal diffusivity of the fuel at 100 MWd/kgHM was 55% higher than the value expected to result from the degradation caused by the build-up of fission products and point defects in the fuel lattice at this burn-up. Clearly, the higher thermal diffusivity and conductivity caused by the HBS formation is a consequence of the removal of fission product atoms from the fuel lattice and healing of radiation defects that accompanies restructuring of the fuel grains (part of the HBS formation mechanisms). Moreover, the role of the pores of the high burnup structure as sinks for the fission gas expelled from the fuel lattice during restructuring is more important than the counter acting effect as barriers to heat transport.

The radial variation of the Vickers hardness H_V and the fracture toughness KI_c in high burnup LWR UO_2 fuel indicate that the fuel becomes a factor of two softer in the course of the irradiation as found by Spino and co-workers (Spino *et al.*, 1996, 2003). The first softening process is detected at the fuel periphery when the local burn-up exceeds 70 MWd/kgHM, essentially as a result of the porosity build-up after HBS formation. The second softening process is found to affect uniformly the whole fuel after it reaches an average 70 MWd/kgHM, as a result of a mechanism that ostensibly denotes the bulk healing of the accumulated irradiation defects (Spino *et al.*, 2003) and that corresponds to the onset of the HBS formation. The other interesting result is the characterization of the fuel hardness versus porosity dependence, from which it can be derived that through the formation of the HBS, the most stable pore configuration in the fuel is achieved.

(*ii*) *Formation mechanism*

The exact mechanisms responsible for the formation of the high burnup structure are still under investigation. The formation of defects in combination with the presence of the fission gases appears to play a key role in the process and several scenarios have been suggested.

Nogita and Une (1994, 1995) proposed a formation mechanism for the HBS that is directly related to the accumulation of radiation damage. Tangled dislocation networks are formed by the inhomogeneous accumulation of dislocations after the development of interstitial-type dislocation loops. At the same time, intragranular fission products gas bubbles are formed by the clustering of vacancies and of fission gases Xe and Kr. With increasing burn-up, tangled dislocations are organized into sub-divided grains with high angle boundaries (Nogita and Une, 1994). Then, some of them are recrystallized, sweeping out small intragranular bubbles. In this approach, recrystallization refers to a series of steps, i.e. formation of subgrains, growth of the subgrains into recrystallization nuclei, and growth of the recrystallized grains. In line with this, Spino *et al.* (1996) have tentatively attributed the formation of the HBS to the local start of recrystallization around pores (characteristic of the HBS).

This interpretation has been opposed by the results of the High Burnup Rim Project (HBRP) in which a set of irradiated UO_2 disks of different burnup and temperature were analyzed extensively (Kinoshita *et al.*, 2004). On the basis of the results of this project Matzke (1999) concluded that (a) there is no instantaneous recrystallization due to the accumulation of gas and radiation damage, (b) an increased temperature is needed for recrystallization, and (c) if occurring, recrystallization does not necessarily sweep gases. The latter three facts disagree with the formation mechanisms proposed by Nogita and Une.

TEM observations of HBRP samples (Sonoda *et al.*, 2002) showed that in the HBS the initial grains are polygonized (a dividing process to produce small grains with low angle boundaries with the neighboring grains, both large and small) and not recrystallized. The subdivision process proceeds further with increasing burnup as recently observed by the SEM examination of a very high burnup specimen (Hiernaut *et al.*, 2008a). Sonoda *et al.* (2002) thus concluded that the restructuring is initiated by the accumulation and mutual interaction of (1) radiation damage including point defects and dislocations, (2) fission products including gas bubbles and metal particles, (3) stored energy caused by electronic excitation and nuclear collision which may cause radiation-enhanced diffusion of interstitials and vacancies, and (4) the growth of dislocation loops.

In spite of the different views on its formation mechanism, there is now agreement that the HBS has a high fission gas retention capacity. In particular, the HBS does not evolve toward an open system of interconnected channels, even when porosity reaches very high values (e.g. 35% in a FBR fuel, 50% in a PWR MOX agglomerate) (Noirot *et al.*, 2008). As a technological spin-off of this result, the HBS could be considered to effectively retain the fission gases

occluded in pores up to relatively high local burn-ups (>300 MWd/kgHM) because only at these burn-up values porosity fractions greater than 0.3 may be reached, for which incipient pore interconnection might just appear. A consequence of the influence of HBS on thermal conductivity is that the high burn-up fuel will run cooler in the reactor than would be assumed from its thermal conductivity versus porosity behavior at low burn-up, leading to lower fission gas release.

(f) Pellet-cladding interaction

During irradiation the pellet starts to expand due to the following reasons:

- Thermal expansion of the UO_2 crystal lattice
- Radiation damage in the lattice, creating atomic displacements
- Expansion of the lattice due to the incorporation of impurities (fission products)
- The accumulation of fission gas in pressurized pores in the fuel matrix
- Relocation of cracked pellet fragments

As a result of this expansion, the gap between the pellet and the cladding will close during the course of the irradiation, strongly enhanced by the simultaneous creep down of the cladding in PWRs, and the pellet will eventually come into contact with the cladding. The pellet expansion will not be homogeneous along the length of the pellet, but will be largest at the pellet ends, leading to a hour-glass type deformation. Moreover, the pellet will undergo radial cracking due to differential thermal expansion which is higher in the center of the pellet where the temperature is higher as well, and decreases towards the ends. A schematic representation of the deformation of an irradiated pellet is shown in Fig. 34.55.

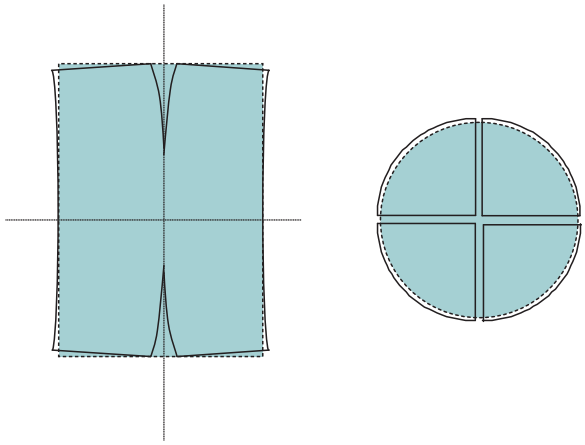

Fig. 34.55 *Schematic representation of pellet deformation during irradiation. The dotted lines indicate the as-fabricated pellet, the solid lines the fragmented pellet after irradiation.*

When the pellet fragments make contact with the cladding, generally at the beginning of the second annual irradiation cycle, the forces remain initially low. Because simultaneously the cladding creeps down as a result of irradiation exposure, the pellet will be compressed, eventually closing some of the radial cracks that were formed. When the pellet continues to expand due to the accumulation of the fission products, the pellet will exert a tangential stress on the cladding, which is not constant but which is high at the spots where the corners of the pellet press on the cladding. This leads to increase of the radial and hoop stresses in the cladding, which can cause deformation at interpellet ridges and eventually cracking of the cladding, particularly during transients. This process is called pellet–cladding mechanical interaction (PCMI).

In addition corrosion by some volatile fission products can occur, especially during power ramps. The fission product iodine has been suggested to play a role in this so-called stress corrosion cracking (SCC) phenomenon, the mechanism being (van Arkel) vapour transport of Zr as ZrI_4 vapour, out of cracks in the zirconia scale which occur due to the strain (Sidky, 1998). But also the role of other fission products (e.g. Cd) has to be considered.

(g) Fuel–coolant interaction

Failure of a fuel pin has a probability of between 10^{-4} and 10^{-6} per year. It can be caused by a design fault in the cladding, by fretting of debris that is caught at the spacer grids, by pellet–cladding mechanical interaction, or stress corrosion cracking. Operational experience during the last 10 years has reduced the failure probability significantly, and rod to grid fretting is now the main cause for failure.

In case of the failure or a defect of the cladding of the fuel pin, the water or steam of the coolant will come in contact with the fuel, leading to oxidation of the fuel pellet:

$$UO_2(cr) + xH_2O(g) = UO_{2+x}(cr) + xH_2(g) \tag{34.45}$$

As discussed by Higgs *et al*. (2007), the oxidation of defective fuel is a complex process involving gas-phase transport of steam as well as hydrogen to the fuel cracks, hydrogen uptake by the cladding, and solid state oxygen diffusion in the matrix along the temperature gradient.

Hiernaut *et al*. (2008b) have demonstrated that oxidation of the fuel matrix will affect the release of the fission products from the fuel pellet (Fig. 34.56). The release of Cs, I, Te, Ba, and Sr from irradiated fuel occurs 500–1,000 K lower in oxidized fuel. The experiments also demonstrated that the fission products Mo and Tc are significantly more volatile in oxidized fuel, as they form volatile gaseous oxide species such as MoO_3.

In the event of a pin failure a hydrogen/steam mixture will replace the helium fill gas in the gap and the (H_2/H_2O) partial pressure ratio will determine the oxygen potential and thus the chemical equilibria affecting fission product

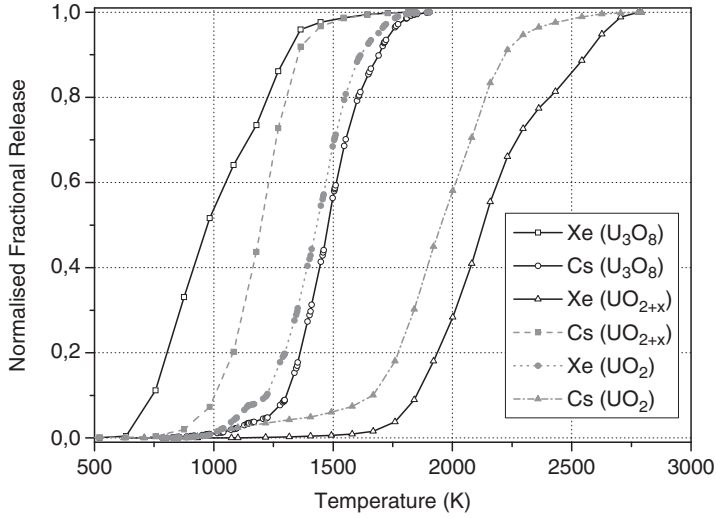

Fig. 34.56 *Fission gas release of Cs and Xe from an irradiated UO_2 sample* (*about* 70 *MWd/kgHM*), *and the same material oxidized to UO_{2+x} and U_3O_8.*

release. A compound such as CsI, which is suggested to be formed in nuclear fuel, is not stable in such an environment and the reaction

$$CsI(g) + H_2O(g) = CsOH(g) + HI(g) \tag{34.46}$$

is likely to occur, depending on the (H_2/H_2O) ratio. Like CsI, CsOH is soluble in water and will thus be retained in the cooling water of the reactor. Such leaks are generally detected by increase in the primary coolant activity.

When the pin failure is caused by a malfunctioning of the reactor the situation becomes more complex. In case of a loss-of-coolant accident (LOCA) the temperature in the fuel pin will rise rapidly and after failure the fission products will be released into the primary circuit where they are exposed to hydrogen-rich steam that additionally can contain elements from absorber and structural materials as vapor species or aerosols (Bowsher, 1987). For example the presence of boron, a commonly used neutron absorber, can lead to vapor–vapor or vapor–aerosol reactions that can convert CsI or CsOH into $CsBO_2$. Similarly, gaseous HI can react with or absorb on metal surfaces of the primary system. A comprehensive review of the fission product chemistry during accident conditions has been made by Bowsher (1987), and more details can be found in that work.

34.5.5 The FR oxide fuel pin and fuel element

Since the mid 1960s, mixed uranium–plutonium dioxide has been the primary fuel form for many fast reactor designs. The fast reactor fuel concept is, similar to the LWR fuel, based on the pellet-in-cladding, helium-bonded concept. For

fast reactors the pellets are clad in stainless steel tubes, which have wire wrapping or gridded support to provide channels for coolant flow. Fast reactor fuel pins are assembled in hexagonal geometry. Since a standard fast reactor fuel pin and fuel element design does not exist, various ways of assembling the fuel pins into a fuel element have been proposed. For example the spacing between the pins can be obtained by a grid, as in the LWRs, or by a wire that is helically wound around the pin. The assembly of pins is surrounded by a wrapper tube to control the cooling of the assembly.

The choice for stainless steel cladding material is motivated by the fact that material should be compatible with liquid metals (sodium), should operate up to 600–650°C, and must have a high radiation stability in a fast neutron flux, in which the displacement damage ranges from 50 to about 150 dpa. At these damage levels clustering of vacancies takes place, which in combination with the presence of helium from (n, α) reactions in the alloy components can lead to bubble and void formation, causing unwanted swelling. In the past the austenitic steels such as AISI 304 and 316 SS have been employed, but these steels have limited applicability because of unacceptable void swelling. Metallurgical improvements of the structure and composition have resulted in advanced austenitic steels such as D9 and 15-15Ti, which can withstand neutron displacement damage of up to 140 dpa (Kasiviswanathan *et al.*, 2007). Nowadays also Cr-ferritic-martensitic steel, alloys with high nickel content or oxide dispersion strengthened (ODS) steels are being studied for reaching exposure to even higher neutron displacement damage. Typical compositions of fast reactor cladding materials are summarized in Table 34.10.

Table 34.10 *Typical chemical compositions for some fast reactor cladding alloys* (*in wt%*). (*After Kittel et al.*, 1993; *Kasiviswanathan et al.*, 2007).

	316SS Austenitic	316Ti Austenitic	PFBR D9 Austenitic	15-15 Ti Austenitic	PE16 Ni-based	HT9 Martensitic	T91 Martensitic
Cr	17.0–18.0	17.1	13.5–14.5	14.7	16.5	11.8	8.3
Ni	13.0–14.0	14.1	14.5–15.5	14.7	43.4	0.55	0.1
Mo	2.0–3.0	2.75	2.0–2.5	1.15	3.15	1.00	1.0
Mn	1.0–2.0	1.50	1.65–2.35	1.6	0.01	0.55	0.4
Nb	0.05–1.0		0.05				0.08
W						0.50	
V						0.30	0.2
Si	0.5–0.75	0.49	0.5–0.75	0.43	0.01	0.25	0.4
Ti		0.34	[a]	0.43	1.27		
Al					1.2		
Co	0.05		0.05				
C	0.04–0.06		0.035–0.05	0.096	0.08	0.20	0.1
P	0.04	0.015	0.02	0.007			
S	0.01		0.01				
N	0.01		0.05				
Fe	Balance	Balance	Balance	Balance	Balance	Balance	Balance

[a] 5–7.5 × C

34.5.6 In-reactor behavior of fast reactor oxide fuel

(a) The thermal profile of FR fuel

Owing to the significantly higher linear heat rating in fast spectrum reactor cores (>400 W/cm) the central temperature of a fast reactor oxide fuel will be considerably higher than in thermal spectrum reactors and eventually a central void can form. In this case equation (34.40) must be reformulated:

$$\Delta T(r) = T(R) - T(r) = \frac{\chi}{4\pi\,\lambda(R^2 - R_0^2)}\left(R^2 - r^2 + R_0^2 \ln\frac{r^2}{R^2}\right) \qquad (34.47)$$

where R_0 is the radius of the central void. Like equation (34.40), this equation can best be solved by a multi-zone model as thermal conductivity varies with temperature and burnup, as in LWR fuel, but also as a function of pellet radius, as a result of the fuel restructuring and actinide and oxygen redistribution (see below). Typical central fuel temperatures are around 2,200–2,300 K during the first phase of irradiation, when the pellet–cladding gap is still open and before fuel restructuring has taken place. At higher burnup, after fuel restructuring and gap closure, the central fuel temperature decreases by several hundreds of degrees, as does the pellet surface temperature (Fig. 34.57). At the end of life of the fuel, the larger swelling of the cladding compared to the fuel can lead to a re-opening of a fuel-to-clad joint, in literature often called the JOG (Joint Oxyde-Gain, the French description) as discussed by Tourasse *et al.* (1992).

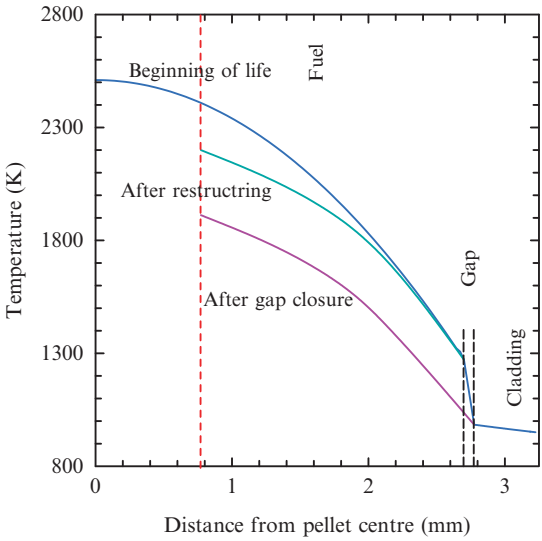

Fig. 34.57 *A typical temperature profile of a FR fuel as a function of the pin radius.*

The fuel-to-clad joint formation will have an impact on the thermal profile of the fuel, but little is known about the mechanism and evolution of its formation (Inoue *et al.*, 2004).

(b) FR fuel restructuring

Owing to the extreme operating conditions of fast reactor oxide fuel (temperature, radiation dose), the original microstructure of the fuel material undergoes significant restructuring during the irradiation (Figs. 34.58 and 34.59). The high central temperature and the steep temperature gradient over the pellet resulting from the combination of low thermal conductivity and high linear rate are among the main driving forces for this. Numerous post irradiation examinations of fast reactor oxide fuels have revealed three distinct radial zones in the fuel (de Halas and Horn, 1963; O'Boyle *et al.*, 1969):

1. The outer rim of the pellet where the *original fuel structure* has survived at relatively low to moderate operating temperatures.
2. An intermediate region of *equiaxed grains*, that have grown at the temperatures of the irradiation.

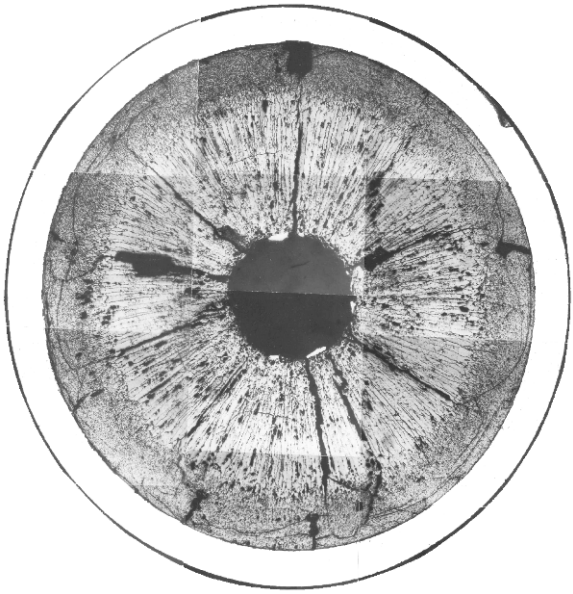

Fig. 34.58 *Typical microstructure of a fast reactor mixed oxide fuel pellet irradiated at high linear heat rate* (*FAFNIR experiment*). (*©European Communities, reproduced with permission*).

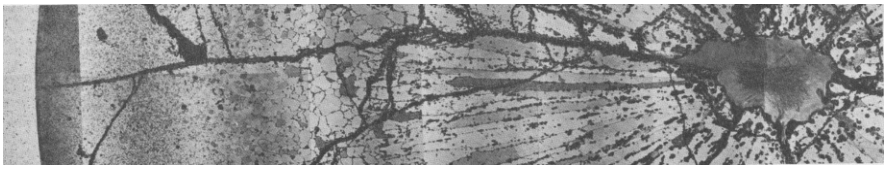

Fig. 34.59 *Section of a fast reactor mixed oxide fuel pellet showing columnar, equiaxed and as-fabricated grains after irradiation (DS1 experiment).* (*©European Communities, reproduced with permission*).

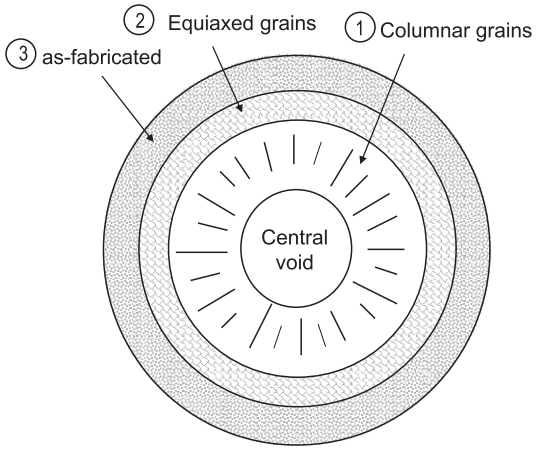

Fig. 34.60 The different zones in a fast reactor mixed oxide fuel pellet. (Olander, 1976).

3. A central region of *columnar grains* that is made up of large grains radiating to the pellet center along the temperature gradient in the hottest part of the fuel.

In the extreme case a *central void* is present at the center of the pellet (Fig. 34.60).

The restructuring is related to the redistribution of the porosity initially present in the as-fabricated fuel (Lackley *et al.*, 1972). There is general agreement that vaporization–condensation processes play a major role in the porosity redistribution. Matter is vaporizing at the hot side of closed pores and is transported to the cold side where it condensates. As a result the fabrication pores migrate up the temperature gradient.

This restructuring is accompanied by significant changes in the concentrations of the major actinides in the radial direction (O'Boyle *et al.*, 1969). Also

re-distribution of oxygen occurs: it migrates to lower temperatures in hypostoichiometric oxides and to higher temperatures in hyperstoichiometric oxides (Rand and Markin, 1968). At the beginning of irradiation fast reactor oxide fuel is generally hypostoichiometric. Because the high fuel operating temperature, the most diffusing species, oxygen, migrates along the thermal gradient from the center towards the colder periphery of the fuel. As a consequence the fuel stoichiometry at the periphery reaches a value close to O/M = 2, whereas the center remains largely hypostoichiometric. Accordingly, the thermal conductivity increases in the outer part of the fuel contributing to a better thermal exchange with the coolant.

Thus, thermal diffusion and/or vapor transport in the temperature gradient of the fuel pellet are key processes affecting the redistribution of matter in reactor fuel pins (Bober and Schumacher, 1973). Thermal diffusion is caused by the differences in the lattice energies of the fuel components in the temperature gradient. This effect becomes significant at temperatures above 1,900°C. Redistribution by vapor transport (vaporization–condensation) due to the different vapor pressures of the fuel components takes place in cracks, voids and pores migrating along the temperature gradient, and in the central cavity. An extensive analytical description of these processes in oxide fuels has been given by Bober and Schumacher (1973).

Post-irradiation examinations have shown that the plutonium concentration increases toward the center of the pellet as a result of the restructuring process. The decrease in oxygen potential towards the central part of the fuel and the process of vaporization–condensation producing the columnar grains cause the redistribution of the plutonium. In hypo-stoichiometric fuel the stronger vaporization of UO_3 and its condensation on the cooler side result in the enrichment in plutonium towards the center part of the fuel. At the same time volatile fission products such as Cs, I and Te as well as Mo move in the opposite direction to cold areas, where they condense between the pellet and the cladding.

The mechanism for the restructuring of fast reactor fuel is thus complex as there is a strong coupling between key parameters such as temperature, thermal conductivity, porosity, oxygen content, and fission product inventory. The formation of the equiaxed and columnar grains is related to the exposure of the fuel to high temperature, close to or above the normal sintering temperature. Equiaxed grains form due to thermally assisted grain growth that continues until a limiting equilibrium size is obtained. This limiting grain size increases as a function of the temperature (Ainscough *et al.*, 1973/1974), but the growth kinetics are strongly affected by the presence of impurities, pores and precipitates. The formation of columnar grains is generally correlated to the mass transport (redistribution) from hotter to colder surfaces of cracks, voids and pores, resulting in their migration to the center of the fuel, leaving behind large elongated crystals oriented along the radius of the pellet (Figs. 34.61 and 34.62).

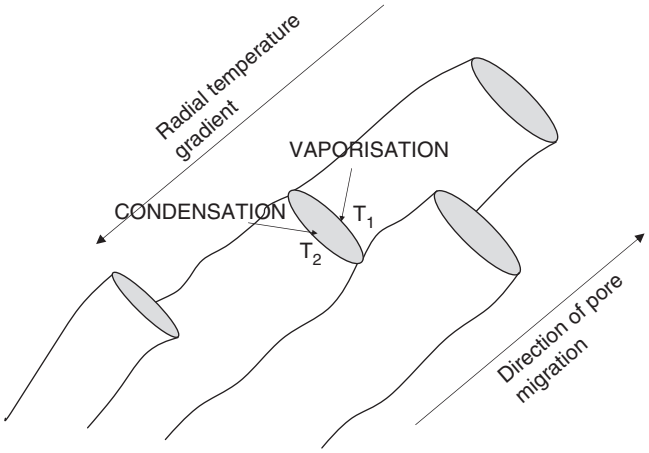

Fig. 34.61 *Schematic representation of the columnar grain formation in a radial temperature gradient*.

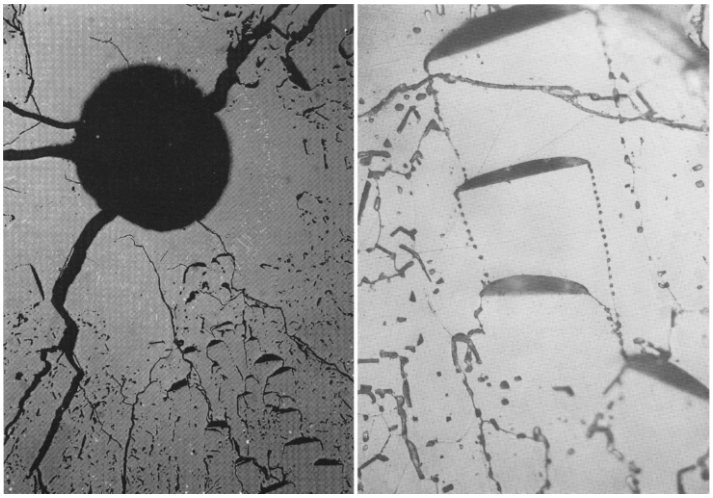

Fig. 34.62 *Lenticular pores observed in irradiated fast reactor mixed oxide fuel.* (©*European Communities*, *reproduced with permission*).

(c) The chemical form of the fission products

Fission product phases have also been identified in fast reactor mixed oxide fuel. O'Boyle *et al*. (1969) observed the presence of metallic precipitates in the columnar grain region as well as the equiaxed grain region. These precipitates

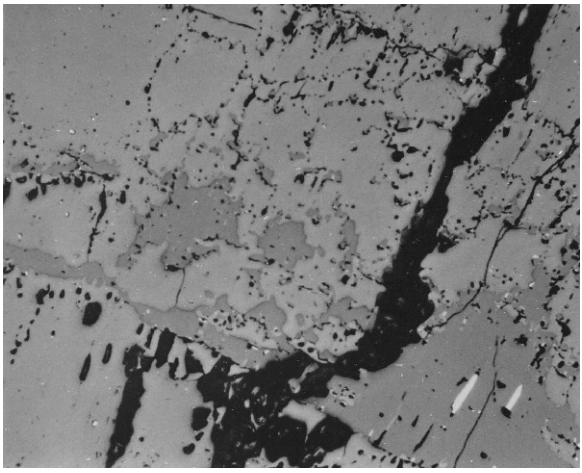

Fig. 34.63 *The grey phase adjacent to the columnar grains in fast reactor mixed oxide fuel.* (©*European Communities*, *reproduced with permission*).

were a (Mo,Tc,Ru,Rh,Pd) alloy, with Ru, Mo and Tc accounting for 90% of the inclusions (Fig. 34.63). Barium was found to be the most abundant fission product in the grey phase, but also the cerium concentration was found to be high in this phase. At low O/(U + Pu) ratio of the mixed oxide, reduction of the hypostoichiometric fuel by the (Mo,Tc,Ru,Rh,Pd) precipitates formed in the early-irradiation period can occur, forming phases like $(U,Pu)(Rh,Pd)_3$ or $(U,Pu)_3(Rh,Pd)_4$. The following reaction takes place (Kleykamp, 1985):

$$\begin{aligned} &3(Mo, Tc, Ru, Rh, Pd) + (n+1)\,(U, Pu)O_{2-x} \\ &\quad = 3(Mo, Tc, Ru) + (U, Pu)(Rh, Pd)_3 + n\,(U, Pu)O_{2-x+\varepsilon} \end{aligned} \tag{34.48}$$

with $n \gg 1$ and $\varepsilon = (2 - x)/n \ll 1$. Kleykamp (1985) observed two different phases with compositions $(U_{1-x}Pu_x)(Rh_{1-y}Pd_y)_3$ and $(U_xPu_{1-x})(Rh_yPd_{1-y})_3$. Ru plays a minor role in these actinide–platinum metal phases, which is consistent with the lower Gibbs energy of formation of URu_3 compared to UPd_3 and URh_3 (see Chapter 19). Palladium, the most volatile of the noble metals, was also detected in the fuel-to-clad joint (Walker, 1978; Tourasse *et al.*, 1992) where it is associated with iron and nickel from the cladding.

O'Boyle *et al.* (1969) observed also the presence of a grey phase in the equiaxed grain region adjacent to the columnar grains and in the mixed-oxide matrix. This grey phase was found to be rich in Ba and Ce. As discussed by Kleykamp (1985) the general formula for this pervoskite-type phase is (Ba,Sr, Cs)(Zr,U,Pu,Mo,Ln)O_3 (where Ln represents the lanthanide elements) with Ba $\gg$ (Sr + Cs).

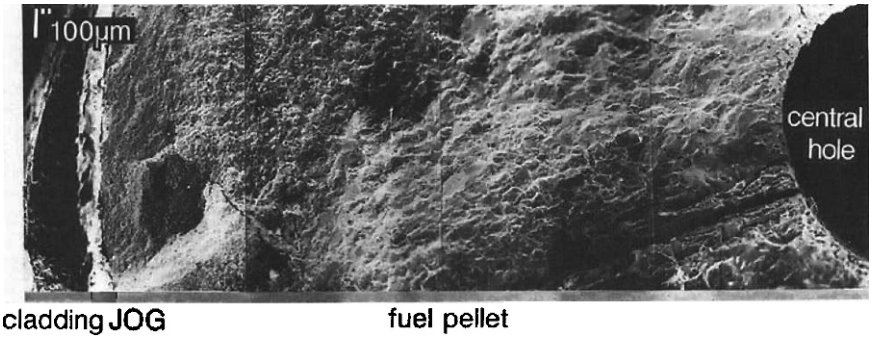

Fig. 34.64 *The oxide phase in the fuel-to-clad joint of fast reactor mixed oxide fuel* (*Tourasse et al.*, 1992). (©*Elsevier*, 1992, *reprinted with permission*).

Owing to the high temperatures and the steep radial temperature gradient in fast reactor fuel, the volatile fission products such as iodine and cesium diffuse out of the hot central region to the colder periphery and the pellet–cladding gap (Neimark *et al.*, 1972; Kleykamp, 1985; Tourasse *et al.*, 1992). Cesium in the gap has been found to be associated with chromium (present in the stainless steel clad of the fuel) and oxygen. It has been suggested that cesium chromate is formed (Antill *et al.*, 1975) but detailed microprobe studies have shown that the phase is chromium oxide (Cr_2O_3) mixed with other phases such as cesium uranate of cesium molybdate (Walker, 1978). In high burnup fuel of the Phénix reactor (Fig. 34.64), an oxide phase containing predominantly cesium and molybdenum has been observed in the fuel-to-clad joint (Tourasse *et al.*, 1992), suggesting that Cs_2MoO_4 could play a role in the transport of material. Other volatile fission products such as cadmium and tellurium, as well as barium were detected in the fuel-to-clad joint.

Also axial redistribution in the fuel pins takes place. Tourasse *et al.* (1992) reported that cesium leaves the hottest parts of the fissile column and concentrates in the upper and lower parts of the fuel pin. This distribution is noticeable at burnup above 9 at.% and its magnitude increases with burnup. Kleykamp (1985) reported slightly different behavior of cesium and iodine in fuel pins containing blanket above and below the fuel stack, the iodine remaining at the fuel/blanket interface and cesium diffusing into the blanket pellets, where it forms $Cs_2(U,Pu)_4O_{12}$.

(d) Fission gas release

Owing to the high fuel temperature, fast reactor oxide fuels show a very high fission gas release (Fig. 34.65), often between 40% and 50% of the gas inventory in the early irradiation stages, and around 80–90% at high burnup (Tourasse

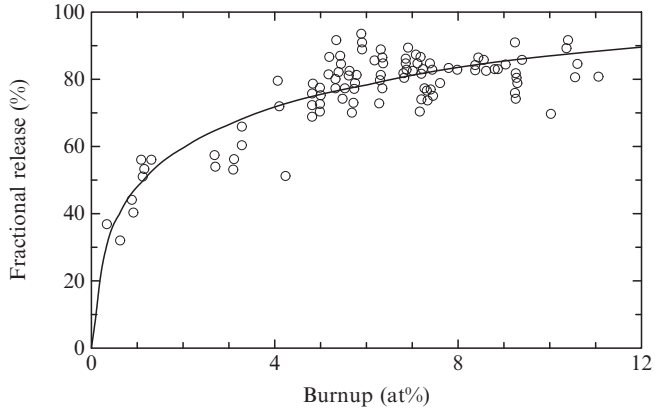

Fig. 34.65 *The fractional fission gas release* (*ratio of the gas released over the theoretical yield*) *of fast reactor mixed oxide fuel in stanard Phénix pins.* (*After Pelletier*, 2008).

et al., 1992; Maeda *et al*., 2005; Pelletier, 2008). As discussed in Section 34.5.4 (d), temperature is one of the key parameters influencing the fission gas release either by favoring the diffusion of single atoms or of bubbles but also via coalescence of bubbles or pore formation together with restructuring (see previous section) that can retain the gases. Clearly above 1,400°C, a temperature typical in fast reactor fuel, the thermally activated processes such as diffusion, sintering, bubble migration enhance the fission gas release.

Post-irradiation examination have revealed that up to a burnup of about 7 at. % fission gas release originates principally from the central restructured zone, while the fission gases in the outer zones are almost completely retained in the matrix (Bailly *et al*., 1999). At higher burnup also the periphery of the fast reactor fuel, where the temperature is moderate and comparable with LWR fuel, releases a considerable amount of its gas inventory, possible due to the microcracking.

(e) Fuel–coolant interaction

In case of a defect/breach in the fuel pin cladding, the liquid sodium coolant can enter the fuel pin and will come in contact with the fuel. Stoichiometric uranium dioxide does not react with pure sodium at moderate temperatures, but a reaction can take place at high temperatures provided excess oxygen is present, for example oxygen dissolved in the coolant or excess oxygen in the uranium dioxide lattice (UO_{2+x}). The oxygen content in liquid sodium for fast reactor coolant is below 10 ppm in mass, typically of the order of 3 ppm, which is well below the maximum solubility (e.g. 6,500 ppm at 1,000 K) (Noden, 1973). From the thermodynamic point of view the compound Na_3UO_4 is in equilibrium with

UO_2 and liquid sodium containing dissolved oxygen (Fig. 34.66). The formation reaction thus can be written as:

$$3Na(O)(l) + UO_2(cr) + O_2(dissolved\ in\ oxide\ or\ Na) = Na_3UO_4(cr) \quad (34.49)$$

In the Na–Pu–O system the analogous phase Na_3PuO_4 exists. It is rhombohedral and forms a continuous solid solution with Na_2PuO_3, the product of the reaction of Na_2O and PuO_2. Na_3PuO_4 is not isostructural with the cubic Na_3UO_4, and as a result the solubility of Na_3PuO_4 in Na_3UO_4 is limited. According to the ternary phase diagram given by Kleykamp (1990), neither Na_3PuO_4 nor Na_2PuO_3 are in equilibrium with liquid sodium (Fig. 34.66). The coexisting phases are Na(O), $PuO_{1.6}$, $Na_4Pu_2O_5$. However, out-of-pile experiments have shown that also the reaction of liquid sodium with PuO_2 yields Na_3PuO_4 (Mignanelli and Potter, 1984).

The quaternary phase $Na_3(U_{1-x}Pu_x)O_4$ has been found as the dominant product of the reaction between $(U,Pu)O_2$ fuel and the sodium coolant in various studies. The Pu/(U + Pu) ratio of the quaternary phase is the same as in the oxide fuel. This phase has a much lower density ($\sim$5.6 g·cm^{-3}) than $(U,Pu)O_2$ ($\sim$10.9 g·cm^{-3}) and its formation can thus lead to significant swelling of the fuel. Moreover, its thermal conductivity is lower than that of the fuel. As a result overheating can occur close to the cladding, eventually leading to propagation of cladding breach and pin failure.

As discussed by Kleykamp (1990, 1997) the reaction starts from the fuel surface by grain boundary penetration of Na. The thickness of the dense reaction layer, which is single-phase under ideal circumstances, increases with the root of time. However, residuals of $(U,Pu)O_{2-x}$ grains that have not yet fully reacted with Na are visible in the $Na_3(U,Pu)O_4$ matrix. The bulk diffusion of Na through the formed $Na_3(U,Pu)O_4$ reaction layer is the rate determining step. The chemical diffusion coefficient is $D_{Na} = 5 \times 10^{-6} \exp(-Q/RT)$ m^2/s with an activation energy Q = 166 kJ/mol between 800 and 1,500 K.

(f) Minor actinide fuel

There is limited experience with minor actinide fuel for fast reactors. Prunier *et al*. (1997) report the results of an irradiation experiment (SUPERFACT) in which the irradiation behavior of mixed actinide oxide fuels was studied in the frame of transmutation research. Low minor actinide content ($U_{0.741}Pu_{0.242}Np_{0.015}O_{1.973}$, $U_{0.745}Pu_{0.237}Am_{0.018}O_{1.957}$) and high minor actinide content fuels ($U_{0.552}Np_{0.448}$-$O_{1.996}$, $U_{0.596}Np_{0.212}Am_{0.192}O_{1.926}$) were irradiated in the Phénix fast reactor (France) and subjected to extensive post-irradiation examinations. The results indicated that the low minor actinide content fuel behaved very similar in comparison to standard mixed oxide fuel. A central hole was formed with columnar grains around it. This was not observed for the high minor actinide content fuel, due to the lower operational power in the absence of plutonium. The fission gas release of all fuels (60–80% of the total

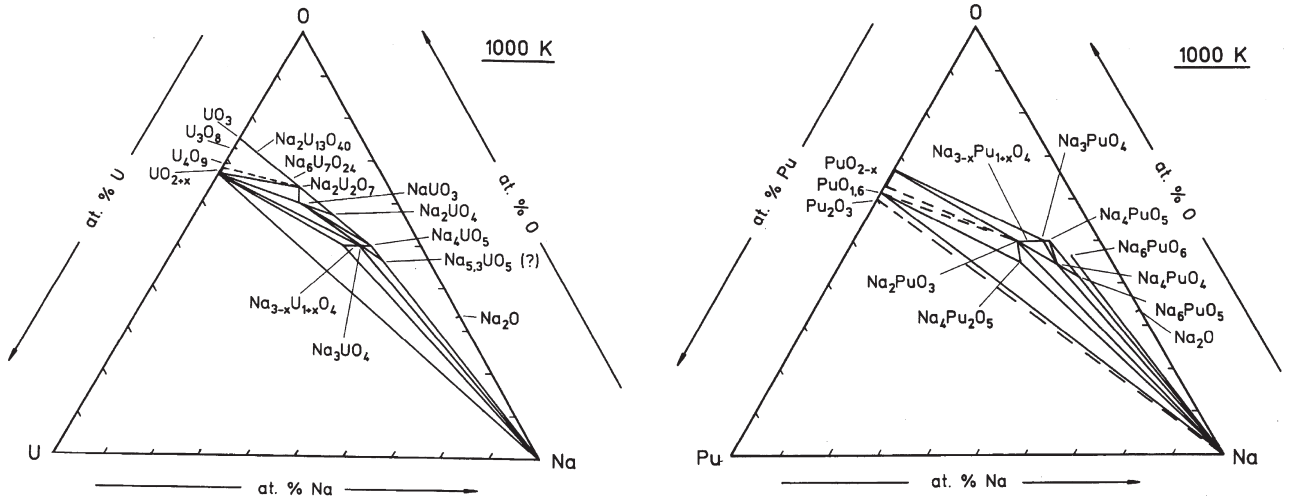

Fig. 34.66 *The isothermal sections of the Na–U–O (left) and Na–Pu–O (right) phase diagrams at T = 1,000 K. (After Kleykamp, 1990). (©Forschungszentrum Karlsruhe, 1990, reproduced with permission).*

yield) was also comparable to that of standard fuel, but the pin puncturing revealed also the release of large amounts of helium. A significant amount of helium was still present in the matrix of especially the $U_{0.596}Np_{0.212}Am_{0.192}O_{1.926}$ fuel. This helium is a result of the decay of the transmutation products of ^{241}Am, as shown in Fig. 34.67. Transmutation of this radionuclide is a complex process, with competition from capture, fission and decay reactions. The formation of ^{242}Cm and its decay to ^{238}Pu is one of the major sources of helium. Microprobe analysis of the fuels showed indeed significant creation of plutonium (^{238}Pu) in the high minor actinide content fuels (Walker and Nicolaou, 1995). These measurements also indicated that the radial distribution of Np and Am was quite flat indicating an even rate of transmutation over the pellet cross section, with in some pins slight redistribution of Pu and Am caused by restructuring.

Picard *et al*. (2000) reported the results of the TRABANT-1 experiment for fuel with composition $(U_{0.55}Pu_{0.40}Np_{0.05})O_2$, irradiated at a linear power of 52–57 kW/m in the high flux reactor (Petten, Netherlands). This fuel reached a burnup of 9.3% and demonstrated a good in-pile performance as shown by the results from the non-destructive analysis.

Tanaka *et al*. (2009) performed a short irradiation experiment on (U,Pu) mixed oxide containing 3–5% Am in the Joyo fast reactor (Japan), with the aim of studying the early irradiation effects. They observed that after an irradiation of 10 min at full power (430 W/cm) the fuel had already developed a central void. Microprobe analysis showed a depletion of U in the zone surrounding the central hole, and an enrichment of Pu and Am. Maeda *et al*. (2009) analyzed the experimental redistributions using models for pore migration by evaporation and condensation, and thermal diffusion, and found good agreement with the pore migration model. Figure 34.68 shows the vapor pressures of the relevant U, Pu and Am vapor species used in that model, indicating that UO_3 is the dominant vapor species above O/M = 1.96. The vapor trans-

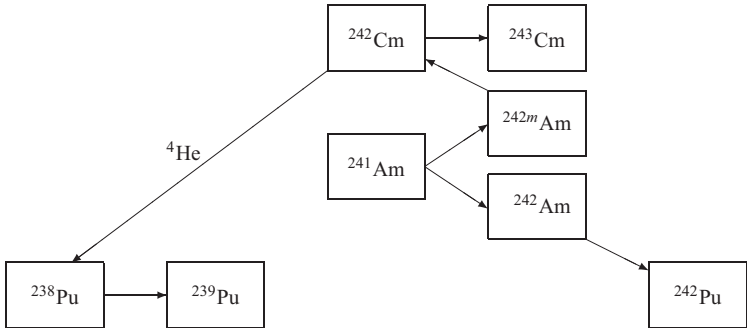

Fig. 34.67 *Transmutation scheme for ^{241}Am showing the various capture and decay processes taking place.*

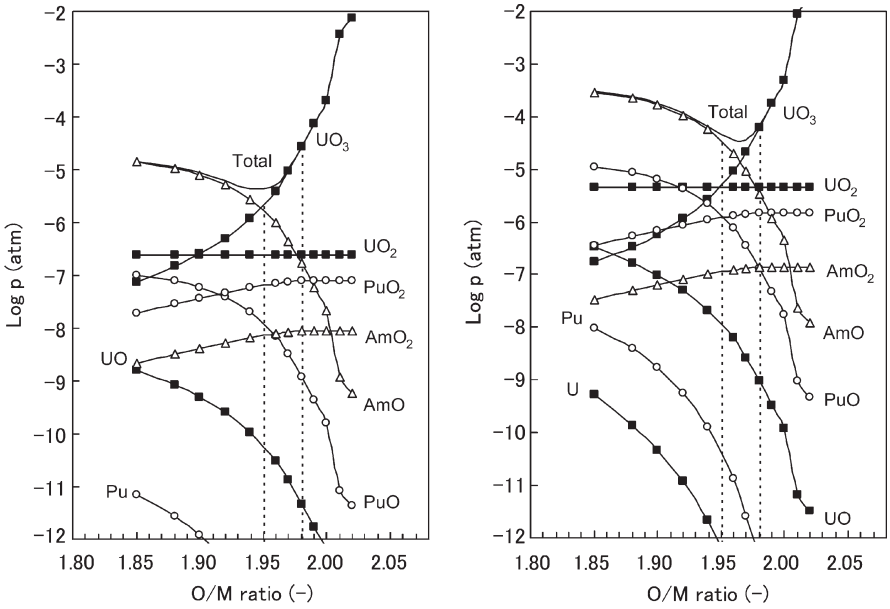

Fig. 34.68 *The vapor pressure of U-bearing, Pu-bearing and Am-bearing gas species above* $(U_{0.69}Pu_{0.29},Am_{0.02})O_{2-x}$ *at temperatures of* 2,073 *K* (*left*) *and* 2,273 *K* (*right*) (*Maeda et al.*, 2009). (©*Elsevier*, 2009, *reprinted with permission*).

ported to the colder side of the lenticular pores is enriched in uranium and as a consequence the hotter side is enriched in plutonium and americium.

These results clearly reveal the complexity of minor actinide oxide fuels. At low linear power the fuels with low minor actinide content behave well, but at high power (high operating temperature) restructuring starts to play a role leading to significant re-distribution of not only Pu, but also Am. This will be even more significant for fuel with a high content of americium, in which also a significant helium production will occur due to the complex transmutation scheme for ^{241}Am.

34.6 FAST REACTOR CARBIDE AND NITRIDE FUEL

34.6.1 The actinide carbides and nitrides

(a) Carbides

The (U,Pu)C fuels have a face-centered cubic NaCl structure, in which the carbon atoms occupy the apex positions and the uranium and plutonium atoms fill the center position ($\frac{1}{2}$, $\frac{1}{2}$, $\frac{1}{2}$) of the cubic structure. In uranium monocarbide UC the carbon atoms, being much smaller than the metal atoms,

can fill the octahedral holes in the metal lattice. By the incorporation of C_2 groups in the octahedral holes, the high temperature form of the dicarbide UC_2 is formed. The uranium dicarbide has a second crystalline form designated as α-UC_2 stable for 1,750 K $< T <$ ~ 2,040 K (tetragonal with a CaC_2 structure, showing an homogeneity range). The sesquicarbide U_2C_3 has a body-centered cubic (bcc) structure and exists only for temperatures below 2,090 K.

Once liquid forms, the solubility of carbon increases rapidly with temperature. Large inconsistencies exist between the numerous experimental data from the literature on the melting point of UC. The recent measurements by laser melting lead to a congruent melting point at 2,781 K (Utton *et al.*, 2008). The uranium monocarbide $UC_{1\pm x}$ has a wide homogeneity range at high temperature (T > 1,400 K) that extends from a slightly hypo-stoichiometric composition ($UC_{0.985}$ at 2,273 K) to uranium dicarbide (β-UC_2). Some experimental investigations between UC and UC_2 have indicated the existence of a miscibility gap with a critical temperature of 2,323 K for $UC_{1.35}$. The extent of this miscibility gap in temperature is still subject of controversy. Some studies suggest a larger extent of the miscibility gap with temperature, which is in disagreement with the existence of a continuous solid solution between UC and UC_2. Further investigations are required to resolve these inconsistencies. Moreover the temperature range of stability of the carbide phases U_2C_3 and UC_2 is still uncertain. This can be related to the very slow rates of formation of U_2C_3 phase and to the stabilization of the UC_2 phase by low oxygen content. The assessed U-C phase diagram is shown in Fig. 34.69 but some further investigations are required to definitely fix the phase relations in this system.

The thermal conductivity of UC has been measured by many authors, as summarized by Lewis and Kerrisk (1976), Matzke (1986) and Blank (1994). Unlike the dioxide in which the phonon contribution predominates at temperatures below about 2,000 K, the thermal conductivity of the monocarbide is dominated by the electronic contribution, i.e. $\lambda_e > \lambda_{ph}$. The thermal conductivity of UC is shown in Fig. 34.72, which indicates a decrease between 300 and 800 K, and a constant value between 800 and about 1,600 K, and an increase above that temperature. The curve can be represented by:

$$\lambda = 22.8 - 5.01 \times 10^{-3}(T/K) + 3.61 \times 10^{-6}(T/K)^2 \qquad 323K < T/K < 973 \tag{34.50}$$

$$\lambda = 19.8 + 1.48 \times 10^{-3}(T/K) \qquad 973K < T/K < 2573 \tag{34.51}$$

The Pu–C system contains four carbides: Pu_3C_2, PuC_{1-x}, Pu_2C_3 and PuC_2 (Fischer, 2008). In contrast to UC, the plutonium monocarbide is always hypostoichiometric. The compound PuC (NaCl structure as UC) decomposes peritectically at 1,875 K into Pu_2C_3 (with the same structure as U_2C_3) and a plutonium-rich liquid phase. PuC_2 (cubic fcc) is only stable at high temperature (above 1,933 K). The currently accepted phase diagram is shown in Fig. 34.69. It still contains large uncertainties due to the lack of experimental data.

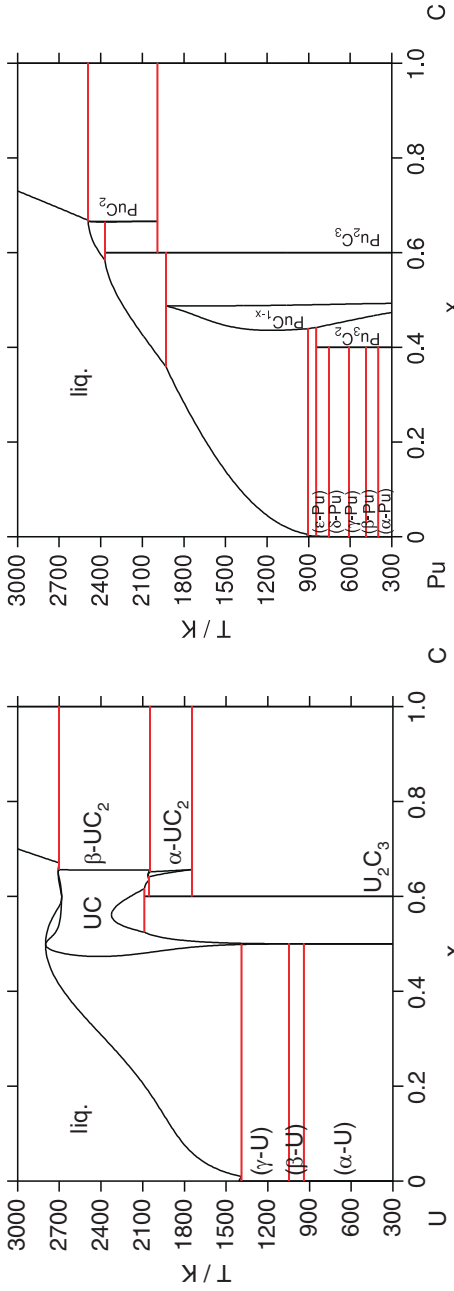

Fig. 34.69 *The assessed U–C (Chevalier and Fischer, 2001) and Pu–C (Fischer, 2008) phase diagrams.*

The thermal conductivity of PuC has been reported to have a behavior that is very different from that of UC. It is comparatively low at room temperature (5 W m^{-1} K^{-1} at 300 K) but increases to a value close to that of UC close to the melting temperature (Fig. 34.72). The results can be presented by the equation:

$$\lambda = 6.44 + 3.38 \times 10^{-3}(T/K) + 1.20 \times 10^{-6}(T/K)^2 \qquad 373K < T/K < 1573 \tag{34.52}$$

No clear explanation has been suggested for this difference.

In the U–Pu–C ternary system, the isostructural monocarbides $UC_{1\pm x}$ and PuC_{1-x} and the sesquicarbides U_2C_3 and Pu_2C_3 form completely miscible mixed carbide phases (Fig. 34.70). The dicarbides UC_2 and PuC_2 are also miscible at high temperature. Because the advanced carbides fuels (U,Pu)C are designed to be slightly hyperstoichiometric with C/M > 1 in order to avoid uranium and plutonium metal formation, the mixed carbide fuels are composed of a matrix of (U,Pu)C with 10–15 wt% $(U,Pu)_2C_3$. As indicated by the orientation of the tielines in the two-phase region, the sesquicarbide contains a significantly higher content of plutonium than the monocarbide. In the UC–PuC system the solidus and liquidus temperatures decrease with the plutonium content in the carbide, as shown in Fig. 34.71. Measurements are available up to 50% Pu in the mixed carbide. No experimental data exist on the solubility of the (U,Pu)C carbide in the metallic liquid phase.

Very little is known about the carbides of the minor actinides, their properties and their solubility in (U,Pu)C. In the Np–C system the same compounds are formed as in the U–C and Pu–C system and Np is expected to behave similar as U. In the Am–C system only the Am_2C_3 phase is known (also expected to be the

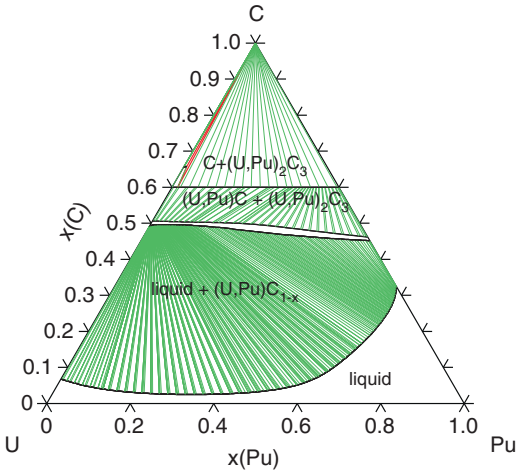

Fig. 34.70 *The U–Pu–C ternary phase diagram at* 1,773 *K* (*Dumas et al.*, 2009).

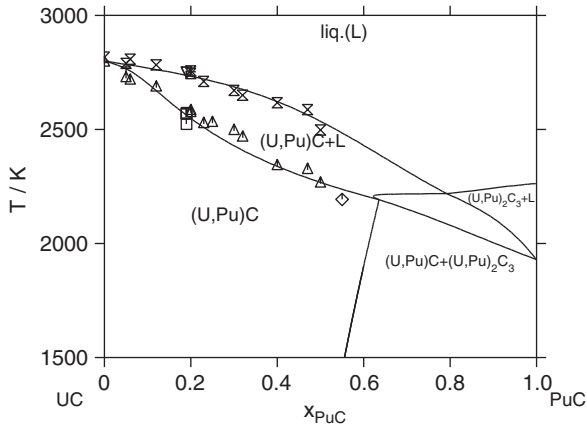

Fig. 34.71 *Assessed UC-PuC isopleth section* (*after Fischer*, 2009).

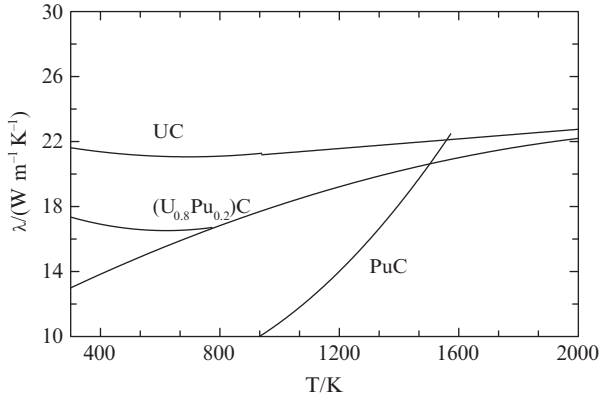

Fig. 34.72 *The thermal conductivity of UC, PuC and* $U_{0.8}Pu_{0.2}C$ *based on the assessment by Lewis and Kerrisk* (1976). *The two curves below 800 K for* $U_{0.8}Pu_{0.2}C$ *indicate probable range of values for this phase.*

only carbide in the Cm–C system), which means that Am (and Cm) will concentrate in the sesquicarbide phase of the fuel.

The thermal conductivity of the mixed carbide (U,Pu)C has been measured by many authors and evaluated by Lewis and Kerrisk (1976). PuC addition to UC leads to a decrease of the thermal conductivity, in line with the values for the PuC end-member, as shown in Fig. 34.72. The data for $U_{0–8}Pu_{0.2}C$ can be represented by:

$$\begin{aligned}\lambda =& 19.7 - 10.10 \times 10^{-3}(T/K) + 8.14 \times 10^{-6}(T/K)^2 \\ & 323K < T/K < 773 \\ \lambda =& 10.24 + 9.74 \times 10^{-3}(T/K) - 1.88 \times 10^{-6}(T/K)^2 \\ & 973K < T/K < 2573\end{aligned} \tag{34.53}$$

(b) Nitrides

Like carbides, the actinide nitrides have a face-centered cubic NaCl structure. In the U–N system, two solid phases exist, the mononitride UN and the sesquinitride U_2N_3 (Fig. 34.73). Two different modifications of the sesquinitride exist: α-U_2N_{3+x} (cubic bcc) and β-U_2N_{3-x} which is stable above about 1,070 K (hexagonal with a La_2O_3 structure type). The melting temperature of UN is dependent on the N_2 pressure: the compound melts at about 3,133 K at 2–3 bar of nitrogen. Large inconsistencies exist on the extent of the composition range of UN. This can be related to different concentrations of impurities (oxygen and carbon) and to the difficulties to quench the uranium rich UN phase to room temperature. The thermal properties of UN are fairly well established and were evaluated by Hayes *et al.* (1990a, b, c). They are summarized in Table 34.11.

In the Pu–N system, the monotride PuN is the only stable phase (Fig. 34.73). The compound is close to stoichiometric although vacancies are allowed on the N sublattice leading to a narrow composition range near N/Pu = 1, but the range of stoichiometry of PuN is not well determined. There is no quantitative information on the phase diagram. The conditions of congruent melting of PuN could not be determined due to problems of sample vaporization. An estimation was proposed by (Spear and Leitnaker, 1968), based on the analogy with ThN and UN, resulting in a melting temperature of (3103±50) K at $p_{N_2}/p_0 = (50 \pm 20)$. For $p_{N_2}/p_0 = 1$ Olson and Mulford (1964) reported the melting of PuN into Pu(1) saturated with nitrogen under release of gaseous N_2 at (2,957 ± 30) K.

The properties of the transuranium mononitrides are relatively well known, as a result of systematic studies by researchers from the Japan Atomic Energy Agency (Minato *et al.*, 2009). In these systems the AnN phase is generally the only stable one, though the high temperature stability changes with increasing atomic number. Of technological importance is the relative high vapour pressure of Am(g) above AmN, as deduced from mass spectrometric measurements for a $(Pu_{0.99}Am_{0.01})N$ sample (Ogawa *et al.*, 1995). A summary of the properties of the AnN compounds is given in Table 34.11.

In the ternary U–Pu–N system, the mononitrides of uranium and plutonium are completely miscible. The isothermal section at 1,000°C reported by Matzke (1986) is shown in Fig. 34.74. The solubility of plutonium in the two forms of uranium sesquicarbide is not known and still remains an open question. Arai *et al.* (1992) made a systematic study of the thermal conductivity of the (U,Pu)N

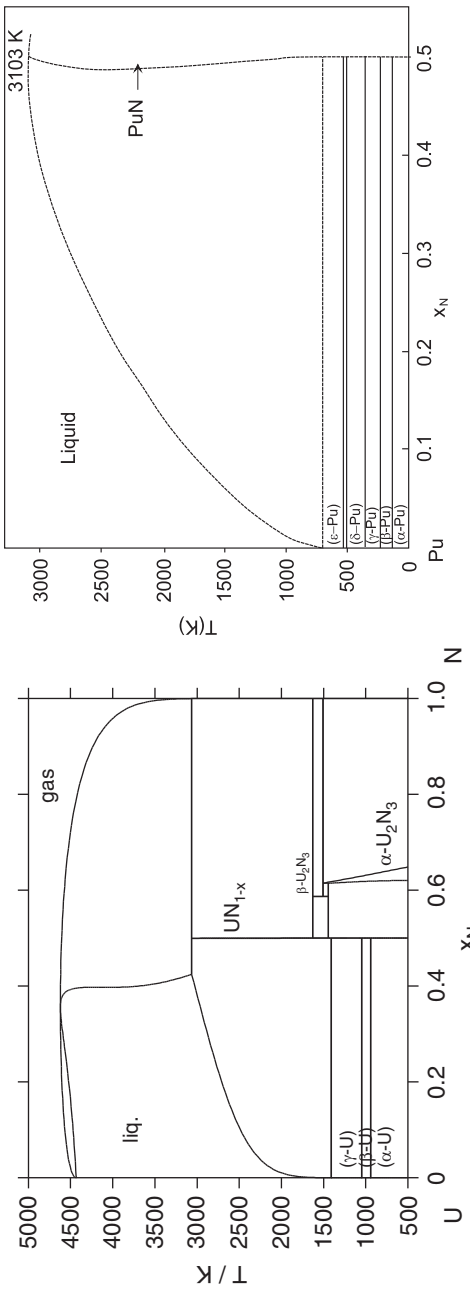

Fig. 34.73 *The assessed U–N phase diagram after Chevalier et al.* (2000) *and the tentative Pu–N phase diagram after Wriedt* (1989).

Table 34.11 *The thermal properties of the actinide nitrides.*

	Equation	*T/K*	*Ref.*
(a) UN			
Thermal expansion	$a(T)/\text{nm} = 0.48790 + 3.264 \times 10^{-6}(T/K) + 6.889 \times 10^{-10}(T/K)^2$	298–2,523	Hayes *et al.* (1990a)
Heat capacity	$C_p/(\text{J}\cdot\text{K}^{-1}\cdot\text{mol}^{-1}) = 40.4263 + 41.1928\times10^{-3}(\text{T/K}) + 31.3066 \times 10^{-6}(\text{T/K})^2 + 10.0570 \times 10^{-9}(\text{T/K})^3 + 0.23304 \times 10^{6}(\text{T/K})^{-2}$	298–3,170	Chapter 19
Thermal conductivity	$\lambda/(\text{W m}^{-1}\text{ K}^{-1}) = 1.864\exp(-2.14p)(\text{T/K})^{0.361}$	298–1,923	Hayes *et al.* (1990d)
Vapour pressure	$^{10}\log(p(N_2)/\text{atm}) = 1.822 + 1.882 \times 10^{-3}(T/K) - 23543.4/(T/K)$	1,400–3,170	Hayes *et al.* (1990c)
	$^{10}\log(\text{p(U)/atm}) = 6.965 - 5.137 \times 10^{-4}(T/K) - 26616.1/(T/K)$	1,400–3,170	Hayes *et al.* (1990c)
Melting point	$T_{fus} = 3{,}035.0(\text{p}(\text{N}_2)0.02832$	[a]	Hayes *et al.* (1990c)
(b) NpN			
Thermal expansion	$a(T)/\text{nm} = 0.48848 + 3.483 \times 10^{-6}(T/K) + 6.274 \times 10^{-10}(T/K)^2 - 7.601 \times 10^{-14}(T/K)^3$	293–1,348	Takano *et al.* (2008)
Heat capacity	$C_p/(\text{J K}^{-1}\cdot\text{mol}^{-1}) = 42.75 + 18.72 \times 10^{-3}(T/K)$	300–1,200	Nishi *et al.* (2008a)
Thermal conductivity	$\lambda/(\text{W m}^{-1}\text{ K}^{-1}) = 7.89 + 1.27 \times 10^{-2}(T/K) - 4.32 \times 10^{-6}(T/K)^2$	740–1,600	Arai *et al.* (1994)
Vapour pressure	$^{10}\log(p(N_2)/\text{atm}) = 13.199 - 29.54 \times 10^{3}/(T/K) + 7.87 \times 10^{-15}(T/K)^5)$	2,480–3,100	Nakajima *et al.* (1997)
	$^{10}\log(p(N\,p)/\text{atm}) = 10.26 - 22{,}200/(T/K)$	2,480–3,100	Nakajima *et al.* (1997)
(c) PuN			
Thermal expansion	$a(T)/\text{nm} = 0.49786 + 4.110 \times 10^{-6}(T\,/\,K) + 69.936 \times 10^{-10}(T/K)^2 - 3.169 \times 10^{-14}(T/K)^3$	298–1,478	Takano *et al.* (2008)
Thermal conductivity	$\lambda/(\text{W m}^{-1}\text{ K}^{-1}) = 20.71 + 3.246 \times 10^{-2}(T/K) - 1.1558 \times 10^{-5}(T/K)^2$	300–1,650	Arai *et al.* (1992)
Heat capacity	$C_p/(\text{J}\cdot\text{K}^{-1}\cdot\text{mol}^{-1}) = 45.002 + 15.42\times10^{-3}(\text{T/K})$	298–2,000	Chapter 19
Vapour pressure	$^{10}\log(p(\text{Pu})/\text{atm}) = 11.74 - 22{,}500/(T/K)$	2,480–3,100	Suzuki *et al.* (1999)
(cd) AmN			
Thermal expansion	$a(T)/nm = 0.49786 + 4.110 \times 10^{-6}\,(T/K) + 9.936 \times 10^{-10}\,(T/K)^2 - 3.169 \times 10^{-14}\,(T/K)^3$	298–1,464	Takano *et al.* (2008)
Heat capacity	$C_p/(\text{J}\cdot\text{K}^{-1}\cdot\text{mol}^{-1}) = 42.44 + 15.63 \times 10^{-3}(T/K)$	300–1,200	Nishi *et al.* (2008a)
Thermal conductivity	$\lambda/(\text{W m}^{-1}\text{ K}^{-1}) = 7.89 + 1.27 \times 10^{-2}(T/K) - 4.32 \times 10^{-6}(T/K)^2$	373–1,473	Nishi *et al.* (2006)

[a] $1 \times 10^{-l3} < \text{P/bar} < 7.5$

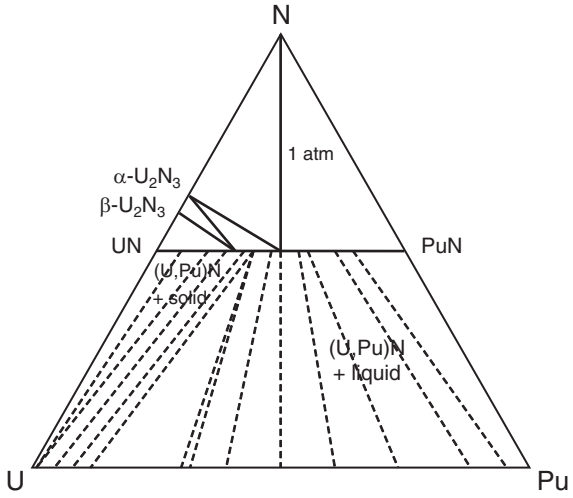

Fig. 34.74 *U–Pu–N phase diagram at* 1,273 *K.* (*After Matzke*, 1986).

solid solution and found a prominent decrease with plutonium content in the UN-rich region and the temperature dependence diminished with the increase of plutonium content (Fig. 34.75). Suzuki *et al*. (1999) studied the (U,Pu)N by X-ray and mass spectrometric techniques and found that the solid solution is not ideal. Takano *et al*. (2008) studied the solid solutions of the minor actinides nitrides with plutonium nitride and found no significant deviation from ideal behavior in this case.

34.6.2 Fabrication of carbide and nitride fuel

(a) Uranium–plutonium carbide

Carbide fuel is generally produced from the oxide via a carbothermic reduction process (Fig. 34.76). In this process the UO_2–PuO_2 mixture used as starting material is mixed and milled with excess carbon, which serves as a reducing agent. To obtain an intimate contact between the powders, the oxide/carbon mixture is compacted and then heated in vacuum or in an argon atmosphere at a temperature around 1,873 K where the following reaction occurs:

$$(1-x)UO_2(cr) + xPuO_2(cr) + 3C(cr) = (U_{1-x}Pu_x)C + 2CO(g) \qquad (34.54)$$

After the heat treatment these compacts (sometimes called clinkers) must be crushed and milled to obtain a powder suitable for the fabrication of the pellets.

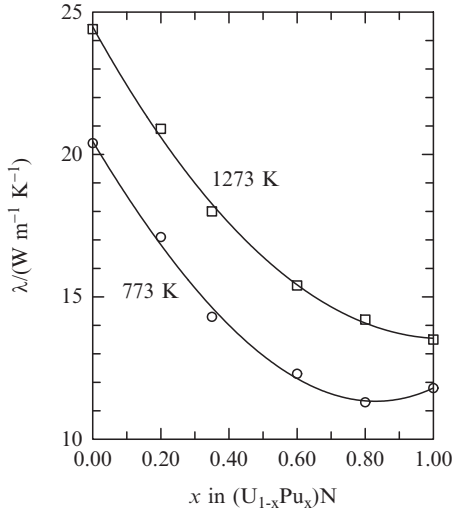

Fig. 34.75 *The thermal conductivity of the (U,Pu)N solid solution at different temperatures.* (*After Arai et al.*, 1992).

Since the mixed carbide powders are pyrophoric, this procedure must be done in a controlled dry and oxygen-free atmosphere.

Due to the poor sinterability of the powders that have already been heated at high temperature, the sintering must be made at very high temperatures (approximately 2,020 K) to obtain an acceptable density. At these temperatures vaporization of plutonium and americium can/will take place, which can be counteracted by adding CO gas to the sintering gas (Richter *et al.*, 1979). Also the use of $(U,Pu)O_2$ solid solution as starting material instead of a mechanical mixture, will help to reduce the losses. When sintering aids are used (e.g. nickel) high density pellets are obtained at lower temperature (approximately 1,770 K) (Gorlé *et al.*, 1974).

Under practical conditions reaction (34.54) is more complex as a slightly hyperstoichiometric product is required to avoid the presence of metal inclusions in the carbide and to improve in-pile behavior. Since (U,Pu)C has only a very narrow composition range at low temperatures (see Fig. 34.70), this means that the product is a two-phase mixture with about 5–15% $(U,Pu)_2C_3$ (Blank, 1994). A too high M_2C_3 content or presence of free carbon will enhance the carburization of the cladding and must be avoided. The difference in thermal expansion of these two phases produces stresses in the pellets. The M_2C_3 can be present as intragranular phase, but often forms a intergranular network. The latter could be an advantage from the point of view of mechanical behavior (Matzke, 1986).

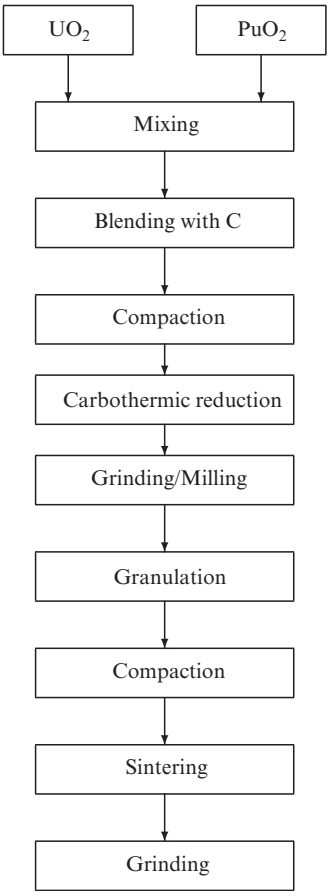

Fig. 34.76 *Schematic representation of the* (*U*,*Pu*) *carbide fuel pellet fabrication process.*

Further complication arises from the fact that the carbides have a high solubility for oxygen. For sodium-cooled fast reactors, initially the goal was to keep the oxygen content low (<500 ppm) but later higher oxygen levels were accepted (1,000–3,000 ppm) as this helps to reduce the M_2C_3 content in the fuel and thus minimizing the cladding carburization (Richter *et al*., 1988). For gas-cooled fast reactor carbide fuel with SiC cladding, an advanced concept that is currently studied (Yvon and Carré, 2009), a low oxygen content is required to avoid reaction with SiC.

(b) Uranium–plutonium nitride

In the past nitride fuel has been produced by direct nitriding of the metal with N_2 or NH_3 gas, but nowadays nitride fuel is generally produced from the oxide

via a carbothermic reduction process. Similarly to the carbide fuel production, the UO_2–PuO_2 starting material is mixed and milled with carbon, which serves as a reducing agent. Generally an excess of carbon (C/M ≈ 2.2–2.5) compared to the stoichiometric value of 2.0 is added. The mixture is then compacted and heated in an nitrogen atmosphere at a temperature above 1,600°C:

$$(U,Pu)O_2(cr) + 2C(cr) + \frac{1}{2}N_2 = (U,Pu)N(cr) + 2CO(g) \qquad (34.55)$$

Due to the fact that during reactor irradiation the radiotoxic isotope ^{14}C is formed as a result of the $^{14}N(n,p)^{14}C$ reaction, the nitride fuel must be fabricated with enriched ^{15}N (natural nitrogen contains 0.37% ^{15}N, the remainder 99.63% being ^{14}N). As the enrichment is relatively costly, and an enrichment of at least 99% is required, the nitrogen gas must be recycled during the fabrication, and eventually during reprocessing (Wallenius and Pillon, 2001).

Arai and Minato (2004) reported the fabrication of the actinide mononitrides UN, NpN, PuN, AmN, CmN and their solid solutions by carbothermic reduction from the corresponding dioxides. Because the thermodynamic stability of the heavier actinides is lower and that of the oxides is higher compared to the light actinides, the amount of excess carbon added was adjusted element by element to obtain mononitrides with high purity. AmN is a special case as loss of Am due to evaporation could occur during fabrication, which can be mitigated by lowering the temperature of carbothermic reduction by about 200 K compared with the other actinide nitrides (1,573 K) and using a molar mixing ratio of C/AmO_2 higher than 3.0. A similar problem occurs when sintering samples containing AmN, as Am losses were observed when preparing dense materials. Metal vaporization can be partially counteracted by a small partial pressure of nitrogen in the sintering atmosphere (Jolkonnen *et al.*, 2004).

34.6.3 The FR carbide and nitride fuel pin and element

As discussed in Section 34.5.5, most fast reactors concepts are based on pellet-in-pin designs. However, not only the helium bonded fuel pin are considered for fast reactor carbide or nitride fuels, but also sodium bonded pins (Kittel *et al.*, 1993), which is possible due to the good compatibility of the carbides and nitrides with liquid sodium.

Dense carbide and nitride fuels are of special interest for fast reactors that operate at high linear heating rate. In contrast to the traditional pellet-in-pin concept considered for the LFR and SFR, a very innovative fuel pin/element design has been proposed for the GFR (Chauvin *et al.*, 2007): hexagonal arrays with a fuel disk in each alveolus. Mixed actinide carbide $(U_{0.80}Pu_{0.20})C$ is the reference fuel, not because of the high linear heating rate, but to assure a high density of heavy atoms. Due to the high neutron dose (100–150 dpa) and the high operating temperatures (500–1,200°C in normal operation up to 1,600°C in

accident conditions) of the GFR, ceramic materials (e.g. SiC, ZrC, TiC) are the reference option for the cladding materials. A liner made of a metal alloy (e.g. W-Re) between the actinide carbide and the cladding is foreseen as barrier for the fission product release. A thin layer of a metal alloys (e.g. W–Re, Mo–Re) between the actinide carbide and the MC carbide is foreseen as barrier for the fission product release.

34.6.4 In-reactor behavior of carbide and nitride fuel

Dense carbide and nitride fuels have been and are still studied for advanced fast reactor concepts in which high linear power is foreseen. Compared to the oxides, MC carbides and MN nitrides (M = U and/or Pu) offer a higher thermal conductivity (by approximately a factor of 7–8), a larger metal atom density (by 30% for MC and 40% for MN) and less moderation (one C or N vs two O per metal atom). The irradiation behavior of these fuels was widely tested (see for example the monograph by Matzke (1986)), mainly in connection with their planned use in liquid metal-cooled fast neutron breeder reactors (LMFBRs). As mentioned above liquid sodium bonded and helium bonded pins have been studied (Kittel *et al*., 1993). The sodium bond has the advantage of lower central fuel temperature and the concomitant fission gas retention, which might however be released during power transients. The lower temperature leads also to a greater degree of swelling, but this can be accommodated by a larger gap, as the thermal conductivity of sodium bond is high. The helium bonded concept leads to a higher fuel temperature and thus a more pronounced fission gas release and thus lower swelling.

The rock salt-structured MC and MN compounds should be stable against amorphization based on the criteria mentioned above, and this was confirmed in many experiments, e.g. self-damage due to α-decay, ion implantation experiments, and reactor irradiations up to high burnup (Matzke, 1986). Both tailored capsule irradiation with controlled parameters and full-scale fuel pin irradiations were made. The total database for the advanced fuels is, however, just a small fraction of that for the oxides, and the experiments were made under widely varying conditions.

The radiation effects in MC and MN fuel are similar to UO_2, but occur at different doses and temperatures. Polygonization occurs at burn-ups in excess of $\sim$5 at. %, and an increase of lattice parameter was observed due to damage ingrowth caused by self-damage in Pu-doped specimens as well as by reactor irradiation. Figure 34.77 shows an example of the volume increase or swelling due to α-decay self-damage in $(U_{0.8}Pu_{0.2})C$, the 20% Pu being short-lived ^{238}Pu, during storage at ambient conditions for 60 days. The increase was larger than that due to the concomitant increase in lattice parameter. No transmission electron microscopy study was made, but the probable reason for the difference is formation of He-filled bubbles.

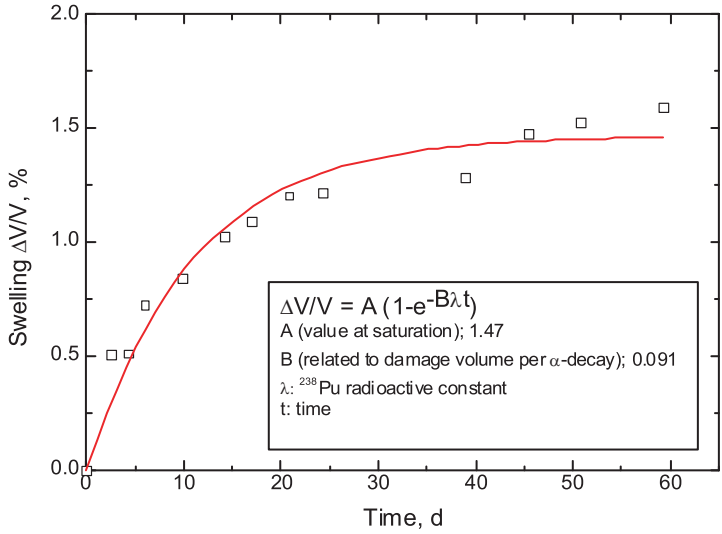

Fig. 34.77 *The volume increase due to α-decay self-damage in* $(U_{0.8}{}^{238}Pu_{0.2})C$, *after Matzke* (1985). *The values have been fitted with the equation described in the inset.*

Matsui *et al.* (1981) have measured different properties (lattice parameter, electrical resistivity, hardness, magnetism) of UC and UN before and after reactor irradiation. The recovery of the observed changes during annealing was measured also. Similar data were obtained for UO_2 and in comparison less defect annealing occurred during fission in UC and UN, which was attributed to the higher thermal conductivity and concomitant lower operating temperature. Consequently, thermal and pressure spikes were expected to be less pronounced than in UO_2, and there was no indication of fast mobility of U-interstitials in UC and UN contributing to fission-enhanced mass transport. The results for fission-enhanced diffusion of U and Pu are compatible with this explanation. The measured D^*-values were temperature independent, athermal between 150 and ~1,100°C and were described by a relation similar to that for oxides (see Section 34.5.4 (d), equation (34.43)), i.e. $D^* = AF$, F being the fission rate in fissions cm^{-3} s^{-1}. The A-value was, however, smaller than that for the oxides by a factor of 5 for MC and a factor of 6.7 for MN. These results are inversely proportional to the thermal conductivities which are, at 1,000°C, in the order UO_2:UC:UN, normalized for UC, 0.15:1:1.2, and indicate less defect mobility during fission in the advanced fuels. Athermal fission-enhanced creep and densification even at low temperatures were also found for both UC and UN, less pronounced than in UO_2.

There is substantial information on the irradiation behavior of mixed (U,Pu) carbides from irradiation programmes in US and Europe in the 1960s and 1970s. More than 5,000 fuel pins have been tested, with helium gas and liquid

sodium bonds in pellet type and vibrocompacted configurations. The early irradiation results indicated that carbide pellet fuel of 70–80% smear density can only be operated at moderate linear heating rate, and showed no clear distinction between the helium and sodium bonded concepts in spite of the higher centerline temperature of the former. However the helium bonding was favored because sodium bonding was more difficult and thus more expensive.

The irradiation behavior of carbide fuel is determined by the density, oxygen content and M_2C_3 content, among others. If the oxygen content is high the excess carbon can migrate to the colder part of the fuel, and the M_2C_3 content in the colder outer zone of the fuel increases (Matzke, 1986), which then shows significant swelling. Fission gas also accumulates in the M_2C_3 phase (Fig. 34.78), enhancing this effect.

An advanced development programme for (U,Pu)C fuel for the Indian breeder programme was performed at Indira Gandhi Centre for Atomic Research (IGCAR) for the fast breeder test reactor (FBTR) (Majumdar *et al.*, 2006). This reactor has been successfully operated with a high plutonium containing hyperstoichiometric mixed carbide fuel since October 1985. Initially $(Pu_{0.7}U_{0.3})$ C fuel was employed at low power levels. Later the fuel was replaced by $(Pu_{0.55}U_{0.45})$C fuel. The results indicated a good in-pile behavior of the high

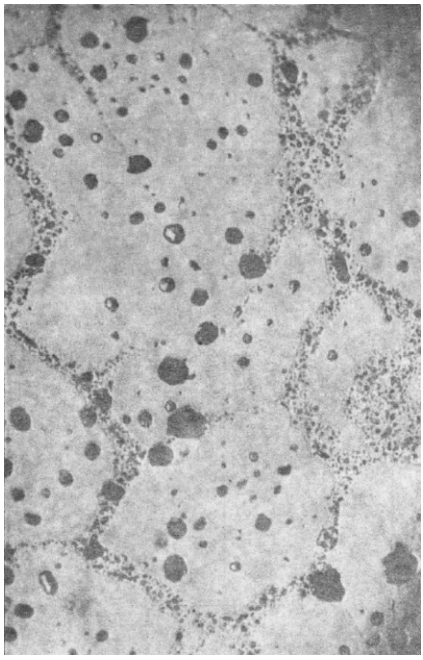

Fig. 34.78 *The M_2C_3 phase at the grain boundaries in (U,Pu)C fuel showing a high concentration of gas bubbles.* (©*European Communities, reproduced with permission*).

Pu content fuel up to 140 MWd/kgHM and the lower Pu content fuel up to a burnup of 100 MWd/kgHM, though the linear power remained low (about 250 W/cm).

Ray and Blank (1984) presented an analysis of the defect structure and of small fission gas bubbles for mixed carbide fuels with burn-ups between 1.8 and 11 at.% by transmission electron microscopy (TEM). A complex defect structure consisting of dislocations, loops and at least three types of solid fission product precipitates was observed. Na-bonded carbides develop predominantly a dislocation network increasing in density with burn-up whereas He-bonded carbides showed mainly a corresponding network of crystallographic needle-like precipitates. Locally the nucleation and growth of small fission gas bubbles 1–20 nm in diameter (bubble population *P*) is closely related to their dislocation or needle environment. Larger bubbles with diameters of 30–50 nm appear to be mostly associated with plate-like precipitates or dislocation boundaries. The local swelling contribution of a bubble population is $<0.5\%$ and its fission gas content is 4–5% of the total amount of gas created over the whole burn-up range investigated.

There is limited irradiation experience with UN and (U,Pu)N fuel compared to carbide fuel, and the results are not conclusive. Early irradiation experiments have shown that the fabrication porosity strongly affects the swelling and fission gas release. At low temperatures ($<$1,500 K) athermal swelling is dominant, resulting from the precipitation of fission products. Fission gas release is low. At higher temperatures thermal swelling dominates, mainly due to migration and coalescence of bubbles. The critical temperature above this rapid increase depends strongly on impurities (oxygen, carbon). At high burnup the (free) swelling saturates and the structure evolves to a network of interconnected porosity. The fission gas release is consequently high (70–80%).

Tanaka *et al*. (2004) reported the results of non-destructive and destructive post irradiation examinations of two (U,Pu)N fuel pins with different He-gap width, irradiated at a linear heating rate of 750 W/cm to 4.3% FIMA in the experimental fast reactor JOYO (Japan). Fission gas release was about 3.3% and 5.2%, and swelling about 1.8% and 1.6%, respectively. The porosity of the pellet was about 40% in the center, and 10% in the outer zone of the pellet. From the radial distributions of Xe concentration measured by electron probe micro analysis (EPMA), it was determined that approximately 80% and 15% of fission gases were retained in the intragranular region and in the fission gas bubbles, respectively. Deformation of the fuel cladding differed between the tested fuel pins. Uniform deformation of the cladding due to fuel cladding mechanical interaction (FCMI) was observed in the fuel pin with a smaller gap width, but significant oval deformation was seen in the fuel pin with a larger gap width. In the latter, the large space for the movement and relocations of the fuel fragments led to nonuniform relocation, resulting in the oval deformation of the cladding. It was concluded that the larger fuel-cladding gap aimed at accommodating the fuel swelling would not be acceptable for He-bonded nitride fuel

pins. To demonstrate the irradiation performance of nitride fuel for fast reactors, it is necessary to carry out irradiation tests aiming at higher burn-up in the future. From the viewpoint of mitigating FCMI, the proper fuel design and porosity control manner of nitride fuel may also be required.

Due to their lower operating temperature, carbide and nitride fuels generally show less restructuring than oxide fuels. However, the fundamental processes are similar to oxide fuel, i.e. a highly porous zone in the center of the fuel pellet, a dense pseudocolumnar grain zone, a zone of transition from low to higher swelling and higher gas release, and the outer zone of low swelling and low gas release (Blank, 1994). An example of a structure of a high linear power carbide fuel is shown in Fig. 34.79.

The fission product chemistry of the carbide and nitride fuels is determined by the solubility in the fuel phases. Fission products such as the lanthanides, zirconium and niobium can be incorporated in the MC and MN phases. The noble metals (Pd, Ru, Rh, Tc) in contrast have very limited solubility and tend to form intermetallic phases like $(U,Pu)(Pd,Rh,Ru)_3$ (Bramman *et al.*, 1971). However, in carbide fuel ternary carbides phases of the type U_2MC_2 have also been observed, depending on the carbon potential. For example Kleykamp (1973) identified the fission product precipitates in the outer zones of irradiated UC samples (0.7 at.%) as $U_2(Tc,Ru,Rh)C_2$ by microprobe analysis. The gaseous and volatile fission products have a very low solubility in the fuel matrix, and tend to precipitate in bubbles or at grain boundaries.

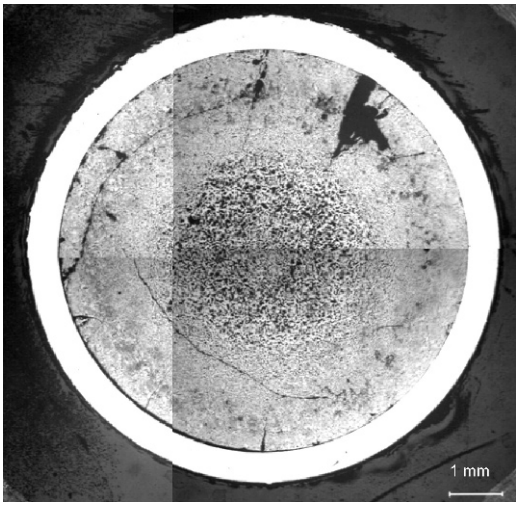

Fig. 34.79 *Optical ceramography of a (U,Pu)C fuel (NIMPHE2 irradiation) showing the structure typical for high linear power fuel (Haas et al., 2009). (© European Communities, reproduced with permission).*

The chemical interaction between (U,Pu)C fuel and clad can lead to carburization of the stainless steel clad during long irradiation times and thus cause cladding embrittlement, leading to a decrease the fuel lifetime. When considering the Gibbs energies of the monocarbides of U and Pu present in the fuel and of Fe, Cr, Ni present in the the cladding, the carbides of Fe and Cr cannot form. But the phase diagrams U–C–Fe, U–C–Cr and U–C–Ni indicate that intermetallic phases such as UFe_2 or UNi_5 may precipitate. In addition, a low temperature eutectic can form between UC and the cladding metals. The problem of compatibility depends on the stoichiometry of the fuel carbide. In case of hypostoichiometric MC_{1-x} the presence of free uranium can lead to the formation of intermetallic compounds such as UFe_2 or UNi_5. In case of hyperstoichiometric MC_{1+x} containing M_2C_3, a significant carburization of the cladding may occur according to the reaction:

$$MC_{1+x} + (Fe, Cr) = MFe_2 + (Fe, Cr)_{23}C_6 \tag{34.56}$$

The clad carburization increases with carbon activity and with x in MC_{1+x}. There is no influence of the fission products on the carbon activity (Lorenzelli and Marcon, 1972). In contrast, the presence of oxygen has to be taken into account as it decreases the carbon activity. In practice a temperature limit has to be taken into account below which carburization is acceptable (kinetically hindered), for example 900°C for 319 stainless steel (Mouchnino, 1969).

The chemical interaction of (U,Pu)N fuel with the cladding is less problematic than for (U,Pu)C. The nitrides have an excellent compatibility with stainless steel, as long as hypostoichiometry $(U,Pu)N_{1-x}$ is avoided. Hyperstoichiometry could lead to chromium nitride formation, as experimentally observed, but this has no negative effects on the clad properties.

34.7 FAST REACTOR METALLIC FUEL

34.7.1 The actinide metals

(a) Uranium and uranium alloys

α-Uranium, the allotropic stable form at room temperature, has an orthorhombic crystal structure. This structure is stable up to 941 K. β-Uranium has a tetragonal structure and is stable to 1,042 K. At this temperature it transforms into the cubic γ modification that melts at 1,407 K. Due to the low crystallographic symmetry, the α and β phases are anisotropic and anisotropic radiation growth has been found to be one of the major obstacles for the use of α-uranium as fuel material (see below). This was partially controlled by using fine-grained randomly-oriented material and such unalloyed material has been used for the first core of the EBR-I reactor in the USA.

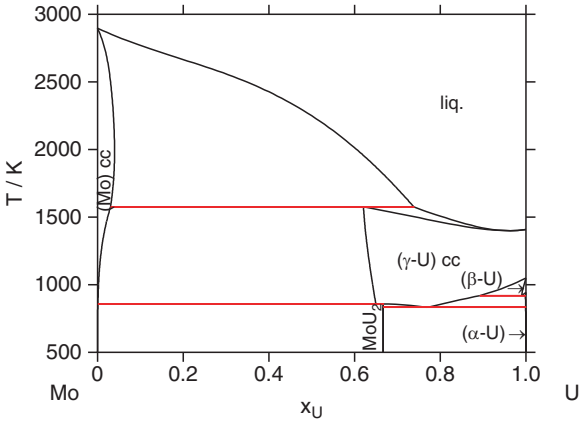

Fig. 34.80 *The assessed Mo–U phase diagram.* (*After Guéneau et al.*, 2007).

Another solution to avoid the anisotropic radiation growth of the metal fuel, needed to reach high burnup, is alloying to stabilize the isotropic γ or δ phases. For these reasons extensive research has been performed into alloys with a refractory element, such as Cr, Mo, Ti, or Zr. Alloying uranium with these elements lowers the temperature at which the γ phase is stable and, when added in significant amounts, increases the melting temperature. Another reason to alloy the uranium was to increase the chemical compatibility with cladding materials. The latter was the reason that U-2wt%Zr (α) was used for the Mark-II and Mark-III cores of the EBR-I reactor, and U-0.1 wt%Cr (β) for the first core of the Dounray Fast Reactor.

U-Mo alloys were seen as very attractive. With the addition of about 20 mol% the gamma phase can be stabilized (Fig. 34.80) but its thermal stability was limited (<923 K) due to the transformation of the γ phase to the α and β phases, though this transformation is reversed at high radiation doses. Better behavior was obtained by adding ruthenium to the binary alloy, resulting in the U–Mo–Ru or U–Fs fuel (where Fs means fissium, a mixture of fission products). More than 30,000 U–Fs alloy fuel elements have been irradiated in the EBR-II reactor in the USA. In parallel the U–Zr alloy was developed in the USA, which showed similar behavior but which was significantly less costly.

(b) U–Pu alloys

Plutonium shows even more crystallographic modifications between room temperature and its melting point, 913 K. The cubic δ phase is stable above 736 K, and can be stabilized by Al, and Pu-1.25 wt%Al was used in the first metal-fueled reactor (Clemetine, USA). But plutonium and Pu-Al alloys have very low melting points, which makes them unattractive as fuel material.

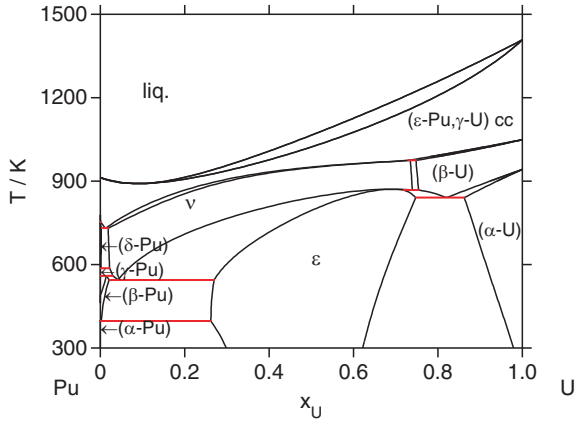

Fig. 34.81 *The assessed U–Pu phase diagram.* (*Kurata*, 1999).

Uranium and plutonium are completely miscible only in the bcc (body-centered-cubic γ-U and ε-Pu) phase just below the solidus/liquidus transition (see Fig. 34.81). At lower temperature, terminal solid solutions with limited mutual solubilities of respectively Pu in α-U (orthorhombic), β-U (tetragonal) and of U in α-Pu (monoclinic), β-Pu (body-centered monoclinic), γ-Pu (face-centered orthorhombic), δ-Pu (face-centered cubic), and δ'-Pu (body-centered tetragonal) exist. In addition, two intermediate phases designated as ν and ε exist with wide composition ranges. Thus for alloys up to 20 mol% Pu the problem of dimensional instability is similar to that of α uranium metal. Moreover, the melting point of the (U,Pu) alloy is considerably lower than that of uranium metal. Finally, binary uranium-plutonium alloys face the problem that plutonium forms eutectic melts with iron and nickel present in cladding materials for fast reactors.

In the 1980s the ternary U–Pu–Zr alloy fuel was developed for EBR-II, building on the experience for the U–Zr fuel. Zirconium in this fuel served primarily as an aid to mitigate fuel–cladding interaction. The upper Zr concentration was set to about 10 wt% for plutonium concentrations of up to 20 wt%, because for higher zirconium concentrations the liquidus temperature would exceed the softening point of the quartz molds used in the injection-casting fabrication equipment (Hofmann *et al.*, 1997). The thermal conductivity of U–Pu–Zr alloy fuel was evaluated by Ogata (2002) from data for U–Zr and U–Pu–Zr alloys:

$$\lambda = 16.309 + 0.02713(T/K) - 46.279x_{Zr} + 22.985x_{Zr}^2 - 53.545x_{Pu} \quad (34.57)$$

where x is the atomic fraction. This equation is valid for $x_{Zr} < 0.72$, $x_{Pu} < 0.16$ and $T < 1{,}173$ K.

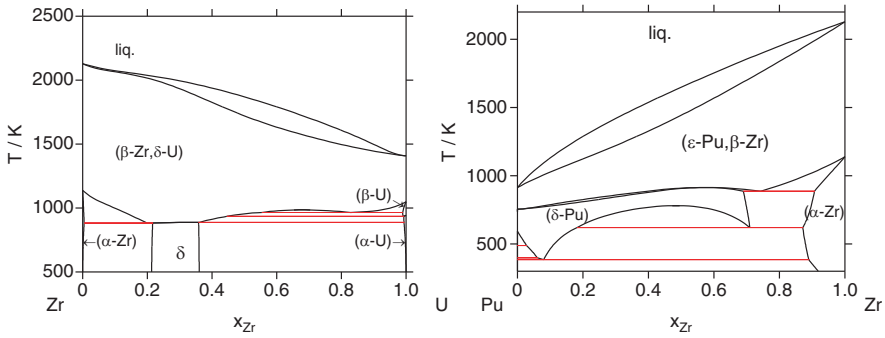

Fig. 34.82 *The assessed Zr–U* (*Chevalier et al.*, 2004) *and Pu–Zr phase diagrams* (*Kurata*, 1999).

Zirconium is completely miscible with uranium and plutonium in the bcc phase at high temperature (Fig. 34.82). At lower temperature, zirconium has a wide solubility in δ-Pu. The solubility of zirconium in the other forms of U and Pu are very low (Fig. 34.82). An intermediate phase designated as "δ" forms in the U–Zr system with a composition close to UZr_2. The phase diagram of the U–Pu–Zr ternary is shown in Fig. 34.83. For typical composition U–19Pu–10Zr (wt%), the alloy forms a bcc solid solution (γ-phase) in the temperature range (923–1,023 K). Between 873 and 923 K, the fuel is a two phase mixture composed of γ and ε phases. Below 873 K, the γ phase transforms to the δ phase and the alloy is a two phase mixture of δ and ε phases.

(c) Minor actinide alloys

The phase diagrams of the Np–U and Np–Pu systems are shown in Figs. 34.84 and 34.85. Neptunium has a high solubility in the α and β forms of uranium and plutonium, and a continuous solid solution exists at high temperature with γ-U and ε-Pu with a bcc structure. According to the assessed Np–Zr phase diagram by Ogawa (1995), neptunium has a very low solubility limit in the α form of zirconium. On the contrary, the solubility of neptunium in β-Zr is high.

The phase diagram of the Am–U system is shown in Fig. 34.84. Contrary to neptunium, americium has a limited solubility limit in all the uranium forms and a miscibility gap exists in the liquid state. The solubility of americium in α, β and γ forms of plutonium is very low. But a continuous solid solution exists in a wide temperature range between δ-Pu and β-Am with a fcc structure. There is no information on the phase diagram of the americium–zirconium system.

The effect of small amounts of Am and Np minor actinides (1.2–1.3 wt%) in U–Pu–Zr was investigated by Kim *et al.* (2004). The observations show that these small additions do not change the microstructure of the fuel.

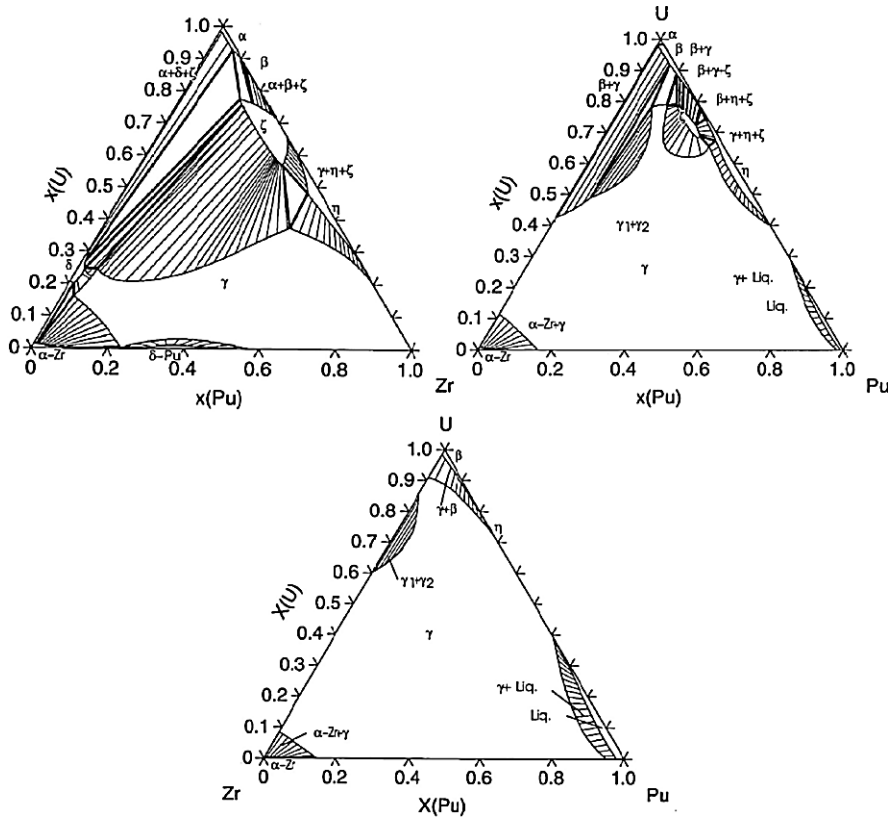

Fig. 34.83 *The assessed Pu–U–Zr isothermal section at* 868, 933 *and* 973 *K.* (*Kurata*, 1999).

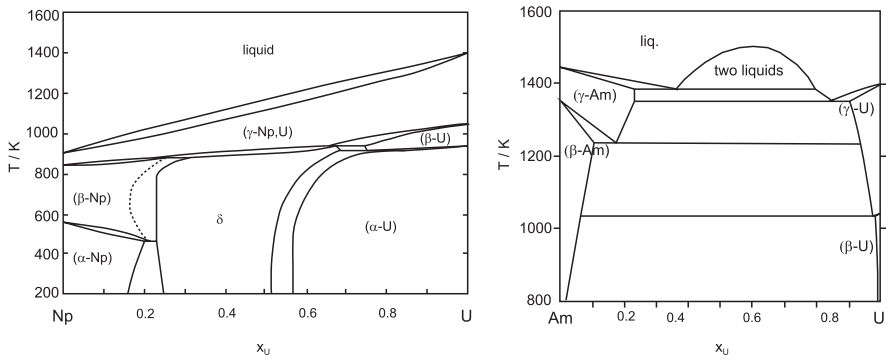

Fig. 34.84 *The assessed Np–U* (*Predel*, 1998) *and Am–Pu* (*Ogawa*, 1995) *phase diagrams.*

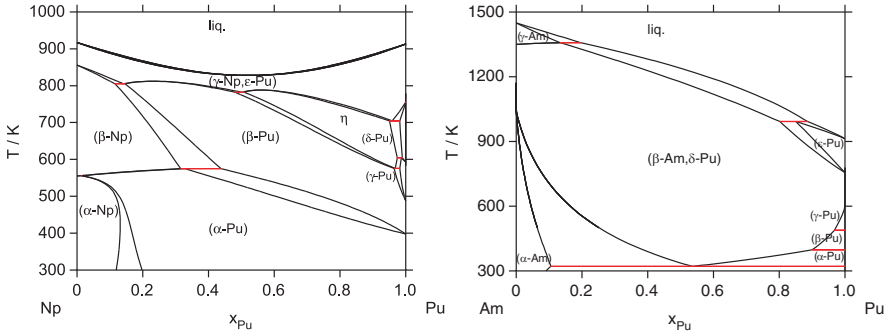

Fig. 34.85 *The assessed Np–Pu and Am–Pu phase diagrams* (*Dupin et al.*, 2009).

The concentration distribution in the fuel shows that the behavior of neptunium is similar to that of plutonium whereas americium seems to behave like zirconium.

Since the fabrication technology for U–Pu–MA alloys will have to be different from that of U–Pu alloys (see below), larger quantities of zirconium can be added to the fuel compared to (U,Pu,Zr). Keiser *et al.* (2008) studied U–Pu–Am–Zr (with 7 wt% Am) and U–Pu–Am–Np–Zr (3–4 wt% Am and 2 wt% Np) alloy compositions from 20 to 40 wt% Zr, and found that at the highest Zr concentration only the δ phase is formed whereas at lower Zr concentrations also a binary ζ(U,Pu) phase is formed, whose amount increases with decreasing Zr concentration.

34.7.2 Fabrication of metal fuel

A variety of fabrication methods for metal fuels has been developed in the course of time (Burkes *et al.*, 2009). For the Mark-I core and blanket of the EBR-I reactor in the USA fine grained α-uranium fuel was produced by rolling the metal in the alpha phase or quenching it from the β phase (Kittel *et al.*, 1993). Co-extruding of the U–Mo alloy in zirconium tubing was used for the production of the fuel for the Fermi reactor in the USA (Kittel *et al.*, 1993).

However, the most common fabrication method of metal fuels is injection casting of the alloy (Burkes *et al.*, 2009). In this process the alloy constituents are mixed and then heated in yttria-coated graphite crucibles to a temperature above the melting point (about 1,773 K for U–Pu–Zr alloy) under vacuum in an induction furnace. Next a quartz glass mold, coated with a zirconia-alcohol slurry, is lowered into the melt and a vacuum-injection casting process is used to force the molten alloy into the mold. The casting is then removed from the furnace, the mold is broken and the fuel cylinders are recovered. The cylinders are cut and sheared to the required dimensions. This process has been used to fabricate the U–Pu and U–Pu–Zr fuels for EBR-II in the USA. The product is a two-phase material, consisting of the α and β phases.

An important issue for the fabrication of metal fuel containing minor actinides is the loss of americium. Americium is a volatile metal that has an appreciable vapor pressure at the processing temperature of the metal fuel. The losses can be reduced by a rapid processing of the melts, minimizing the heating/melting/holding intervals (Sabau and Ohriner, 2008). Since this effect cannot be eliminated, the losses have to be accounted for in the fabrication procedure. Injection casting, which requires relatively long heating times, is thus not well suited. Arc melting in combination with gravity drop casting is better suited, and has been successfully used on laboratory scale, with good americium retention (Kurata *et al*., 1997; Keiser *et al*., 2008).

34.7.3 The FR metal fuel pin and fuel element

The fast reactor metal fuel pin design aims at allowing the fuel to swell and achieve an almost complete fission gas release. This proved to be the best practical solution to cope with the radiation effects, and has been realized by the following technical measures:

- The smear density of the fuel, defined as the effective density inside the fuel pin, was lowered to $<80\%$ of the theoretical density of the fuel, by allowing a larger pellet–cladding gap to accommodate swelling up to a value at which a network of open porosity was created to obtain complete fission gas release.
- The gap was filled with (liquid) sodium to compensate the temperature increase over the pellet–cladding gap. The liquid sodium also fills (part) of the open porosity of the fuel, thus increasing its thermal conductivity.
- The plenum volume of the pin was increased to allow the sodium level to rise and to accommodate the complete fission gas release.

34.7.4 In-reactor behavior of metal fuel

The in-reactor behavior of metal fuel has been described comprehensively by Hofman and Walters (1994). The early work on α-uranium revealed significant anisotropic radiation growth, which is defined as the change in the shape of the sample without significant increase in volume. This is due to the fact that α-U crystals elongate in the [010] direction and contract in the [100] direction, caused by the fact that the interstitials and vacancies created by fission form loops on {010} and the {110} planes as a result of the anisotropic thermal expansion induced by thermal spikes in displacement cascades (see Hofman and Walters, 1994 and references therein). Significant radiation-induced swelling of α-uranium was also observed. The cause was found to be twofold. Firstly, it is due to the accommodation of the fission products in the fuel matrix. As in other fuel forms, some fission products can dissolve in the fuel matrix, whereas the fission gases are barely soluble in the metal and collect in gas bubbles. This swelling is directly dependent on the burnup. Secondly, anisotropic growth will cause strain between grains in polycrystalline samples, leading to plastic defor-

mation of grain boundaries (tearing, cavitation). This form of swelling is temperature driven, being dominant in the temperature range 673–873 K, and is characterized by the formation of large irregular cavities at grain boundaries. Although these two processes are independent, fission gas will accumulate in the cavities, resulting in a lower compressibility (see Hofman and Walters (1994) for a more extensive description).

A large amount of the irradiation data for U–Pu fuels was generated in the fast breeder programme of the USA (Hofman and Walters, 1994). Uranium metal fuel has been used as driver fuel for the EBR-II reactor and more than 30,000 fuel pins have been irradiated up to a burnup of 8 at.%.

Under irradiation, the temperature gradient and burnup lead to the fuel constituent redistribution in the fuel (Hofman *et al*., 1996; Kim *et al*., 2006). The microstructure of irradiated (U,Pu,Zr) fuels exhibits three distinct concentric zones (Fig. 34.86):

1. The Zr-enriched central zone
2. The Zr-depleted and U-enriched intermediate zone
3. The slightly Zr-enriched zone on the outer periphery

In general the radial U distribution is opposite of that of Zr, whereas the plutonium distribution shows only a slight radial dependence. Also distinct

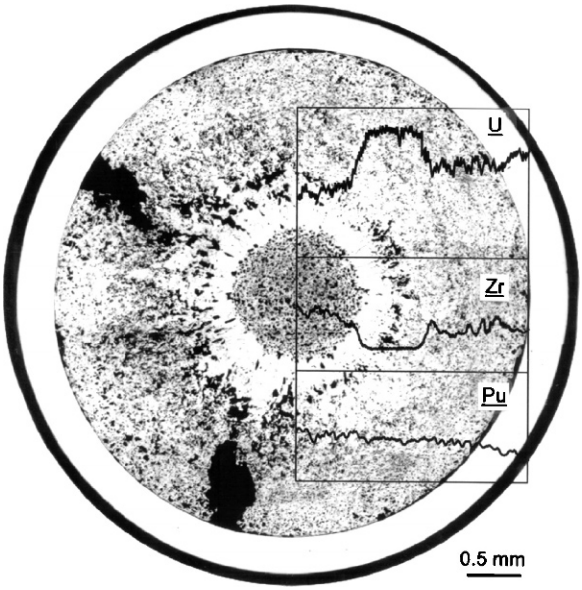

Fig. 34.86 *Optical micrograph of the irradiated U-Pu-Zr fuel and electron probe microanalysis* (*EPMA*) *scans for the major constituents* (*Kim et al.*, 2006). (©*Elsevier*, 2006, *reprinted with permission*).

differences in porosity occur between the zones. It has been suggested that this microstructure is caused by migration of Zr atoms due to the radial temperature gradient in the fuel, encompassing a multi-phase regime in which each phase field has different thermochemical properties (Kim *et al*., 2006).

The liquefaction temperature by eutectic formation between U–Pu–Zr fuel and stainless steel cladding is expected to occur above 873 K. The phase diagrams of the U–Pu–Zr–Fe system were assessed by Kurata (1999) using both thermodynamic calculations and experiments. Metallography of diffusion tests indicated that no liquid phase is formed at 923 K with a Pu content less than 25 wt% in U–Pu fuel.

The influence of minor actinides on metal fuel behavior was reported in a few studies only. Meyer *et al*. (2009) reported the results of an experimental irradiation of U–Pu–Zr metal fuel pins containing 1.2 wt% Am and 1.3 wt% Np. The limited postirradiation examination results indicated that the addition of the minor actinides did not alter the behavior of metallic U–Pu–Zr fuel, including the fuel cladding chemical interaction. The results indicate that americium migration has occurred along with the migration of uranium and zirconium, but local radial redistribution of americium to the cladding inner wall did not occur. However the possibility of condensation of americium in the plenum region above the fuel column could not be excluded. Ohta *et al*. (2009) reported the results of the irradiation of the U–Pu–Zr metal fuel containing 5% minor actinides as well as 5% rare-earths (to simulate fission product impurities) up to about 7 at.% burnup. Non-destructive analysis confirmed the fuel integrity and fuel behavior simulation predicted that no significant volatilization of Am occurred, though this needs to be confirmed by destructive analysis. Keiser, Jr. *et al*. (2008) reported the results of the irradiation of (U,Pu,Am,Np,Zr) and (Pu, Am,Np,Zr) alloys to a burnup of 4–8 at.% indicating similar irradiation behavior as (U–Pu–Zr) alloys.

34.8 OTHER FUEL FORMS

34.8.1 Coated particle fuels

The fuel for high temperature gas cooled reactors is made of graphite elements (hexagonal blocks or spherical compacts) containing many small 500 μm particles coated with several protective layers. The coatings act as barrier against fission gas release, forming a miniature pressure vessel, allowing the fuel to operate at high temperature.

The concept of coated particles was developed in the 1950s, in Europe and USA. Originally the so-called BISO particles (bistructural isotropic) were developed. These are kernels with a two-layer coating, the inner made of porous carbon to serve as buffer for fission gases and to accommodate geometrical deformation of the kernel, and the outer of dense pyrolytic carbon (PyC) that

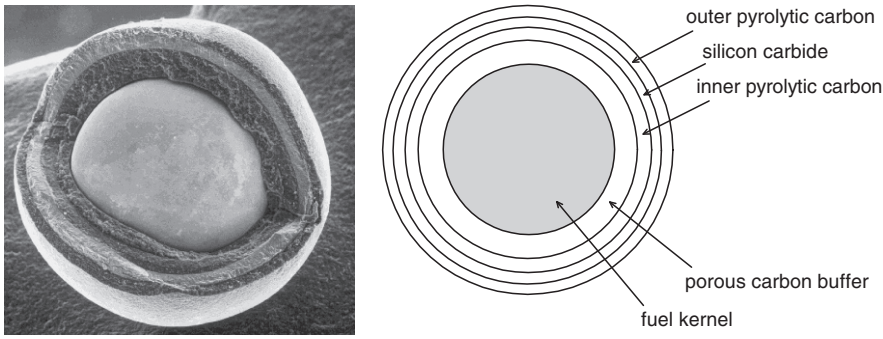

Fig. 34.87 *A TRISO coated particle* (©*Forschungszentrum Jülich*, *reproduced with permission*).

serves as a mechanical protection of the particle. Later the so-called TRISO (tristructural isotropic) particles were introduced, which are four-layer coated with an interlayer of SiC between two layers of high-density isotropic PyC (Fig. 34.87). The role of the SiC layer is to improve the sealing of the particles against fission product release, as it acts as a barrier even at temperatures far above the operational limit. The outer PyC layer acts as a protection of the SiC seal. Most of the reactor concepts employing coated particle fuel now use the TRISO concept, with a kernel of 500–600 μm, a porous carbon layer of 90–100 μm, inner and outer PyC layers of 40 μm and a SiC layer of 35 μm.

The fabrication of the oxide kernel is normally achieved by gel-supported precipitation (Petti *et al.*, 2003). This is an aqueous process in which the uranium (and/or other actinides) are dissolved in nitric acid, together with additives (polyvinyl alcohol, tetrahydrofuryl alcohol) to obtain a viscous solution required for the gel formation (Fig. 34.88). This solution is then pumped through a vibrating nozzle that produces droplets that fall in an ammonium bath in which gelation/solidification of the droplets occurs to give spherical particles. After ageing, washing (with isopropyl alcohol and water) and drying, the microspheres are calcined. Next the microspheres are sintered in Ar/H_2 to obtain UO_2 kernels of high density (close to theoretical). By sieving and sorting only those particles that meet the specifications are selected for further processing. With this process ThO_2, PuO_2 and mixed oxide fuel kernels can also be produced. It is also suited for the fabrication of UCO kernels. Carbon black is added to the starting solution and the sintering is performed using CO to ensure adequate C/O stoichiometry in the UCO kernel (Petti *et al.*, 2003).

The coatings are deposited on the kernels in a fluidized bed reactor. In a flow of argon gas the kernels are inserted into a furnace, in which the layers are subsequently produced from different precursor gas feeds by chemical vapor deposition in the temperature range 1,500–1,673 K (Fig. 34.88).

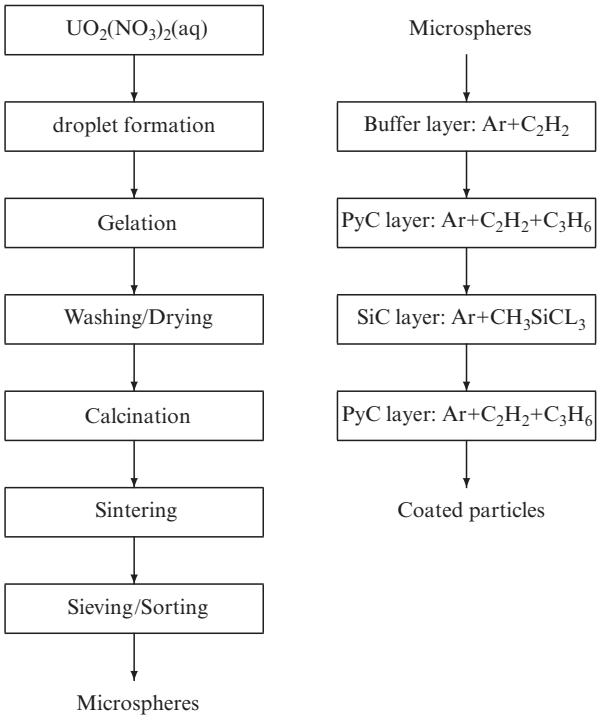

Fig. 34.88 *Schematic representation of coated particles. Left: the gel-supported kernel fabrication*; *right: the coating deposition*.

High-temperature gas-cooled reactor fuel elements are made by mixing the coated particles with a matrix graphite powder, made of different kinds of graphite and a resin. First the coated particles are overcoated with the matrix powder, next they are dosed into the matrix powder, which is then compacted and which is then carbonized and annealed (2,273 K). In Europe the compact is a spherical fuel elements (pebble) of about 6 cm. In this case a ''non-fuel'' zone is added to the outside of the compact, which after carbonization and annealing is machined to the right dimensions. Spherical compacts permit a continuous refuelling of the core. In the USA the cylindrical compacts (rodlets) are loaded into hexagonal graphite blocks that form the building blocks (elements) of the reactor core (Fig. 34.89).

Due to the good thermal conductivity of the graphite the fuel temperature in the coated particles is moderate. It is dependent on the helium coolant temperature, which enters the core at a temperature of 523–723 K and leaves the core at a temperature between 823 and 1,223 K, depending on the power density of the reactor design. At this temperature the fuel particle will keep its integrity and retain the fission gas (Fig. 34.90). However, occasionally particle failure occurs,

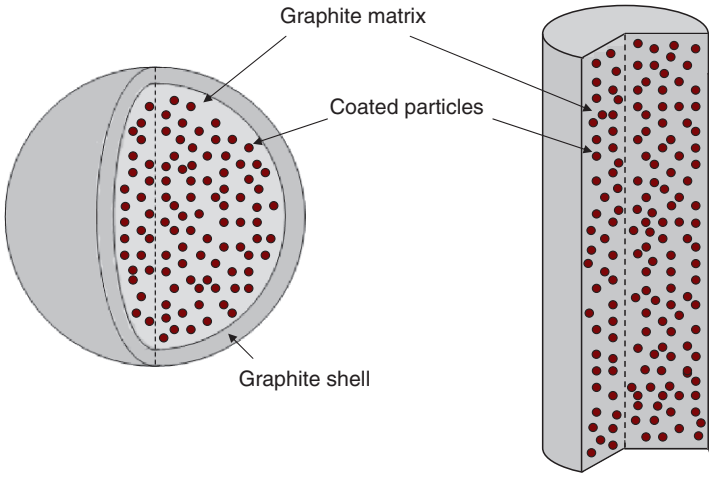

Fig. 34.89 *Schematic representations* (*not to scale*) *of the spherical* (*left*) *and cylindrical* (*right*) *high-temperature gas-cooled reactor fuel elements*.

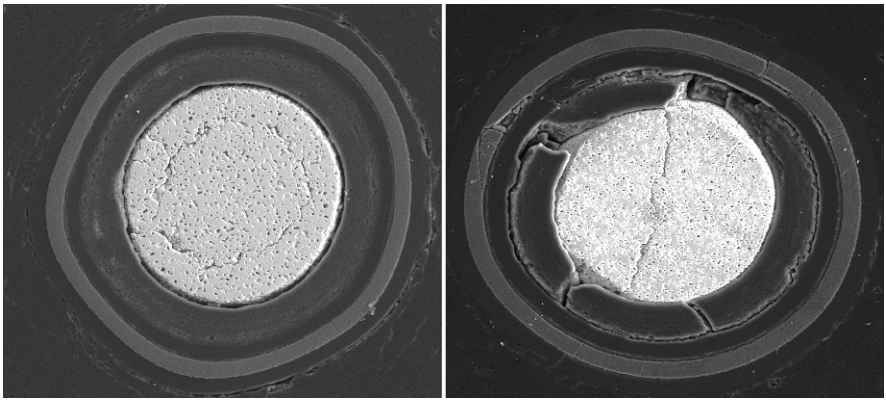

Fig. 34.90 *A ceramographic section of an intact* (*left*) *and a failed* (*right*) *irradiated TRISO coated particle* (*burnup* 9.7% *FIMA*) *after heating at* 1,800°*C* (*Freis et al*., 2008). (©*European Communities*, *reproduced with permission*).

leading to fission gas release. The following mechanisms may result in particle failure (Petti *et al*., 2003):

- Pressure vessel failure caused by internal gas pressure
- Pyrocarbon layer cracking and/or detachment due to irradiation-induced shrinkage which ultimately leads to the failure of the SiC layer

- Fuel kernel migration (amoeba effect), which leads to interactions with the coating layers, which is mainly an issue in block type cores
- Fission product/coating layer chemical interactions
- Matrix/outer PyC interaction
- As-manufactured defects produced during fabrication of fuel particles or during pressing of fuel compacts/spheres
- Thermal decomposition of the SiC layer at very high temperatures
- Enhanced SiC permeability and/or SiC degradation (especially for Ag)

Some of these mechanisms will be explained below.

During irradiation, coated particle fuel is subjected to a considerable overpressure due to gas generation. Fission gases are released from the kernel to the porous buffer layer and as a result tensile forces are generated in the inner Pyrocarbon and SiC layers. In addition to fission gas, there is excess oxygen released during fission. This excess oxygen reacts with the buffer to form CO gas. Both fission gas release and CO formation are a function of burnup and temperature.

The U–C–O phase diagram is shown in Fig. 34.91. $UO_{2\pm x}$ and carbon are in equilibrium:

$$[O]_{sln\ in\ UO_{2\pm x}} + C(cr) = CO(g) \tag{34.58}$$

The CO equilibrium pressures above $UO_{2\pm x}$ and C can reach very high values depending on the O/U ratio of the uranium dioxide. This is related to the sharp increase of the oxygen potential in $UO_{2\pm x}$ with the O/U ratio.

Low CO pressures of the order of 10^{-2}–10^{-6} bar are obtained for hypostoichiometric uranium dioxide (O/U < 2) whereas values up to 10^{4} bar are calculated for hyperstoichiometric oxide with O/U = 2.01 assuming thermody-

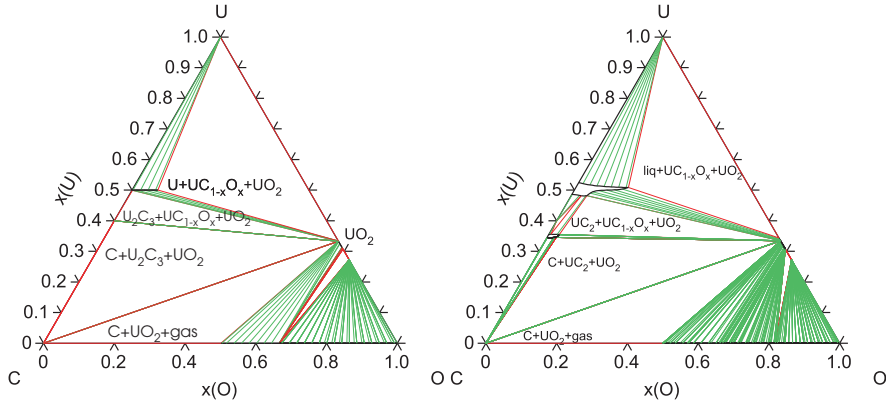

Fig. 34.91 *Assessed U–C–O phase diagram at* 1,273 *and* 1,973 *K.* (*After Guéneau et al.*, 2006).

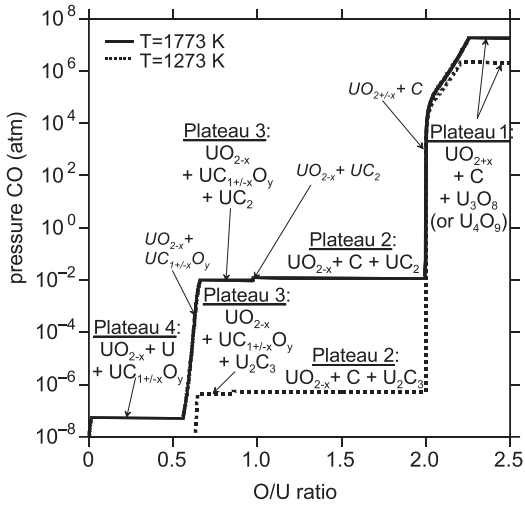

Fig. 34.92 *Variation of equilibrium CO pressure along the U–CO composition line* (*C/O* = 1) *at* 1,273 *and* 1,773 *K.* (*After Guéneau et al*., 2006).

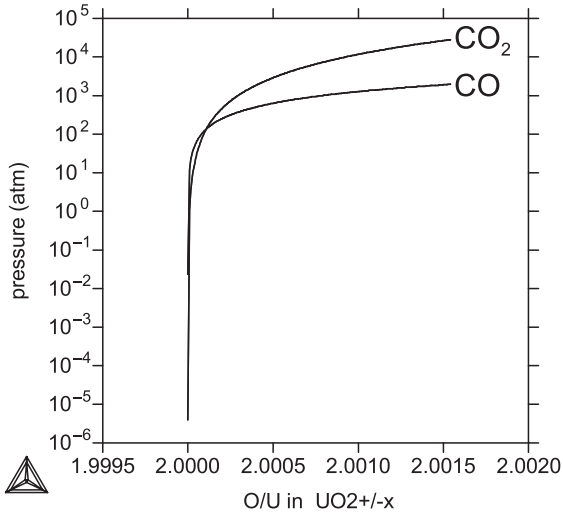

Fig. 34.93 *Calculated CO and* CO_2 *partial pressures versus O/U ratio in* $UO_{2\pm x}$ *fuel in equilibrium with carbon at* 1,273 *K and at a fixed volume of* 7.18×10^{-6} m^3 (*free volume of the buffer*). (*After Guéneau et al*., 2006).

namic equilibrium (Figs. 34.92 and 34.93). Kinetic factors related to the complex mechanisms involved in the reaction may lead to lower pressures that may explain the low number of failed particles due to overpressure in the irradiations tests. Nevertheless it is important to design the particles with a large enough

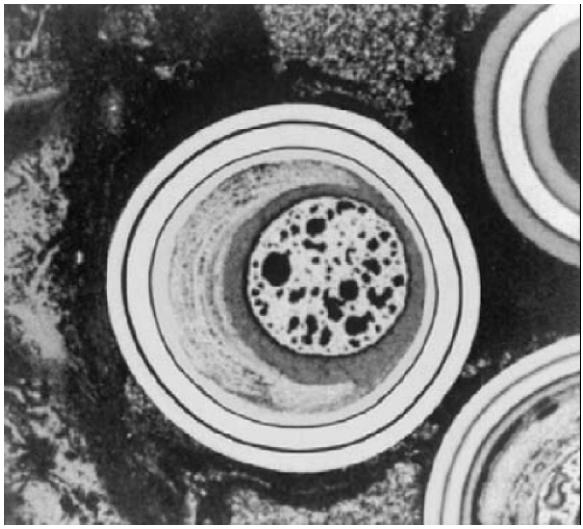

Fig. 34.94 *Kernel migration in a TRISO particle* (*Petti et al.*, 2003). (©*Elsevier*, 2003, *reprinted with permission*).

buffer volume to ensure that under nominal conditions particles do not fail by overpressure.

To avoid the overpressure in the particle due to the interaction between free oxygen and carbon, an advanced ''UCO'' fuel made of a mixture of UO_2 and UC_2 was developed in the USA. In fact, in the three phase region [UO_2 + UC_2 + C], the equilibrium pressure of CO is low (10^{-6}–10^{-2} bar for 1,273< T <1,773 K) and only depends on the temperature.

Kernel migration, also called ''amoeba'' effect, is associated with carbon transport in the particle when a local temperature gradient is present (Fig. 34.94). In fact, when the temperature is different on each side of the particle, the CO equilibrium pressures are different and lead to mass transport of carbon down the temperature gradient. If the migration is excessive, the kernel will penetrate the TRISO coating leading to particle failure. The use of ''UCO'' fuel minimizes this problem as the CO pressures are maintained at low levels.

Irradiation experiments have demonstrated that some fission products are transported from the kernel to the inner surface of the SiC where they interact, possibly leading to failure of the SiC layer. The temperature and the temperature gradient over the particle are of course key parameters for these processes, as is the burnup (i.e. concentration of fission products). One of the critical elements is palladium, which is important for both UO_2 and UCO particles. In UO_2 fuel particles palladium is found in Mo–Tc–Ru–Rh–Pd and Pd–Te precipitates, but also at the inner surface of the SiC layers (Minato *et al.*, 1990, 1994). On the cold side of the particles reactions with the SiC layers were

observed. The SiC layer is corroded locally and secondary phases, mainly consisting of silicon and palladium, are seen both in the SiC layer and at the interface of the inner PyC and the SiC layers. It was proposed that the reaction

$$2Pd(cr) + SiC(cr) = Pd_2Si(cr) + C(cr) \tag{34.59}$$

occurs (Minato *et al*., 1990). Silver was found to migrate through apparently intact particles and it is released into the reactor coolant system where it deposits on cold surfaces. The mechanism is thought to be diffusive transport (Schenk *et al*., 1990). Other volatile fission products such as Cs and Te have been detected in the buffer PyC layer (Minato *et al*., 1994). Schenk *et al*. (1990) suggested that cesium release is initiated upon failure of the silicon carbide layer, likely by fission product enhanced local changes of the SiC structure. After SiC failure, cesium release is controlled by a SiC grain boundary diffusion. It has been suggested (Minato *et al*., 1994) that Cs reacts with the carbon to form intercalation phases such as CsC_n (e.g. CsC_{60}), which are thermodynamically stable at high temperature and low oxygen potential.

High temperature heating tests at 1,873 K, a typical temperature for simulating loss of coolant flow and pressure loss accidents in high temperature reactors, have shown that no additional release of safety-relevant fission products occurs compared to normal operation, and that the particle failure remains very low (Schenk *et al*., 1990). Test at higher temperature have demonstrated that the SiC layer undergoes thermal decomposition above 2,273 K (Nabielek *et al*., 1989). This phenomenon is controlled by thermodynamics and kinetics, i.e. temperature and time. Zirconium carbide (ZrC) is considered as an interesting alternative for the sealing layer of TRISO particles. The melting point of ZrC is very high (3813 K) and it forms a eutectic liquid with carbon at 3,123 K (Minato *et al*., 1997). Irradiation studies of ZrC coated particles under normal and accidental conditions have shown good results (Reynolds *et al*., 1976; Minato *et al*., 1997). In addition, zirconium carbide shows a good resistance to chemical attack by the fission product palladium and a good retention capability of cesium. However, its resistance against ruthenium is less.

34.8.2 Sphere-pac and Vipac fuel

Vibrocompacted fuels have been studied as an alternative to pellet-type fuel. In this process fuel particles are loaded in a cladding tube and compacted by vibration to obtain a close packed arrangement. In case the particles are spherical, one generally refers to *sphere-pac* fuel, in case the particles have a random shape, one refers to *vipac* fuel. As the fabrication process has a reduced number of steps, they are well suited for remote handling and thus for fast reactor fuel containing poorly decontaminated plutonium or minor actinide (Barth *et al*., 2007). The obvious disadvantage of this fuel type is the higher centerline fuel temperature as a result of the much poorer thermal transport in the sphere pac, compared to pellet-type fuel.

Spherical particles for *sphere-pac* fuel can be prepared by sol-gel technology, as described in the previous section. This technique has been successfully used for the fabrication of oxide, carbide and nitride fuels. The *sphere-pac* concept is based on the packing of particles of two or three size fractions to obtain an optimum smear density of the fuel pin. Generally the larger fraction is filled first, and the smaller are then "infiltrated" to fill the interstitial space within the coarse packing. For example, with particles of 800 and 70 μm a packing fraction (or smear density) of around 80% can be obtained, when vibration conditions (acceleration, frequency, amplitude and time) are optimized (Barth *et al.*, 2007). The theoretical packing fraction (P_f) can be obtained from the relations between the pin diameter (D), and the sphere diameter (d_i) as derived by Ayer and Soppet (1965). For a bi-modal sphere packing the relation is

$$P_f = 0.867 - 0.079e^{-0.313D/d_1} - 0.269e^{-0.201d_1/d_2} - 0.159e^{-0.313D/d_1 - 0.201d_1/d_2} \tag{34.60}$$

and for a tri-modal sphere packing

$$\begin{aligned} P_f = {} & 0.951 - 0.029e^{-0.313D/d_1} - 0.098(e^{-0.201d_1/d_2} + e^{-0.201d_2/d_3}) \\ & - 0.198e^{-0.201(d_1/d_2 + d_2/d_3} \end{aligned} \tag{34.61}$$

The thermal conductivity of a sphere-pac fuel is determined by the following factors:

- The thermal conductivity of the spheres
- The effect of the thermal conductivity of the filling gas
- The sintering together of the large spheres (necking)
- The restructuring of the sphere pac fuel

The sintering effect plays a major role (Ades and Peddicord, 1982). The as-fabricated spheres that have a small contact area, start to restructure by a process known as necking (Fig. 34.95). Below 1,373 K the neck growth is dominated by irradiation creep. Between 1,373 and 1,673 K the necking is caused by grain boundary diffusion and linear thermal creep, and it accelerates above 1,673 K, leading to significant restructuring of the central region of a sphere-pac fuel (Fig. 34.96), similar to fast reactor oxide fuel operating at high centerline temperature. Columnar grains are formed with typical lenticular pores, due to vaporisation/condensation processes (Fig. 34.97).

Irradiation experiments with various types of *sphere-pac* fuel have been performed. The restructuring of the fuel starts early after the beginning of the irradiation and complete restructuring has been observed after 12 h. Van der Linde and Verheugen (1982) reported the results of UO_2 and $(U,Pu)O_2$ *sphere-pac* fuel irradiated in the HFR (Netherlands). The post-irradiation examinations revealed that sintering and necking of the spheres at the positions where they touch is an important factor affecting their behavior. Barth *et al.* (2007) reported the results of short irradiation experiments of $(U_{0.8}Pu_{0.2})O_2$ and

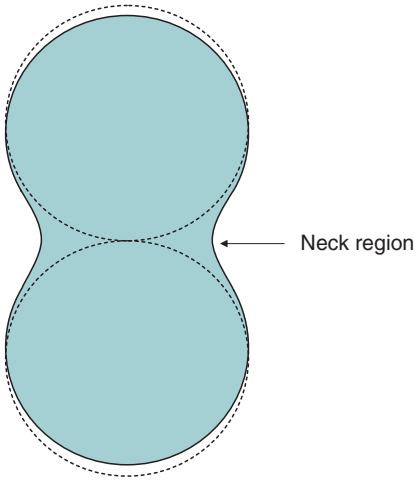

Fig. 34.95 *A schematic representation of sintering of two spheres. The dotted lines indicate the as-fabricated spheres, the solid lines necking process occurring irradiation and leading to densification.*

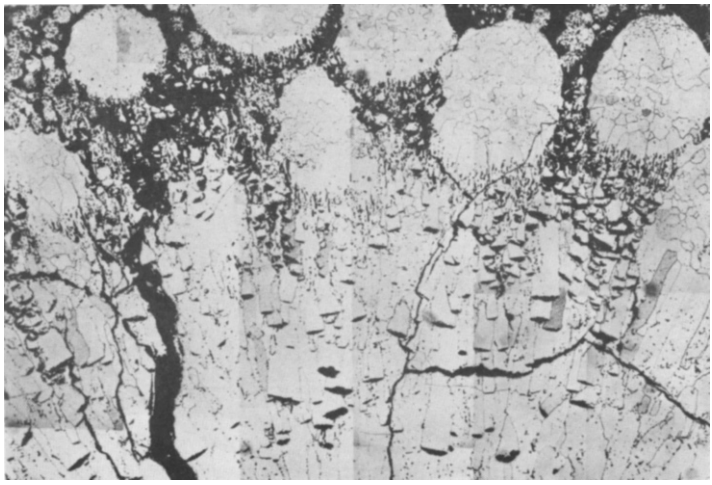

Fig. 34.96 *Columnar grain and lenticular pores, as well as dendrite type deposition on the spheres in an irradiated sphere pac fuel.* (©*European Communities, reproduced with permission*).

$(U_{0.75}Pu_{0.20}Np_{0.05})O_2$ *sphere-pac* fuels. These tests showed that the fuel restructuring starts immediately and leads to densification to a pellet-like body, and the formation of a central void for a linear rating of 64.8 kW/m. Mason *et al*. (1992) reported the results of (U,Pu)C mixed carbide irradiation tests in the Fast

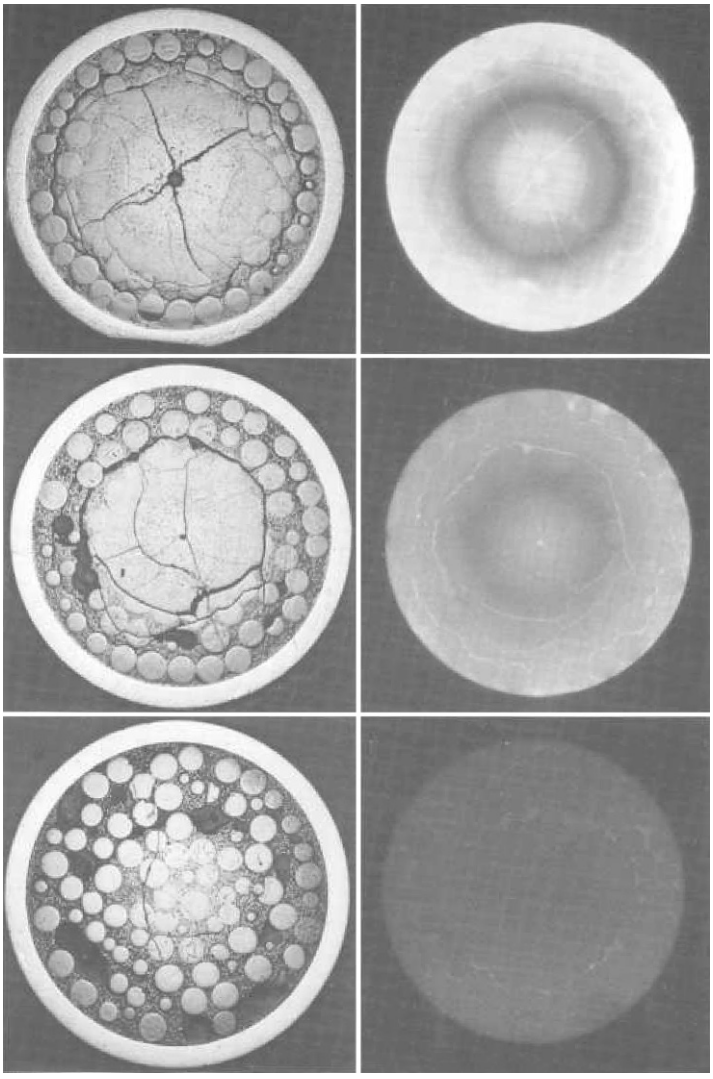

Fig. 34.97 *Ceramographs (left) and (γ, β)-autoradiographs (right) of UO_2 sphere-pac fuel. The maximum linear power (kW/m) and burnup (MWd/kgU) were* 28/30 (*bottom*), 42/44 (*middle*) *and* 61/52 (*top*) (*Van der Linde and Verheugen*, 1982). (©*NRG, reproduced with permission*).

Flux Test Facility (USA) showing that restructuring also occurs in that fuel but develops more slowly. After 620 full power days at a linear rating of 69.9 kW/m the densification only proceeded from the center to about half the radius of the pellet and the onset of a central void could be observed.

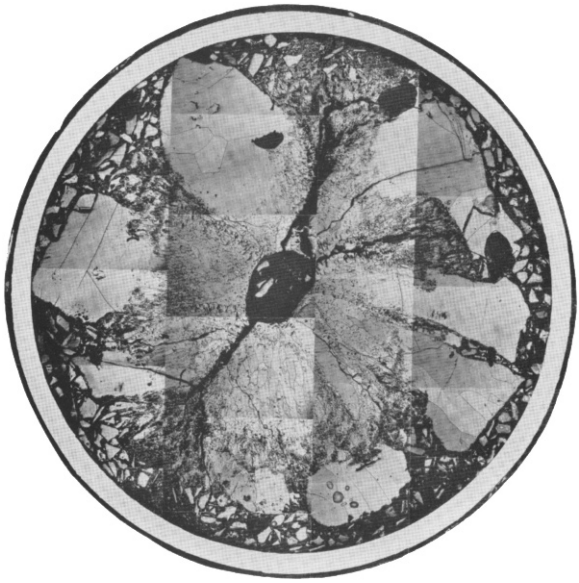

Fig. 34.98 *Restructuring of vipac fuel made of granulates.* (©*European Communities, reproduced with permission*).

Proposals have been made to use a material with a good thermal conductivity (Mo, MgO, SiC) for the smallest-fraction spheres of a three fraction mixture to improve the overall conductivity of the sphere-pac (Van der Linde, 1991) but were never tested.

Early tests of *vipac* fuel used granules produced in various ways such as sintering and crushing, fusion, electrodeposition, pneumatically impaction, or sol-gel (Freshley, 1972). Due to the low smear fuel density of about 80% and the concomitant high centerline fuel temperature, these granulates sinter during irradiation to a dense material with the same restructuring typical for *sphere-pac* fuels (Fig. 34.98). In Russia *vipac* fuel has been employed for direct processing of $(U,Pu)O_2$ mixed oxide obtained from electrochemical reprocessing of LWR fuel (Bychkov *et al*., 2002). With this process a polydisperse granulate is obtained that is filled directly into the fuel pin and subsequently compacted by vibration. In the Russian process the addition of a small amount of metallic uranium powder increased the smear uranium density to about 85% of that of the UO_2. This uranium metal acts also as a oxygen getter to control the oxygen potential (Mayorshin *et al*., 2000). Mixed oxide fuel pins for the BOR60 reactor in Russia have been fabricated by this process. It was found that the presence of uranium powder reduced the release of cesium due to the lower oxygen potential. Gratchyov *et al*. (2007) reported the results of the irradiation of $(U,Pu)O_2$ *vipac* fuel produced from weapons-grade plutonium in the BN600 fast reactor

(Russia) and Bychkov *et al*. (2002) reported results from an irradiation experiment of (U,Pu,Np)O_2 *vipac* fuel produced by this process. The post-irradiation examinations of these experiments showed the typical fast-reactor oxide fuel restructuring and no anomalies.

34.8.3 Molten-salt fuels

In a molten salt reactor the fissionable material is dissolved in an inorganic liquid that circulates at a low pressure through the reactor vessel and the primary circuit, including the heat exchanger. Also the secondary coolant transferring the heat to the steam generator is generally a molten salt.

The molten salt technology was originally developed at Oak Ridge National Laboratory (ORNL) in the USA. That work started in the 1940s with the concept for aircraft propulsion (MacPherson, 1985) and the Aircraft Reactor Experiment (ARE), critical during several days in 1954, was the first demonstration of the feasibility of the molten salt technology. In ARE a mixture of NaF–ZrF_4 was used as carrier of the fissile UF_4.

In the second half of the 1950s the molten salt technology was transferred to the civilian nuclear programme of the USA. It was recognised that the molten salt reactor would be ideal for thermal breeding of uranium from thorium (MacPherson, 1985) and the Molten Salt Reactor Experiment (MSRE) was started at ORNL to demonstrate the operability of molten-salt reactors. MSRE was a graphite-moderated reactor of 8 MWth that operated from 1965 to 1969. ^{7}LiF–BeF_2 (FLIBE), with 5% ZrF_4 as oxygen getter, was selected as fuel carrier because of the very low neutron-capture cross sections of ^{7}Li and Be. Three different fissile sources were used: $^{235}UF_4$, $^{233}UF_4$ and $^{239}PuF_3$. LiF-BeF_2 was used as coolant in the secondary circuit. The results of MSRE, which have been reported in great detail (Grimes and Cuneo, 1960; Grimes, 1970; Haubenreich and Engel, 1970), revealed that the selected materials (fuel, structurals) all behaved well and that the equipment behaved reliably. In that respect the experiment was very successful. The MSRE was followed by the design of the Molten Salt Breeder Reactor (MSBR) in which ^{7}LiF–BeF_2 was selected as carrier for the fertile ThF_4 and the fissile UF_4. Because for this reactor a permanent clean-up was foreseen, the ZrF_4 oxygen getter could be omitted.

Molten salt reactors are still being studied and three different concepts are investigated nowadays: the moderated thorium reactor, based on the MSBR design, the non-moderated thorium reactor, and the actinide burner. Due to the different requirements, the fuel compositions of the latter two are different from the original MSBR concept, as will be discussed below.[7] LiF–BeF_2 solvent proposed for the graphite moderated thorium-based breeder has very good physico-chemical properties as fuel matrix. The 66:34 composition has a low melting point (732 K), as shown in Fig. 34.99, which is only slightly increased when ThF_4 is added. The solubility of ThF_4 in the liquid phase is high. Beneš and Konings (2008) showed by thermochemical modeling that the solubility of

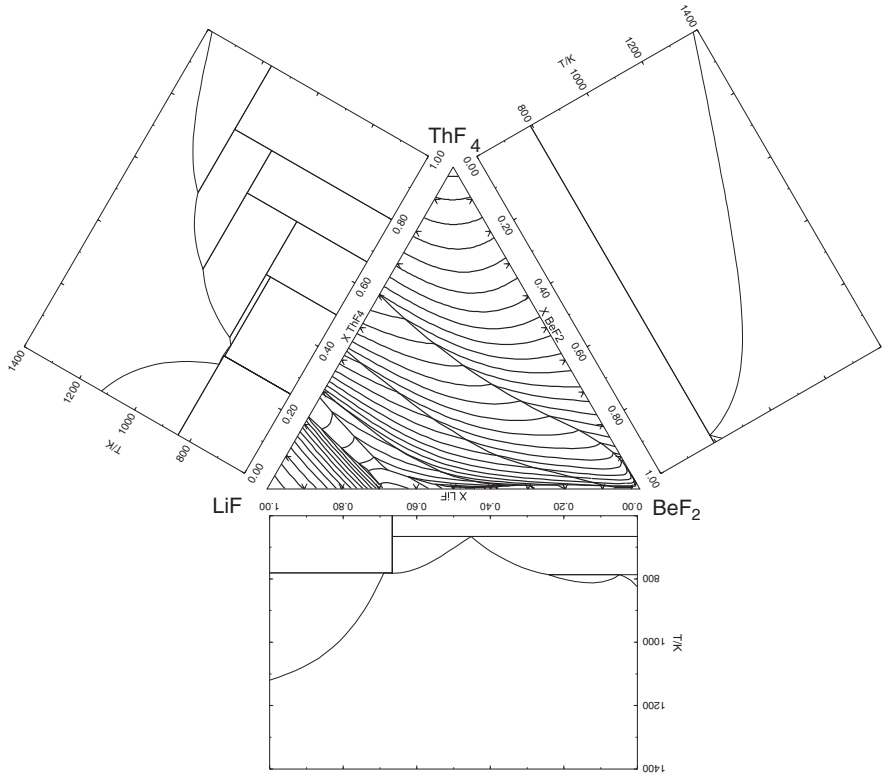

Fig. 34.99 *The projection of the liquidus surface of LiF–BeF_2–ThF_4. Isotherms with an interval of 25 K are shown. The three binary subsystems are along the sides.* (*After van der Meer and Konings*, 2006)

ThF_4 in the LiF–BeF_2 matrix for T = 839 K (inlet temperature of MSBR) and LiF/BeF_2 = 0.818/0.182 (the fuel composition proposed in MSBR) is between 9.2 and 20.8 mol%. The proposed fuel composition in the LiF–BeF_2–AnF_4 system of the MSBR was chosen well within this window: 71.7–16.0–12.3 mol%, where the AnF_4 fraction was 12.0 mol% ThF_4 and 0.3 mol% for UF_4. The relevant physico-chemical properties of this salt, such as density, viscosity, heat capacity or thermal conductivity, have been studied in some detail, and the recommended values are given in Table 34.12.

The concept for the non-moderated thorium molten salt reactor is based on the use of only[7] LiF as solvent, resulting in the ^{7}LiF–ThF_4–UF_4 mixture as fuel (Mathieu *et al*., 2006; Merle-Lucotte *et al*., 2008). As shown in Fig. 34.100, the solubility of ThF_4 in liquid LiF at T = 903 K (inlet temperature of the Thorium Molten Salt Reactor) is between 20.0 and 32.3 mol%, and the LiF–AnF_4 (78–22 mol%) composition has been proposed. In this concept AnF_4 is

Table 34.12 *Selected properties of fuel salts.* (*After Beneš and Konings*, 2008).

Property	*LiF–ThF$_4$*	*LiF–BeF$_2$–ThF$_4$*
	0.78–0.22	0.717–0.16–0.123
Melting point/K	841	771
ρ/kg·m^{-3}	5543.0–1.2500 (T/K)	4124.3–0.8690 (T/K)
η/ mPa s	0.365exp(2,735/(T/K))	0.062exp(4,636/(T/K))
C_p/J·K^{-1}·g^{-1}	1.00	1.23
λ/W·m^{-1}·K^{-1}	~1.5	1.5
log$_{10}$(p/Pa)	11.902–12989/(T/K)	11.158–10,790.5/(T/K)

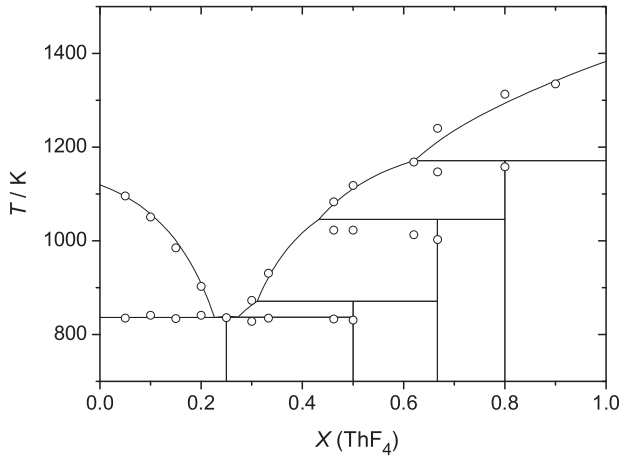

Fig. 34.100 *The assessed LiF–ThF$_4$ phase diagram.* (*After van der Meer and Konings*, 2006)

represented mainly by ThF_4 which serves as a fertile material to breed ^{233}U and by UF_4 which is the fissile material, normally up to 4 mol%. The recommended values for the relevant physico-chemical properties of this salt are also given in Table 34.12.

For the molten salt actinide burner the actinide solubility is a key parameter. The solubility of PuF_3 in LiF–BeF_2 is low (<1 mol%) and it has been demonstrated that replacement of BeF_2 by NaF increases the solubility (Barton, 1959). Therefore ^{7}LiF–NaF–BeF_2 has been proposed as a solvent for PuF_3 (Ignatiev *et al.*, 2002) as transmutation fuel. This system has not been studied in great detail. A phase diagram for the LiF–NaF–BeF_2–PuF_3 system for 1.3 mol% PuF_3 has been proposed by Beneš and Konings (2009), as shown in Fig. 34.101. The lowest pseudoternary eutectic has been calculated to be at T = 775 K for x(LiF) = 0.203 and x(NaF) = 0.571, x(BeF_2) = 0.212, and x(PuF_3) = 0.013. This

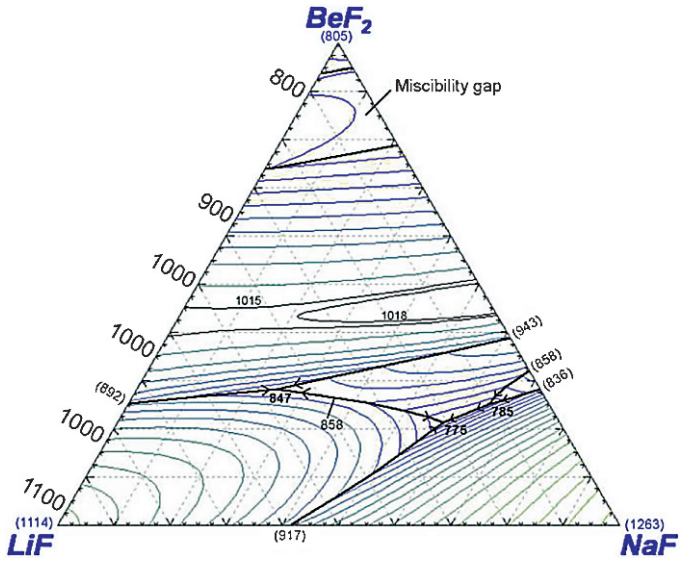

Fig. 34.101 *The pseudo-ternary LiF–NaF–BeF_2 section of the LiF–NaF–BeF_2–PuF_3 phase diagram for* 1.3 *mol% PuF_3.* (*After Beneš and Konings*, 2009).

temperature is well below the inlet temperature of the MSR burner concepts. Physico-chemical properties of this fuel salt are poorly known.

34.8.4 Inert matrix fuels

The term *Inert Matrix Fuel* (IMF) is generally used for plutonium fuel that does not contain uranium as a component of the fuel matrix but instead a material that is highly transparent for neutrons, thus not activating during in-reactor irradiation. The concept of inert matrix fuel has been proposed for the destruction of excess plutonium (separated civil or from dismantled weapons) in a single irradiation campaign. A variety of materials has been proposed, but nowadays IMF focusses on zirconia-based materials, and in this section we will restrict ourselves to this fuel type.

Ledergerber *et al*. (2001) have developed ytrrium-stabilized zirconium based IMF for the utilization of separated plutonium. The fuel also contained Er as burnable poison for reactivity control. They studied two different fabrication processes: a dry process (powder mixing) using multi-stage attrition milling and a wet process based on coprecipitation from nitrate solutions using the internal gelation process. Hellwig *et al*. (2005) described the fabrication of this IMF for irradiation tests in the Halden reactor. IMF pellets with composition $(Zr_{0.74}Y_{0.14}Er_{0.04}Pu_{0.08})O_2$ were fabricated using both processes. In the dry process the powders were milled 15 times in an attrition mill, then sintered at

1,723 K in an oxidative atmosphere (CO_2). In the wet process the powders were coprecipitated from solutions, then crushed and also milled 15 times in the attrition mill, sintered at 1,923 K in a reducing atmosphere (N_2 + 8%H_2).

The major disadvantage of zirconia-based fuel material is the low thermal conductivity. Measurements of the thermal conductivity λ of this material yielded the following expression (Hellwig and Kasemeyer, 2003):

$$\lambda = \frac{1}{0.403 + 0.00013(T/K)} + 1.1 \times 10^{11}(T/K)^3 \qquad (34.62)$$

Irradiation tests of zirconia-based IMF in the Halden reactor showed that (Hellwig *et al.*, 2005, 2006):

- The observed fuel temperatures are significantly higher than in standard UO_2 for the same linear heating rate, in line with expectations, because the thermal conductivity of the zirconia-based IMF is significantly lower than that of UO_2
- A substantial densification took place at beginning of irradiation, evident from the decrease of rod inner pressure and decrease in fuel column length.
- At later stages of the irradiation, an increase of the rod inner pressure during high power periods indicated fission gas release comparable to that expected for UO_2 fuel at these (high) fuel temperatures.
- Significant grain growth in the inner part of the fuel.

Improvement of the thermal conductivity by mixing the Zr-based material with a ceramic or metallic material has been investigated by several groups. A dual MgO–ZrO_2 fuel for use in LWRs has been proposed by Medvedev *et al.* (2005), who suggest that magnesia will bring high thermal conductivity while zirconia will provide protection from the LWR coolant attack.

34.8.5 Transmutation targets

Transmutation of long-lived radionuclides is a potential technology for the treatment of spent fuel from the nuclear fuel cycle. In the transmutation process the long-lived radionuclides are transformed by nuclear reactions into short-lived or stable nuclides. This can be achieved by a neutron capture reaction or by neutron capture followed by fission, normally in nuclear reactors. The former process is generally used for the transmutation of fission products, the latter for (transuranium) actinides. Transmutation technology is complementary to the reprocessing and re-use of plutonium from spent fuel. It implies, however, that further extraction steps are implemented in the fuel reprocessing to separate also other long-lived radionuclides such as the minor actinides Np, Am and Cm from the spent fuel. These extraction steps are often called *partitioning* and therefore the term Partitioning and Transmutation (P&T) is generally used for this recycling concept.

The radioactive characteristics of the relevant americium and curium isotopes are quite different from those of uranium and plutonium. As discussed in Section 34.5.2 (d) the high(er) γ and neutron dose rates have to be taken into account for these elements, as well as the decay power (particularly ^{244}Cm), as a result of which the fabrication is significantly more complicated, and can only be done in shielded cells.

In contrast to minor actinide fuels that are intended for energy production, the studies of transmutation targets have focused from the beginning on uranium-free concepts to optimise the transmutation efficiency. Two types of targets have been considered: composite and solid solution targets.

In composite (dispersion) targets the main phase generally serves as the neutronically inert matrix and the dispersed phase contains the fissile material. The fission process takes place in the dispersed phase and the effects of the irradiation (fission product recoil, alpha radiation of transmutation products) will be concentrated in and immediately around that phase. The fraction of the matrix subjected to radiation damage is dependent on the size and volume fraction of the dispersed phase (Chauvin *et al*., 1999), as shown in Fig. 34.102.

By choosing the right combination of phases, the properties of the composite material can be tailored for the specific irradiation conditions (Chauvin *et al*., 1999). For example by choosing a good heat conducting material, the poor conductivity of the actinide phase can be compensated. When spherical particles are randomly distributed in a matrix, the overall thermal conductivity is given by the equation (Schulz, 1981):

$$(1 - C_D) = \frac{\lambda_D - \lambda_C}{\lambda_D - \lambda_M}(\lambda_M \lambda_C)^{\frac{1}{3}} \tag{34.63}$$

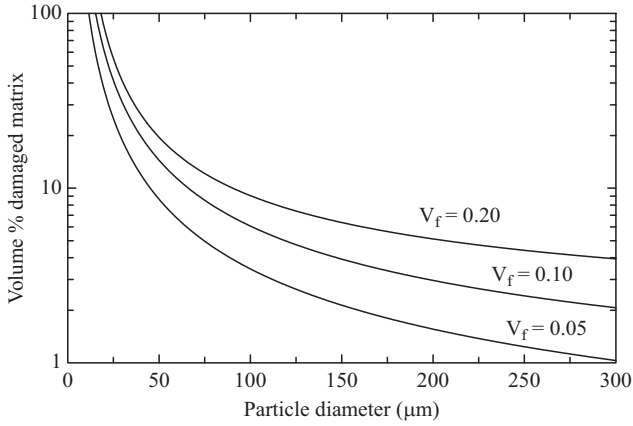

Fig. 34.102 *The volume of damaged matrix as a function of particle diameter for different volume fractions (V_f) of the dispersed phase.*

where λ_M, λ_D and λ_C represent the thermal conductivity of the matrix, dispersed phase and the composite, respectively, and C_D ($0 \leq C \leq 1$) represents the concentration of the dispersed phase. For non-spherical particles the situation becomes more complex and finite element modeling can help to obtain a reliable estimate of the thermal conductivity (Lutique *et al*., 2003).

In solid solution targets the actinides and the matrix form a homogeneous mixture of two or more solid phases that are distributed randomly/substitutionally on the same crystallographic lattice site. In a solid-solution the fission takes place homogeneously in the material, and the effects of the radiation are homogeneously distributed.

The composite studies have concentrated on matrices like MgO, Mo, or $MgAl_2O_4$. The latter has been studied extensively and although the results indicated that it has limited suitability as matrix material, the experience showed the complexity of the composite. For the dispersed phase the pure oxide phase is considered, but a solution of the actinide oxide(s) in yttria-stabilized zirconia (Croixmarie *et al*., 2003) has also been considered. Yttria-stabilized zirconia is also the main material considered for solid solution targets, thus closely resembling the IMF concept for plutonium destruction.

Transmutation targets can be fabricated using traditional powder blending techniques, but these have the disadvantage that they produce radioactive dust that will accumulate in the glove boxes, which is unwanted when working with americium or curium, as discussed in Section 34.5.2 (d). Therefore liquid processes have been studied extensively. An innovative method was developed by Fernández *et al*. (Richter *et al*., 1997; Fernández *et al*., 2002), based on infiltration of an actinide nitrate solution into either a porous ceramic body or a powder with a particle size large enough to be free flowing and not producing dust. After the infiltration is completed the precipitate that filled the open porosity in the material, is decomposed by thermal treatment, eventually followed by further infiltration steps. The infiltrated pellet can be sintered into a dense pellet; the infiltrated powder can be pressed into a pellet and then sintered.

In the EFTTRA-T4 experiment a $MgAl_2O_4$–AmO_2 target, produced by the infiltration method yielding a microdispersed distribution of the actinide phase, was irradiated in the HFR (Netherlands) during 358 full power days. At the end of the irradiation 96% of the initial ^{241}Am was transmuted, and 28% of the initial americium atoms were fissioned. The irradiation performance of the target was not optimal, however, as significant swelling (up to 18% in volume) was observed (Konings *et al*., 2000; Wiss *et al*., 2003). The cause of this swelling was revealed by the ceramographic analysis, which indicated a substantial porosity increase in the irradiated pellet (compared to 3% in the unirradiated fresh pellets). This could be attributed to the accumulation of helium produced by alpha decay of ^{242}Cm (a product in the transmutation chain of ^{241}Am) in gas bubbles. The $MgAl_2O_4$ matrix of the irradiated target was found to be amorphous in transmission electron microscopic studies (Wiss *et al*., 2003), which

could pose an additional contribution to the swelling. Similar experiments with microdispersed UO_2 instead of AmO_2 indicated that swelling occurred in these cases also at low operating temperature (Georgenthum *et al.*, 2001) but not at higher operating temperature (Neeft *et al.*, 2003). These results showed that the $MgAl_2O_4$ matrix has limited stability towards the impact of fission products of fission energy, and can thus only be used if the operating temperature is above the amorphous-crystal transition temperature.

34.9 CONCLUSIONS

The current knowledge of the properties and behavior of nuclear fuel is based on about six decades of extensive research. As a result, the behavior and operation limits of light-water reactor fuel are nowadays well understood. The vast amount of data from in-pile and out-of-pile experiments have been included in mechanistic fuel performance codes that can simulate and predict the fuel behavior for the current operation domain with high reliability. This does not mean that all underlying physical processes are completely understood yet. For example, the mechanism for the formation of the high burnup structure, an extreme consequence of radiation exposure, is still a matter of debate. Improved and sophisticated analytical techniques will continue to provide more detailed information but in parallel further understanding must result from modeling of the process mechanisms taking place at various scales of length and time.

The requirements for the fuels for the next-generation reactors are defined within the context of sustainability, competitiveness, safety and proliferation resistance. This means that breeding and recycling are key issues, as is transmutation to reduce the lifetime and toxicity of the fuel cycle waste. As a result, next generation reactor fuel will be chemically more complex and exposed to more extreme conditions. There is a promising knowledge base for uranium–plutonium fast reactor fuels from the past, but the requirement to recycle/transmute the minor actinides (Np, Am and eventually Cm) is a major challenge. This will require extensive research into the properties and behavior, fabrication technology and irradiation behavior of MA-bearing fuels and targets. In view of these challenges it is important that the experimental studies for next-generation reactor fuels are accompanied by extensive modeling, making use of the advantages of modern high performance computing tools, to make the transition from a predominantly empirical approach to fuel development to a more science-based approach.

LIST OF ABBREVIATIONS

An	generic for actinide
ADU	ammonium diuranate
AGR	advanced gas-cooled reactor

AUC	ammonium uranyl carbonate
bcc	body-centered cubic
BWR	boiling water reactor
COCA	Cobroyage Cadarache
EPMA	electron probe micro-analysis
FBR	fast breeder reactor
FIMA	fission of initial metal atoms
FR	fast reactor
fcc	face-centered cubic
GFR	gas-cooled fast reactor
HBS	high burn-up structure
HTR	high temperature reactor
IAEA	International Atomic Energy Agency
IDR	integrated dry route
IMF	inert matrix fuel
kgHM	kilogram Heavy Metal
Ln	generic for lanthanide
LWR	light water reactor
MA	minor actinides
MIMAS	micronized master blend
MOX	mixed oxide
MSR	molten salt reactor
MSBR	molten salt breeder reactor
OCOM	optimized comilling
O/M	oxygen over metal ratio
PCI	pellet-cladding interaction
PWR	pressurized water reactor
PyC	pyrolytic carbon
SBR	short binderless route
SEM	scanning electron microscopy
SFR	sodium-cooled fast reactor
TD	theoretical density
TEM	transmission electron microscopy
TRISO	tristructural siotropic

ACKNOWLEDGEMENTS

The authors wish to thank P. van Uffelen (JRC-ITU) and D. Staicu (JRC-ITU) for fruitful discussions, Y. Guerin (CEA), L. Morss (US-DOE), J. Somers (JRC-ITU) and C. Walker (JRC-ITU) for the critical review of the manuscript, J.P. Hiernaut (JRC-ITU), D. Freiss (JRC-ITU) and W. Goll (Areva) for providing some of the figures.

REFERENCES

Adamson, M. G., Aitken, E. A., and Caputi, R. W. (1985) *J. Nucl. Mater.*, **130**, 245–265.

Ades, M. J. and Peddicord, K. L. (1982) *Nucl. Sci. Eng*. **81**, 540–550.

Agarwal, R., Sen, B. K., and Venugopal, V. (2009) *J. Nucl. Mater.*, **385**, 112–116.

Ainscough, J. B., Oldfield, B. W., and Ware, J. O. (1973/1974) *J. Nucl. Mater.*, **47**, 117–128.

Aitken, E. A. and Evans, S. K. (1968) Tech. Rep. USAEC GEAP-5672, General Electric.

Amaya, M., Kubo, T., and Korei, Y. (1996) *J. Nucl. Sci. Technol.*, **33**, 636–640.

Antill, J. E., Peakall, K. A., and Smart, E. F. (1975) *J. Nucl. Mater.*, **56**, 47–60.

Arai, Y. and Minato, K. (2004) *J. Nucl. Mater.*, **344**, 180–185.

Arai, Y., Suzuki, Y., Iwai, T., and Ohmichi, T. (1992) *J. Nucl. Mater.*, **195**, 37–43.

Arai, Y., Okamoto, Y., and Suzuki, Y. (1994) *J. Nucl. Mater.*, **211**, 248–250.

Assmann, H. (1982) *J. Nucl. Mater.*, **106**, 15–34.

Assmann, H. and Stehle, H. (1979) *J. Nucl. Mater.*, **81**, 19–30.

Assmann, H., Peehs, M., and Roepenack, H. (1988) *J. Nucl. Mater.*, **153**, 115–126.

Ayer, J. E. and Soppet, F. E. (1965) *J. Am. Ceram. Soc.*, **48**, 180–183.

Bailly, H., Ménessier, D., and Prunier, C. (1999) *The Nuclear Fuel of Pressurized Water Reactors and Fast Neutron Reactors*, Lavoisier Publishing, Paris.

Bakker, K. and Konings, R. J. M. (1996) *Nucl. Technol.*, **115**, 91–99.

Bakker, K. and Konings, R. J. M. (1998) *J. Nucl. Mater.*, **254**, 129–134.

Bakker, K., Kwast, H., and Cordfunke, E. (1995) *J. Nucl. Mater.*, **226**, 128–143.

Bakker, K., Cordfunke, E. H. P., Konings, R. J. M., and Schram, R. P. C. (1997) *J. Nucl. Mater.*, **250**, 1–12.

Baron, D. (1998) *Proceedings of the Seminar Thermal Performance of High Burn-Up LWR Fuel*, Cadarache, France, March 3–6, 1998. OECD/NEA, p. 131.

Barth, G., Bakker, K., Hellwig, C., Kihara, Y., Ozawa, T., Wallin, H., and Shigetome, Y. (2007) *J. Nucl. Sci. Technol.*, **44**, 329–336.

Barton, C. J. (1959) *J. Phys. Chem.*, **64**, 306–307.

Bartscher, W. and Sari, C. (1983) *J. Nucl. Mater.*, **118**, 220–226.

Bartscher, W. and Sari, C. (1984) Commission of the European Communities, Joint Research Centre, European Institute for Treansuranium Elements, Programme Progress Report TSUR 38, p. 48.

Bartscher, W. and Sari, C. (1985) Commission of the European Communities, Joint Research Centre, European Institute for Treansuranium Elements, Programme Progress Report TSUR 39, pp. 54–55.

Beals, R. J., Handwerk, J. H., and Wrona, B. J. (1969) *J. Am. Ceram. Soc.*, **52**, 578–581.

Beauvy, M. (1992) *J. Nucl. Mater.*, **188**, 232–238.

Beneš, O. and Konings, R. J. M. (2008) *J. Fluorine Chem.*, **130**, 22–29.

Beneš, O. and Konings, R. J. M. (2009) *J. Chem. Thermodyn.*, **41**, 1086–1095.

Besmann, T. M. and Lindemer, T. B. (1978) *Nucl. Technol.*, **40**, 297–306.

Besmann, T. M. and Lindemer, T. B. (1985) *J. Nucl. Mater.*, **130**, 489–504.

Besmann, T. M. and Lindemer, T. B. (1986) *J. Nucl. Mater.*, **137**, 292–293.

Billaux, M. (2005) *The 2005 Frédéric Joliot and Otto Hahn Summerschool*, Karlsruhe, Germany.

Blank, H. (1972) *Phys. Stat. Sol. (a)*, **10**, 465–478.

Blank, H. (1988) *J. Nucl. Mater.*, **153**, 171–177.

Blank, H. (1994) *Materials Science and Technology*, VCH Verlagsgesellschaft mbH, Chapter 4, pp. 194–363.
Blank, H. and Matzke, H. (1973) *Radiat. Eff.*, **17**, 57–64.
Bober, M. and Schumacher, G. (1973) *Advances in Nuclear Science and Technology*. Vol. 7, Academic, New York, pp. 495–564.
Bowsher, B. R. (1987) *Progr. Nucl. Energy*, **20**, 199–233.
Bramman, J. I., Sharpe, R. M., and Dixon, R. (1971) *J. Nucl. Mater.*, **38**, 236–239.
Brucklacher, D. and Dienst, W. (1972) *J. Nucl. Mater.*, **42**, 285–296.
Burkes, D. E., Fielding, R. S., Porter, D. L., Crawford, D. C., and Meyer, M. K. (2009) *J. Nucl. Mater.*, **389**, 458–469.
Bychkov, A. V., Skiba, O. V., Mayorshin, A. A., Kormilitsyn, M. V., Shishalov, O. V., Zhemkov, I., Kisly, V., and Babikov, L. G. (June 2002) in *Actinide and Fission Product Partitioning and Transmutation. Seventh Information Exchange Meeting*, Jeju, Republic of Korea, October 2002, pp. cd–rom.
Carbajo, J. J., Yoder, G. L., Popov, S. G., and Ivanov, V. K. (2001) *J. Nucl. Mater.*, **299**, 181–198.
Chauvin, N., Konings, R. J. M., and Matzke, H. (1999) *J. Nucl. Mater.*, **274**, 105–111.
Chauvin, N., Malo, J. Y., Garnier, J. C., Bertrand, F., Bosq, J. C., Ravenet, A., Lorenzo, D., Pelletier, M., Escleine, J. M., Munoz, I., and Bonnerot, J. M. (2007) in *Proceedings GLOBAL 2007: Advanced Nuclear Fuel Cycles and Systems*, Boise ID, September 2007. p. cd rom.
Chevalier, P. Y. and Fischer, E. (2001) *J. Nucl. Mater.*, **288**, 100–129.
Chevalier, P. Y., Fischer, E., and Cheynet, B. (2000) *J. Nucl. Mater.*, **280**, 136–150.
Chevalier, P. Y., Fischer, E., and Cheynet, B. (2004) *Calphad*, **28**, 15–40.
Chikalla, T. D. and Eyring, L. (1968) *J. Inorg. Nucl. Chem.*, **30**, 133–145.
Cordfunke, E. H. P. and Konings, R. J. M. (1988) *J. Nucl. Mater.*, **152**, 301–309.
Cozzo, C., Staicu, D., Pagliosa, G., Papaioannou, D., Rondinella, V., Konings, R.J.M., Walker, C., Barker, M., Herve, P. J. (2009) *J. Nucl. Mater.*, in press.
Croixmarie, Y., Abonneau, E., Fernández, A., Konings, R. J. M., Desmoulière, F., and Donnet, L. (2003) *J. Nucl. Mater.*, **320**, 11–17.
Cronenberg, A. W. and Osetek, D. J. (1987) *J. Nucl. Mater.*, **149**, 252–260.
Dayton, R. W. (1960) *Reactor Handbook. Second Edition. Volume I. Materials*, Inter-Science Publishers, New York, pp. 87–89.
de Halas, D. R. and Horn, G. R. (1963) *J. Nucl. Mater.*, **2**, 207–220.
Desgranges, L., Pasquet, B., Valot, C., and Roure, I. (2009) *J. Nucl. Mater.*, **385**, 99–102.
Dumas, J. C., Martial, C., Sundman, B., Dupin, N., Guéneau, C. (2009) *F-BRIDGE Plenary Meeting*, 1–2 April 2009, PSI, Switzerland.
Dupin, N., Guneau, C., and Konings, R. J. M. (2009) *F-BRIDGE Plenary Meeting*, 1–2 April 2009, PSI, Switzerland.
Duriez, C., Alessandri, J. P., Gervais, T., and Philipponneau, Y. (2000) *J. Nucl. Mater.*, **277**, 143–158.
Fahey, J. A., Turcotte, R. P., and Chikalla, T. D. (1974) *Inorg. Nucl. Chem. Lett.*, **10**, 459–465.
Fernández, A., Haas, D., Konings, R. J. M., and Somers, J. (2002) *J. Am. Ceram. Soc.*, **85**, 694–696.
Fink, J. K. (2000) *J. Nucl. Mater.*, **279**, 1–18.
Fischer, E. (2008) *CALPHAD*, **32**, 371–377.

Fischer, E. (2009) CALPHAD, doi:10.1016/j.calphad.2009.01.004.
Fisher, S. B., White, R. J., Cook, P. M. A., Bremier, S., Corcoran, R. C., Stratton, R., Walker, C. T., Ivison, P. K., and Palmer, I. D. (2002) *J. Nucl. Mater*., **306**, 153–172.
Freis, D., Bottomley, D., Ejton, J., de Weerd, W., Kostecka, H., and Toscano, E. H. (2008) in *Proceedings HTR2008: 4th International Topical Meeting on High Temperature Reactor Technology*, October 1–4, 2008, Washington, USA, pp. Article number: HTR2008–58203.
Freshley, M. D. (1972) *Nucl. Eng. Des*., **21**, 264–278.
Freshley, M. D. and Mattys, H. M. (1962) Tech. Rep. HW-76559, General Electric.
Georgenthum, V., Brillaud, J., Chauvin, N., Pelletier, M., and Planck, D. (2001) *Progr. Nucl. Energy*, **38**, 317–320.
Gibby, R. L. (1971) *J. Nucl. Mater*., **38**, 163–177.
Gorlé, F., Coheur, L., and Timmermans, W. (1974) *J. Nucl. Mater*., **51**, 343–353.
Grandjean, S., Arab-Chapelet, B., Robisson, A. C., Picart, S., Dancausse, J. P., Baron, P., Brossard, P., and Warin, D. (2007) in *Proceedings GLOBAL 2007: Advanced Nuclear Fuel Cycles and Systems*, Boise, ID, September 2007. pp. 98–105.
Gratchyov, A. F., Skiba, O. V., Tsykanov, V. A., Ivanov, V. B., Mayorshin, A. A., Bychkov, A. V., Kisly, V. A., Shishalov, O. V., Ossipenk, A. G., Krukov, F. N., Novosyolov, A. E., Smirnov, V. P., Dvoretsky, V. G., Oshkanov, N. N., Maltsev, V. V., Vaslilyev, B. A., Asaga, T., Ishii, T., and Maeda, K. (2007) *J. Nucl. Sci. Technol*., **44**, 504–510.
Grimes, W. R. (1970) *Nucl. Appl. Technol*., **8**, 137–149.
Grimes, R. W. and Catlow, C. R. A. (1991) *Phil. Trans. R. Soc. London A*, **335**, 609–634.
Grimes, W. R. and Cuneo, D. R. (1960) *Reactor Handbook*, *2nd Edition*, Interscience Publishers, New York, Chapter 17.
Guéneau, C., Baichi, M., Labroche, D., Chatillon, C., and Sundman, B. (2002) *J. Nucl. Mater*., **304**, 161–175.
Guéneau, C., Chantain, S., Dumas, J. C., Lechelle, J., Rado, C., Defoort, F., Dupin, N., Sundman, B., Noël, H. and Konings, R. (2006) in *Proceedings HTR2006: 3rd International Topical Meeting on High Temperature Reactor Technology*, Johannesburg, October 1–4, 2006, pp. 225–232.
Guéneau, C., Dupin, N., Sundman, B., Rado, C., and Konings, R. (2007) A progress report on the development of FUELBASE, a thermodynamic database for the description of multicomponent systems for nuclear fuel applications part 1. Binary systems. Tech. Rep. CEA Report, RT DPC/SCP 07-224 indice A, CEA/DEN/DANS/DPC/SCP/07-DO-31.
Guéneau, C., Chatillon, C., and Sundman, B. (2008) *J. Nucl. Mater*., **378**, 257–272.
Haas, D., Bottomley, P. D. W., Cojazzi, G. G. M., Glatz, J. P., Hähner, P., Hurst, R., Konings, R. J. M., Rondinella, V. V., and Somers, J. (2009) in *GLOBAL 2009. The Nuclear Fuel Cycle: Sustainable Options & Industrial Perspectives*, September 6–11, 2009, pp. on cd–rom.
Hagrman, D. L. and Reymann, G. A. (1979) *MATPRO Version 11-A*, *Handbook of Materials Properties for Use in the Analysis of Light Water Reactor Fuel Rod Behavior*, *TREENUREC-1280 Advanced Inorganic Chemistry*, Revision 3.
Haubenreich, P. N. and Engel, J. R. (1970) *Nucl. Appl. Technol*., **8**, 118–133.
Hayes, S. L., Thomas, J. K., and Peddicord, K. L. (1990a) *J. Nucl. Mater*., **171**, 262–270.
Hayes, S. L., Thomas, J. K., and Peddicord, K. L. (1990b) *J. Nucl. Mater*., **171**, 271–288.

Hayes, S. L., Thomas, J. K., and Peddicord, K. L. (1990c) *J. Nucl. Mater.*, **171**, 300–318.
Hayes, S. L., Thomas, J. K., and Peddicord, K. L. (1990d) *J. Nucl. Mater.*, **171**, 289–299.
Hellwig, C. and Kasemeyer, U. (2003) *J. Nucl. Mater.*, **319**, 87–94.
Hellwig, C., Pouchon, M., Restani, R., Ingold, F., and Bart, G. (2005) *J. Nucl. Mater.*, **340**, 163–170.
Hellwig, C., Streit, M., Blair, P., Tverberg, T., Klaassen, F. C., Schram, R. P. C., Vettraino, F., and Yamashita, T. (2006) *J. Nucl. Mater.*, **352**, 291–299.
Hiernaut, J. P. and Ronchi, C. (2001) *J. Nucl. Mater.*, **294**, 39–44.
Hiernaut, J. P., Wiss, T., Colle, J. Y., Thiele, H., Walker, C. T., Goll, W., and Konings, R. J. M. (2008a) *J. Nucl. Mater.*, **377**, 313–324.
Hiernaut, J. P., Wiss, T., Papaioannou, D., Konings, R. J. M., and Rondinella, V. V. (2008b) *J. Nucl. Mater.*, **372**, 215–225.
Higgs, J. D., Lewis, B. J., Thompson, W. T., and He, Z. (2007) *J. Nucl. Mater.*, **366**, 99–128.
Hofman, G. L. and Walters, L. C. (1994) *Materials Science and Technology*, VCH Verlagsgesellschaft mbH, pp. 1–42, Chapter 4.
Hofman, G. L., Hayes, S., and Petri, M. C. (1996) *J. Nucl. Mater.*, **227**, 277–286.
Hofmann, G. L., Walters, L., and Bauer, T. H. (1997) *Prog. Nucl. Energy*, **31**, 83–110.
IAEA (2006) Thermophysical properties database of materials for light water reactors and heavy water reactors. Tech. Rep. IAEA-TECDOC-1496.
Ignatiev, V., Merzlyakov, A., Afonichkin, V., Khokhlov, V., Salyulev, A., Golovatov, Y., Grebenkine, K., and Subbotin, V. (June 2002) in *Actinide and Fission Product Partitioning and Transmutation. Seventh Information Exchange Meeting*, Jeju, Republic of Korea, October 2002, pp. cd–rom.
Inoue, M., Maeda, K., Katsuyama, K., Tanaka, K., Mondo, K., and Hisada, M. (2004) *J. Nucl. Mater.*, **326**, 59–73.
Ishimoto, S., Hirai, M., Ito, K., and Korei, Y. (1994) *J. Nucl. Sci. Technol.*, **31**, 796–802.
Johnson, I. and Johnson, C. E. (1988) *J. Nucl. Mater.*, **154**, 67–73.
Jolkonnen, M., Streit, M., and Wallenius, J. (2004) *J. Nucl. Sci. Technol.*, **41**, 457–465.
Kang, K. W., Yang, J. H., Kim, J. H., Rhee, Y. W., Kim, D. J., Kim, K. S., and Song, K. W. (2007) *Thermochim. Acta* **455**, 134–137.
Kasiviswanathan, K., Venkiteswaran, C., Karthik, V., Venugopal, V., Muralidharan, N. G., and Joseph, J. (2007) *J. Nucl. Mater.*, doi:10.1016/j.jnucmat.2007.09.044.
Kato, M., Uno, H., Tamura, T., Morimoto, K., Konashi, K., and Kihara, Y. (2006) *Recent Advances in Actinide Science*, Royal Society of Chemistry, Cambridge, pp. 367–372.
Kato, M., Morimoto, K., Sugata, H., Konashi, K., Kashimura, M., and Abe, T. (2008a) *J. Alloys Comp.*, **452**, 48–53.
Kato, M., Morimoto, K., Sugata, H., Konashi, K., Kashimura, M., and Abe, T. (2008b) *J. Nucl. Mater.*, **373**, 237–245.
Kato, M., Konashi, K., and Nakae, N. (2009a) *J. Nucl. Mater.*, **389**, 164–169.
Kato, M., Tamura, T., and Konashi, K. (2009b) *J. Nucl. Mater.*, **385**, 419–423.
Keiser, D. D. Jr., Kennedy, J. R., Hilton, B. A., and Hayes, S. L. (2008) *JOM* January, 29–32.
Killeen, J. C. (1980) *J. Nucl. Mater.*, **88**, 177–184.
Kim, Y. S., Hofman, G. L., Hayes, S. L., and Sohn, Y. H. (2004) *J. Nucl. Mater.*, **327**, 27–36.

Kim, Y. S., Hayes, S. L., Hofman, G. L., and Yacout, A. M. (2006) *J. Nucl. Mater.*, **359**, 17–28.
Kinchin, G. H. and Pease, R. S. (1955) *Rep. Progr. Phys.*, 18, 1–51.
Kinoshita, M., Sonoda, T., Kitajima, S., Sasahara, A., Kameyama, T., Matsumura, T., Kolstad, E., Rondinella, V. V., Ronchi, C., Hiernaut, J. P., Wiss, T., Kinnart, F., Ejton, J., Papaioannou, D., and Matzke, H. (2004) in *Proceedings of the 2004 International Meeting on LWR Fuel Performance*, Orlando, FL, pp. 207–213.
Kittel, J. H., Frost, B. R. T., Mustelier, J. P., Bagley, K. Q., Crittenden, G., and van Dievoet, J. (1993) *J. Nucl. Mater.*, **204**, 1–13.
Klein, D., Baer, W., and Smith, G. G. (1958) *Nucl. Sci. Eng.*, **3**, 698–.
Kleykamp, H. (1973) *J. Nucl. Mater.*, **47**, 271–277.
Kleykamp, H. (1979) *J. Nucl. Mater.*, **84**, 109–117.
Kleykamp, H. (1985) *J. Nucl. Mater.*, **131**, 221–246.
Kleykamp, H. (1990) Tech. Rep. KfK 4701.
Kleykamp, H. (1997) *J. Nucl. Mater.*, **209**–213, 1–7.
Kleykamp, H., Paschoal, J. O., Pejsa, R., and Thümmler, F. (1985) *J. Nucl. Mater.*, **130**, 426–433.
Konings, R. J. M. (2001) *J. Nucl. Mater.*, **295**, 57–63.
Konings, R. J. M. and Haas, D. (2002) *C R Phys.*, **3**, 1013–1022.
Konings, R. J. M., Conrad, R., Dassel, G., Pijlgroms, B., Somers, J., and Toscano, A. (2000) *J. Nucl. Mater.*, **282**, 159–170.
Kurata, M. (1999) *CALPHAD*, 23, 305–337.
Kurata, M., Sasahara, A., Inoue, T., Betti, M., Babelot, J. F., Spirlet, J. C., and Koch, L. (1997) in *Proceeding GLOBAL'97*, Yokohama, Japan, pp. 1384–1389.
Lackley, W. J., Homan, F. J., and Olsen, A. R. (1972) *Nucl. Technol.*, **16**, 120142.
Lambertson, W. A., Mueller, M. H., and Gunzel, F. H. (1953) *J. Am. Ceram. Soc.*, **36**, 397–399.
Ledergerber, G., Degueldre, C., Heimgartner, P., Pouchon, M. A., and Kasemeyer, U. (2001) *Prog. Nucl. Energy*, **38**, 301–308.
Lemehov, S. E., Sobolev, V., and van Uffelen, P. (2005) *J. Nucl. Mater.*, **320**, 66–76.
Lewis, H. D. and Kerrisk, J. F. (1976) Tech. Rep. LA-6096.
Lorenzelli, N. and Marcon, J. P. (1972) *J. Nucl. Mater.*, **44**, 57–63.
Lozano, N., Desgranges, L., Aymes, D., and Niepce, J. C. (1998) *J. Nucl. Mater.*, **257**, 78–87.
Lutique, S., Staicu, D., Konings, R. J. M., Rondinella, V. V., Somers, J., and Wiss, T. (2003) *J. Nucl. Mater.*, **319**, 59–64.
Lyon, W. L. and Bailey, W. E. (1967) *J. Nucl. Mater.*, **22**, 332–339.
MacPherson, H. G. (1985) *Nucl. Sci. Eng.*, **90**, 374–379.
Maeda, K., Katsuyama, K., and Asaga, T. (2005) *J. Nucl. Mater.*, **346**, 244–252.
Maeda, K., Sasaki, S., Kato, M., and Kihara, Y. (2009) *J. Nucl. Mater.*, **389**, 78–84.
Majumdar, S., Sengupta, A. K., and Kamath, H. S. (2006) *J. Nucl. Mater.*, **352**, 165–173.
Manara, D., Ronchi, C., Sheindlin, M., Lewis, M., and Brykin, M. (2005) *J. Nucl. Mater.*, **342**, 148–163.
Manzel, R. and Walker, C. T. (2002) *J. Nucl. Mater.*, **301**, 170–182.
Markin, T. L. and Rand, M. H. (1966) *Thermodynamics*, vol. 1, IAEA, Vienna, pp. 145–156.
Markin, T. L. and Street, R. S. (1967) *J. Inorg. Nucl. Chem.*, **29**, 2265–2280.

Mason, R. E., Hoth, C. W., Stratton, R. W., and Botta, F. B. (1992) *Trans. Am. Nucl. Soc*., **6**, 215–218.
Mathieu, L., Heuer, D., Brissot, R., Garzenne, C., Le Brun, C., Lecarpentier, D., Liatard, E., Loiseaux, J. M., Méplan, O., Merle-Lucotte, E., Nuttin, A., Walle, E., and Wilson, J. (2006) *Progr. Nucl. Energy*, **48**, 664–679.
Matsui, H., Horiki, M., and Kirihara, T. (1981) *J. Nucl. Sci. Technol*., **18**, 171–.
Mattys, H. M. (1968) *Actinides Rev*., **1**, 165–182.
Matzke, H. (1980) *Radiat. Eff*., **53**, 219–242.
Matzke, H. (1982) *Radiat. Eff*., **64**, 3–33.
Matzke, H. (1983) *Radiat. Eff*., **75**, 317–325.
Matzke, H. (1985) *J. Nucl. Mater*., **223**, 1–5.
Matzke, H. (1986) *Science of Advanced LMFBR Fuels*, North Holland, Amsterdam.
Matzke, H. (1987) *J. Chem. Soc. Faraday Trans*., **83**, 1121–1142.
Matzke, H. (1990) *J. Chem. Soc. Faraday Trans*., **86**, 1243–1256.
Matzke, H. (1994) *J. Nucl. Mater*., **208**, 18–26.
Matzke, H. (1995) *J. Nucl. Mater*., **208**, 1–5.
Matzke, H. (1999) in *Technical Committee Meeting on Technical and Economic Limits to Fuel Burnup Extension*, IAEA, San Carlos de Bariloche, Argentina, November 15–19, pp. 207–213.
Matzke, H., Blank, H., Coquerelle, M., Lassmann, K., Ray, I. L. F., Ronchi, C., and Walker, C. T. (1989) *J. Nucl. Mater*., **166**, 165–178.
Mayorshin, A. A., Skiba, O. V., Tsykanov, V. A., and Kisly, V. A. (2000) in *Proceedings 8th International Conference on Nuclear Engineering (ICONE 8*), Baltimore, MD, April 26, 2000.
Medvedev, P., Frank, S. M., O'Holleran, T. P., and Meyer, M. K. (2005) *J. Nucl. Mater*., **342**, 48–62.
Merle-Lucotte, E., Heuer, D., Allibert, M., Doligeza, X., Ghetta, V., and Le Brun, C. (2008) in *PHYSOR: International Conference on the Physics of Reactors Nuclear Power: A Sustainable Resource*, Switzerland, p. Paper log355.
Meyer, M. K., Hayes, S. L., Carmack, W. J., and Tsai, H. (2009) *J. Nucl. Mater*., **392**, 176–183.
Mignanelli, M. A. and Potter, P. E. (1984) *J. Nucl. Mater*., **125**, 182–201.
Millet, C. and Piconi, C. (1983) *J. Nucl. Mater*., **116**, 195–202.
Minato, K., Ogawa, T., Kashimura, S., Fukuda, K., Shimizu, M., Tayama, Y., and Takahashi, I. (1990) *J. Nucl. Mater*., **172**, 184–196.
Minato, K., Ogawa, T., Fukuda, K., Shimizu, M., Tayama, Y., and Takahashi, I. (1994) *J. Nucl. Mater*., **208**, 266–281.
Minato, K., Ogawa, T., and Fukuda, K. (1997) *J. Nucl. Mater*., **249**, 142–149.
Minato, K., Takano, M., Otobe, H., Nishi, T., Akabori, M., and Arai, Y. (2009) *J. Nucl. Mater*., **389**, 23–28.
Mogensen, M., Pearce, J., and Walker, C. (1999) *J. Nucl. Mater*., **264**, 99–112.
Morimoto, K., Kato, M., Osagawara, M., and Kashimura, M. (2008) *J. Nucl. Mater*., **374**, 378–385.
Mosley, W. C. (1972) *J. Inorg. Nucl. Chem*., **34**, 539–555.
Mouchnino, M. (1969) Tech. Rep. CEA-3353, Commisariat à l'Energie Atmomique.
Nabielek, H., Schenk, W., Heit, W., Mehner, A. W., and Goodin, D. (1989) *Nucl. Technol*., **84**, 62–75.

Nakajima, K., Arai, Y., and Suzuki, Y. (1997) *J. Nucl. Mater.*, **247**, 33–37.
Neeft, E. A. C., Bakker, K., Schram, R. P. C., Conrad, R., and Konings, R. J. M. (2003) *J. Nucl. Mater.*, **320**, 106–116.
Neimark, L. A., Lambert, J. D., Murphy, W. F., and Renfro, C. W. (1972) *Nucl. Technol.*, **16**, 75–82.
Nishi, T., Takano, M., Itoh, A., Akabori, M., Minato, K., and Kizaki, M. (2006) *J. Nucl. Mater.*, **355**, 114–118.
Nishi, T., Itoh, A., Takano, M., Numata, M., Akabori, M., Arai, Y., and Minato, K. (2008a) *J. Nucl. Mater.*, **376**, 78–82.
Nishi, T., Takano, M., Itoh, A., Akabori, M., Arai, Y., Minato, K., and Numata, M. (2008b) *J. Nucl. Mater.*, **377**, 295–298.
Noden, J. D. (1973) *J. Br. Nucl. Energy Soc.*, **12**, 329–333.
Nogita, K. and Une, K. (1994) *Nucl. Instr. Meth. Phys. Res. B*, **91**, 301–306.
Nogita, K. and Une, K. (1995) *J. Nucl. Mater.*, **226**, 302–310.
Noirot, J., Desgranges, L., and Lamontagne, J. (2008) *J. Nucl. Mater.*, **372**, 318–339.
Nutt, A. W. and Tokar, M. (1972) Tech. Rep. LA-4945, Los Alamos National Laboratory.
O'Boyle, D. R., Brown, F. L., and Sanecki, J. E. (1969) *J. Nucl. Mater.*, **29**, 27–42.
Ogata, T. (2002) *J. Nucl. Sci. Technol. Suppl.*, **3**, 675–681.
Ogawa, T. (1995) *J. Alloys Comp.*, **194**, 1–7.
Ogawa, T., Ohmichi, T., Maeda, A., Arai, Y., and Suzuki, Y. (1995) *J. Alloys Comp.*, **224**, 55–59.
Ohta, H., Yokoo, T., Ogata, T., Inoue, T., Ougier, M., Glatz, J. P., Fontaine, B., and Breton, L. (2009) *Nucl. Technol.*, **165**, 96–110.
Olander, D. (1976) Fundamental aspects of nuclear reactor fuel elements. Tech. Rep. TID-26711- P1, Technical Information Center, Office of Public Affairs Energy Research and Development Administration (1976)
Olson, W. M. and Mulford, R. N. R. (1964) *J. Phys. Chem.*, **68**, 1048–1051.
Oudinet, G., Munoz-Viallard, I., Aufore, L., Gotta, M. J., Becker, J. M., Chiarelli, G., and Castelli, R. (2008) *J. Nucl. Mater.*, **375**, 86–94.
Paquette, J., Torgerson, D. F., Wren, J. C., and Wren, D. J. (1985) *J. Nucl. Mater.*, **130**, 129–138.
Pelletier, M. (2008) *Les Combustibles Nucléaires*, Commissariat à l'énergy atomique, Editions Le Moniteur, Paris, pp. 91–93.
Petti, D. A., Buongiorno, J., Maki, J. T., Hobbins, R. R., and Miller, G. (2003) *Nucl. Eng. Des.*, **222**, 281–297.
Picard, E., Noirot, J., Moss, R. L., Plitz, H., Richter, K., and Rouault, J. (2000) *Nucl. Technol.*, **129**, 1–12.
Predel, B. (1998) *Phase Equilibria, Crystallographic and Thermodynamic Data of Binary Alloys*, Vol. 5-I, Springer, Berlin, Germany.
Prunier, C., Boussard, F., Koch, L., and Coquerelle, M. (1997) *Nucl. Technol.*, **119**, 141–148.
Rand, M. and Markin, T. R. (1968) *Thermodynamics of Nuclear Materials*, IAEA, Vienna. p. 637.
Ray, I. L. F. and Blank, H. (1984) *J. Nucl. Mater.*, **124**, 159–174.
Ray, I. L. F. and Matzke, H. (1991) *Fundamental Aspects of Inert Gases in Solids*, Plenum Press, New York, pp. 457–467

Ray, I. L. F., Matzke, H., Thiele, H., and Kinoshita, M. (1997) *J. Nucl. Mater.*, **245**, 115–123.
Reynolds, G. H., Janvier, J. C., Kaae, J. L., and Morlevat, J. P. (1976) *J. Nucl. Mater.*, **62**, 9–16.
Richter, K., Kramer, G., and Gueugnon, J. F. (1979) *Trans Am. Nucl. Soc.*, **31**, 213–216.
Richter, K., Benedict, U., Gueugnon, J. F., Kutter, H., Sari, C., and Mühling, G. (1988) *J. Nucl. Mater.*, **153**, 205–210.
Richter, K., Fernández, A., and Somers, J. (1997) *J. Nucl. Mater.*, **249**, 121–127.
Ronchi, C. (1973) *J. Appl. Phys.*, **44**, 3575–.
Ronchi, C. and Wiss, T. (2002) *J. Appl. Phys.*, **10**, 5837–5848.
Ronchi, C., Shiendlin, M., Musella, M., and Hyland, G. J. (1999) *J. Appl. Phys.*, **85**, 776–789.
Ronchi, C., Iosilevski, I. L., and Yakub, E. (2004a) *Equation of State of Uranium Dioxide*, Springer, New York.
Ronchi, C., Sheindlin, M., Staicu, D., and Kinoshita, M. (2004b) *J. Nucl. Mater.*, **327**, 58–76.
Sabau, A. S. and Ohriner, E. K. (2008) *J. Nucl. Mater.*, **376**, 251–253.
Sari, C. and Schumacher, G. (1976) *Nucl. Technol.*, **28**, 256–260.
Sari, C. and Zamorani, E. (1970) *J. Nucl. Mater.*, **37**, 324–330.
Schenk, W., Pott, G., and Nabielek, H. (1990) *J. Nucl. Mater.*, **171**, 19–30.
Schmidt, H. E. (1970) Tech. Rep. Progress Report No. 9 July–December 1969, No. 2576.
Schmidt, H. E. (1971) *High Temp.-High Press.*, **3**, 345–353.
Schmidt, H. E. (1975) Proc. 4th Journées d' Actinides, Harwell, UK (June 26, 1974), Atomic Energy Research Establishment Report AERE-R-7961.
Schmidt, H. E., Sari, C., Richter, K., and Gerontopoulos, P. (1986) *J. Less-Common Met.*, **121**, 621–630.
Schulz, B. (1981) *High Temp. High Press.*, **13**, 649–657.
Serizawa, H., Arai, Y., and Nakajima, K. (2001) *J. Chem. Thermodyn.*, **33**, 615–628.
Sidky, P. S. (1998) *J. Nucl. Mater.*, **256**, 1–17.
Smith, P. K. and Peterson, D. E. (1970) *J. Chem. Phys.*, **52**, 4963–4972.
Sonoda, T., Kinoshita, M., Ray, I. L. F., Wiss, T., Thiele, H., Pellottiero, D., Rondinella, V. V., and Matzke, H. (2002) *Nucl. Instr. Meth. Phys. Res. B*, **191**, 622–628.
Spear, K. E. and Leitnaker, J. M. (1968) Tech. Rep. ORNL-TM-2106, Oak Ridge National Laboratory.
Spino, J. and Papaioannou, D. (2008) *J. Nucl. Mater.*, **372**, 416–420.
Spino, J. and Peerani, P. (2008) *J. Nucl. Mater.*, **375**, 8–25.
Spino, J., Vennix, K., and Coquerelle, M. (1996) *J. Nucl. Mater.*, **231**, 179–190.
Spino, J., Cobos-Sabate, J., and Rousseau, F. (2003) *J. Nucl. Mater.*, **322**, 204–216.
Spino, J., Papaioannou, D., and Glatz, J. P. (2004) *J. Nucl. Mater.*, **328**, 67–70.
Spino, J., Rest, J., Goll, W., and Walker, C. T. (2005) *J. Nucl. Mater.*, **346**, 131–144.
Staicu, D. (2010) in *Comprehensive Nuclear Materials*, Elsevier, Oxford, Chapter 38.
Suzuki, Y., Maeda, A., Arai, Y., and Ohmichi, T. (1999) *J. Nucl. Mater.*, **188**, 239–243.
Takano, M., Akabori, M., Arai, Y., and Minato, K. (2008) *J. Nucl. Mater.*, **376**, 114–118.
Tanaka, K., Maeda, K., Katsuyama, K., Inoue, M., Iwai, T., and Arai, Y. (2004) *J. Nucl. Mater.*, **327**, 77–87.
Tanaka, K., Miwa, S., Sato, I., Hirosawa, T., Obayashi, H., S, K., Yoshimochi, H., and Tanaka, K. (2009) *J. Nucl. Mater.*, **385**, 407–412.

Thiriet, C. and Konings, R. J. M. (2003) *J. Nucl. Mater*., **320**, 292–298.
Tourasse, M., Boidron, M., and Pasquet, B. (1992) *J. Nucl. Mater*., **188**, 49–57.
Turnbull, J. A., Friskney, C., Findlay, J., Johnson, F., and Walter, A. J. (1982) *J. Nucl. Mater*., **107**, 168–184.
Uchida, T., Arima, T., Idemitsu, K., and Inagaki, Y. (2009) *Comput. Mater. Sci*., **45**, 229–234.
Ugajin, M. (1982) *J. Nucl. Mater*., **110**, 140–146.
Une, K. and Oguma, M. (1983) *J. Nucl. Mater*., **115**, 84–90.
Une, K., Nogita, K., Kashibe, S., and Imamura, M. (1992) *J. Nucl. Mater*., **188**, 65–72.
Une, K., Nogita, K., Shiratori, T., and Hayashi, K. (2001) *J. Nucl. Mater*., **288**, 20–28.
Utton, C. A., Bruycker, F. D., Boboridis, K., Jardin, R., Noël, H., Guéneau, C., and Manara, D. (2008) *J. Nucl. Mater*., **385**, 443–448.
Valin, S., Caillot, L., Dehaudt, P., Guerin, Y., Mocellin, A., Delafoy, C., and Chotard, A. (2003) in *Advanced Fuel Pellet Materials and Designs for Water Cooled Reactors. Proceedings of a Technical Committee Meeting*, Brussels, 20–24 October 2003, IAEA-TECDOC-1416, pp. 175–186.
Van Craeynest, J. C. and Weilbacher, J. C. (1968) *J. Nucl. Mater*., **26**, 132–136.
Van der Linde, A. (1991) Some fundamental aspects of the thermal conductivity of heterogeneously composed sphere-fac fuel. Tech. Rep. ECN-R–91-002.
Van der Linde, A. and Verheugen, J. H. N. (1982) *Nucl. Technol*., **59**, 70–77.
van der Meer, J. P. M. and Konings, R. J. M. (2006) *J. Nucl. Mater*., **360**, 16–24.
Vitanza, C., Kolstad, E., and Graziani, V. (1979) in *Proceedings of ANS Topical Meeting on LWR Fuel Performance*, Portland, OR, ANS, La Grange Park, IL, pp. 366–376.
Walker, C. T. (1978) *J. Nucl. Mater*., **74**, 358–362.
Walker, C. T. and Nicolaou, G. (1995) *J. Nucl. Mater*., **218**, 129–138.
Walker, C. T., Rondinella, V. V., Papaioannou, D., Van Winckel, S., Goll, W., and Manzel, R. (2005) *J. Nucl. Mater*., **345**, 192–205.
Walker, C. T., Staicu, D., Sheindlin, M., Papaioannou, D., Goll, W., and Sontheimer, F. (2006) *J. Nucl. Mater*., **97**, 137–203.
Wallenius, J. and Pillon, S. (2001) in *Proceedings of Nuclear Application in the New Millenium* (Ac-cApp/ADTTA'01), ANS, Reno, NV, pp. 5–9.
Was, G. S. and Allen, T. R. (2008) *NATO Science Series II. Mathematics, Physics and Chemistry, Vol. 235, Radiation Effects in Solids*, Springer, London, pp. 65–98.
Wiesenack, W. (1997) in *Proceedings of International Topical Meeting on Light Water Reactor Fuel Performance*, Portland, OR, March 2–6.
Willis, B. T. M. (1963) *Nature*, **197**, 755–756.
Willis, B. T. M. (1978) *Acta Cryst*., **A34**, 88–90.
Willis, B. T. M. (1987) *J. Chem. Soc. Faraday Trans*., **2**, 83.
Wiss, T., Matzke, H., Trautmann, C., Klaumünzer, S., and Toulemonde, M. (1997) *Nucl. Instr. Meth. Phys. Res. B*, **122**, 583–588.
Wiss, T., Konings, R. J. M., Walker, C. T., and Thiele, H. (2003) *J. Nucl. Mater*., **320**, 85–95.
Wriedt, H. A. (1989) *Bull. Alloys Phase Diagrams*, **10**, 593–602.
Yakub, E., Staicu, D., and Ronchi, C. (2009) *J. Nucl. Mater*., **389**, 119–126.
Yvon, P., Carré, F. (2009) *J. Nucl. Mater*. **385**, 217–222.
Ziegler, J. F., Biersack, J. P., and Littmark, U. (1985) *The Stopping and Range of Ions in Solids*, Pergamon, London.